INSTYTUT PROBLEMÓW JĄDROWYCH im. Andrzeja Sołtana
THE ANDRZEJ SOŁTAN INSTITUTE FOR NUCLEAR STUDIES

Julia Hoffman

Search for light neutral Higgs bosons in 2HDM model in e^+e^- collisions using DELPHI detector at LEP.

A dissertation submitted to
the A. Soltan's Institute for Nuclear Studies
in partial fulfillment of the requirements
for the degree of Doctor of Philosophy
in
The High Energy Division

Under supervision of
professor Ryszard Sosnowski

Warsaw 2003

Abstract

This thesis presents searches for neutral Higgs bosons produced at LEP in the Yukawa process $e^+e^- \to f_1\bar{f}_1 A/h \to f_1\bar{f}_1 f_2\bar{f}_2$, where $f_{1,2} = b, \tau$. The search has been performed within a Two Higgs Doublet Model (2HDM), for the mass range of 4 – 70 GeV/c^2, using data collected by the DELPHI detector at LEP for 1994 and 1995 years at about 91 GeV centre-of mass energy. Three different final states were considered: $\tau^+\tau^-\tau^+\tau^-$, $b\bar{b}\tau^+\tau^-$ and $b\bar{b}b\bar{b}$. The analysed data amounts to luminosity of $\sim$80 pb^{-1}. Results are presented in the form of mass-dependent upper bounds on coupling factors. All exclusions are given at the 95% CL.

Table of contents

List of Figures

List of Tables

Chapter 1

Introduction

High energy physics deals with elementary particles of matter and interactions between them.

The Standard Model is a theoretical framework that describes all the particles which have been discovered and so far seem to us to be fundamental. The model allows also to calculate their interactions with high degree of accuracy. It has been very successful in describing the results of all experiments over a wide range of energies. The model describes the electromagnetic, weak and strong interactions. The fourth fundamental interaction – gravity – is however not included in the model. There is a single piece of this model still missing, a particle called "the Higgs boson". This particle is a very important ingredient of the theory. It explains the way particles acquire mass. It also gives rise to masses of quarks and leptons, fundamental blocks of matter. The other reason that the Higgs boson is an important part of the model is, that without it the Standard Model is not renormalisable. In the Standard Model the Higgs sector consists of one complex Higgs doublet field. This is the simplest choice that allows the Higgs mechanism to generate the masses of the gauge bosons of the weak interaction. It is however not the only choice – the Higgs mechanism can generate masses also from other kinds of Higgs multiplet fields (e.g. triplets or quadruplets) or can use more than one Higgs multiplet field. A model with a different or extended Higgs sector can be considered to be an alternative to the Standard Model if its predictions are in agreement with experimental results. Extensions of the Standard Model of particle physics can be a source of new physics. It would allow to answer questions that the SM fails to address, e.g. the large number of free parameters or no natural explanation for the mass hierarchy of quarks and leptons, or the CP violation source in the Standard Model which is not sufficient to explain the assymetry between matter and antimatter. Most extensions of the SM introduce new sources of CP violation.

This thesis is dedicated to neutral Higgs bosons searches beyond the Standard Model, in the so called Two-Higgs-Doublet Model. The search is based on data collected by DELPHI experiment at the Large Electron Positron (LEP) collider at the European laboratory for particle physics (CERN) in Geneva, Switzerland.

The outline of this thesis is as follows:

- Chapter 2 presents the theoretical framework for the search and introduces the Higgs mechanism and the Two-Higgs-Doublet Model.

- Chapter 3 describes the experimental setup – the LEP collider and the DELPHI detector.

- Chapter 4 presents Higgs boson production processes, available for LEP1 energies. It also gives motivation for search of Higgs bosons predicted by the Two-Higgs-Doublet Model and introduces the Yukawa process, for which the analysis has been performed.

- Chapter 5 presents the main part of the thesis, where the analysis performed to search for Higgs bosons produced in the Yukawa process at LEP1 is described. To give a full review of the search, complementary analysis, in which the author was not directly involved, is also shortly presented. The search for Higgs bosons A^0 and h^0 in the Yukawa process is described. The analysis concerns $Z^0 \rightarrow b\bar{b}h^0(A^0)$ and $Z^0 \rightarrow \tau^+\tau^-h^0(A^0)$ processes for Higgs bosons masses varying from 4 to 70 GeV/c^2, at energies in the center of mass at and around the Z^0 mass (LEP1 phase).

- In Chapter 6 results of the analysis are presented, in the form of mass-dependent upper bounds on coupling factors for all considered final states. All exclusions are given at the 95% confidence level.

- Chapter 7 summarizes the results.

Chapter 2

The Higgs mechanism

Many predictions of the Standard Model have been tested by various experiments to a remarkable precision. However, the part of the theory known as the Higgs sector (i.e. the Higgs fields and their couplings) has not been verified experimentally. In particular the existence of the neutral Higgs boson, introduced to the model over thirty years ago, has not been experimentally confirmed yet.

In the Standard Model the Higgs sector consists of one complex doublet of Higgs fields. This is the simplest choice that allows the Higgs mechanism to generate the masses of the gauge bosons of the weak interaction ($\mathrm{W}^{\pm}$ and Z^0). It is, however, not the only choice. The Higgs mechanism can generate masses also from other kinds of Higgs multiplet fields (e.g. triplets or quadruplets) or can use more than one Higgs multiplet field.

In this chapter a phenomenological description of the Higgs mechanism will be given. The aim of it is to explain the Higgs mechanism in the simplest case and then introduce a frame, appropriate for application in the Weinberg–Salam Model (a *minimal* frame). Certain extensions of the minimal frame will be given, as the analysis described here, is connected to these extensions.

As it is often emphasized, the Higgs sector of the Standard Model is not understood from a fundamental point of view, although it performs technically in an entirely satisfactory way as an effective low energy theory.

2.1 The Standard Model

The Standard Model of the electroweak and strong interactions is the simplest theory describing the fundamental constituents of matter and their interactions in agreement with all known experimental data. At the scale of the subatomic world the effects of gravity can be neglected with respect to the other three fundamental forces: electromagnetic, weak and strong.

During the 1960's, Salam, Weinberg and Glashow combined electromagnetic interactions (based on the Quantum Electrodynamics Theory - QED) with weak interactions into the $SU(2)_L \otimes U(1)_Y$ gauge theory. In 1964 Gell-Mann and Zweig independently proposed hypothetical fundamental particles - *quarks* (q), fermions with $\frac{1}{2}\hbar$ spin and fractional charge to describe the great number of observed particles (hadrons) as sets of quarks. One class of hadrons, *baryons*, consist of three quarks (qqq) or three anti-quarks ($\bar{q}\bar{q}\bar{q}$). Another one, *mesons*, are built of a quark and an anti-quark ($q\bar{q}$). Each class can be divided into different groups (*multiplets*). Today's knowledge brings us six kinds (*flavours*) of quarks: u (up), d (down), c (charm), s (strange), t (top), b (bottom, or beauty), and six kinds of anti-quarks (denoted by $\bar{u}$, $\bar{d}$, $\bar{s}$, $\bar{c}$, $\bar{b}$, $\bar{t}$). As well as leptons, quarks are grouped in three *families* (*generations*)[1], in doublets and singlets of a representation of the symmetry group $SU(2)$:

Fermions	Generations			I$_3$	Y	Q
Quarks	$\begin{pmatrix} u \\ d \end{pmatrix}_L$	$\begin{pmatrix} c \\ s \end{pmatrix}_L$	$\begin{pmatrix} t \\ b \end{pmatrix}_L$	$+1/2$ $-1/2$	$+1/3$ $-1/3$	$+2/3$ $-1/3$
	u_R	c_R	t_R	0	$+4/3$	$+2/3$
	d_R	s_R	b_R	0	$-2/3$	$-1/3$
Leptons	$\begin{pmatrix} \nu_e \\ e \end{pmatrix}_L$	$\begin{pmatrix} \nu_\mu \\ \mu \end{pmatrix}_L$	$\begin{pmatrix} \nu_\tau \\ \tau \end{pmatrix}_L$	$+1/2$ $-1/2$	-1 -1	0 -1
	e_R	μ_R	τ_R	0	-2	-1

Table 2.1: The fermions of the Standard Model and some of their quantum numbers. The electric charge Q of a particle is related to its hypercharge Y and the third component of the weak isospin I_3 by: $Q = I_3 + \frac{1}{2}Y$. Indexes L and R stand for Left and Right helicity.

The classification reflects the existence of a symmetry, present in the weak interaction. The weak isospin is a conserved quantum number in the weak interaction and $SU(2)$ is a representation of isospin symmetry. In Table 2.1 the down type quarks (d, s, b) are the eigenstates of the quarks under the weak interaction, which are not the same as the mass eigenstates. The two eigenstates are related by the unitary Cabibbo–Kobayashi–Masakawa (CKM) mixing matrix (as described in *Review of particle physics* [1]):

$$\begin{pmatrix} d \\ s \\ b \end{pmatrix}_{weak} = \begin{pmatrix} V_{ud} & V_{us} & V_{ub} \\ V_{cd} & V_{cs} & V_{cb} \\ V_{td} & V_{ts} & V_{tb} \end{pmatrix} \begin{pmatrix} d \\ s \\ b \end{pmatrix}_{mass} \tag{2.1}$$

The electroweak sector of the Standard Model is described as a $SU(2) \times U(1)$ gauge theory. In it's basic form it describes all the electroweak interactions between fermions by the exchange of massless vector bosons [2].

The lagrangian density of the free massless boson fields takes form:

$$\mathcal{L}^B = -\frac{1}{4}F_{B\mu\nu}(x)F_B^{\mu\nu}(x) - \frac{1}{4}F^i_{W\mu\nu}(x)F_W^{i\mu\nu}(x) \tag{2.2}$$

[1]The same classification is applied to antiparticles, which have opposite quantum numbers and helicity.

The field tensors $F_B^{\mu\nu}$ and $F_W^{i\mu\nu}$ are defined as:

$$F_B^{\mu\nu} = \partial^\nu B^\mu - \partial^\mu B^\nu \tag{2.3}$$

$$F_W^{i\mu\nu} = \partial^\nu W^{i\mu} - \partial^\mu W^{i\nu} \tag{2.4}$$

where B_μ is the U(1) gauge field and W_μ^i, i=1, 2, 3 are the SU(2) gauge fields. Through the following transformations:

$$A_\mu = cos\theta_W B_\mu + sin\theta_W W_\mu^3 \tag{2.5}$$

$$Z_\mu = sin\theta_W B_\mu - cos\theta_W W_\mu^3 \tag{2.6}$$

$$W_\mu^\pm = \frac{1}{\sqrt{2}}(W_\mu^1 \mp iW_\mu^2) \tag{2.7}$$

where the Weinberg angle θ_W is a free parameter, $W_\mu^\pm$, Z_μ and A_μ describe charged, and neutral electroweak force carriers, respectively. The lagrangian 2.2 can be written as:

$$\mathcal{L}^B = -\frac{1}{4}F_{\mu\nu}(x)F^{\mu\nu}(x) - \frac{1}{2}F_{W\mu\nu}(x)F_W^{\mu\nu}(x) - \frac{1}{4}F_{Z\mu\nu}(x)F_Z^{\mu\nu}(x) \tag{2.8}$$

where $F^{\mu\nu}$ is the electromagnetic field tensor and $F_W^{\mu\nu}$ and $F_Z^{\mu\nu}$ are the field tensors for $W^\pm$ and Z fields. The W and Z fields can be made massive by including terms:

$$m_W^2 W_\mu(x)W^\mu(x) + \frac{1}{2}m_Z^2 Z_\mu(x)Z^\mu(x) \tag{2.9}$$

However introducing masses this way causes the lagrangian density to be no longer invariant under an U(1) gauge transformation

$$\psi(x) \rightarrow \psi^{'}(x) = \psi(x)e^{iY\xi(x)} \tag{2.10}$$

where ψ is a boson field with weak hypercharge Y and $\xi(x)$ is differentiable function. The lagrangian including the mass terms will neither be invariant under SU(2) transformations. The theory is also not renormalisable.

The way to give W and Z vector bosons mass, keeping the gauge theory SU(2)×U(1) invariant is spontaneous symmetry breaking.

2.2 The Higgs Mechanism

It appears that the basic lagrangian for weak interactions is invariant under a local gauge symmetry [3]. However, the observation of masses of bosons and fermions participating in weak interactions shows that such a symmetry is not manifested, at least under the conditions of present experiments. In models of weak interactions, the *spontaneous symmetry breaking* is usually achieved by the Higgs mechanism.

Let us explain, what *spontaneous symmetry breaking* means. If a lagrangian in a theory or model has a symmetry S, equations of motion, arising from the lagrangian are also S–symmetric. The *spontaneous S–symmetry breaking* occurs, if solutions of those equations, describing fundamental state of a physical system, do not have full S–symmetry of the lagrangian (i.e. they are partly S–symmetric, or they are not symmetric at all).

2.2.1 The discrete global symmetry

A lagrangian of a fundamental, real scalar field $\phi = \phi(x)$, where x is a timespace coordinate[2], is given by:

$$\mathcal{L} = T - V(\phi) = \frac{1}{2}(\partial_\alpha\phi)(\partial^\alpha\phi) - (\frac{1}{2}\mu^2\phi^2 + \frac{1}{4}\lambda\phi^4) \tag{2.11}$$

where

$$T = \frac{1}{2}(\partial_\alpha\phi)(\partial^\alpha\phi)$$

is the kinetic part and

$$V(\phi) = (\frac{1}{2}\mu^2\phi^2 + \frac{1}{4}\lambda\phi^4)$$

is the potential part of the lagrangian. The potential has two free parameters: μ and λ. The expression $\frac{1}{2}\mu^2\phi^2$ is called a *mass part*. The parameter μ should not be treated as squared field mass, but just as a parameter with the dimension of the mass. The expression $\frac{1}{4}\lambda\phi^4$ describes selfinteraction of the field, characterized by a *dimensionless* constant λ.

The langrangian $\mathcal{L}$ is invariant under both global and discrete transformation of the ϕ field: $\phi \leftrightarrow -\phi$. That means it describes equally well two physical systems, ϕ and $-\phi$. Let us consider any of them. The system has the minimal energy when its kinetic and potential energies have their minima. Assuming $\phi = const$, where kinetic energy has its minimum, let us minimize the potential part.

The potential $V(\phi)$ has its extremum for

[2]The dependence of the ϕ field and other fields introduced in this chapter on x will not be explicitly written for readabilitity of equations.

$$\frac{\partial V(\phi)}{\partial \phi} = 0, \tag{2.12}$$

what gives:

$$\phi(\mu^2 + \lambda\phi^2) = 0 \tag{2.13}$$

The solutions are:

$$\phi = 0 \qquad \phi_{min} = \pm\sqrt{\frac{-\mu^2}{\lambda}} \equiv \pm v \tag{2.14}$$

$V(\phi)$ has a minimum, when $\lambda > 0$. If the other parameter, μ^2 is greater than 0, $\mu^2 > 0$, μ is a real number and can be treated as the field mass, and the potential $V(\phi)$ attains its minimum for $\phi = 0$. Now we have one global minimum of the potential (Figure 2.1a). For $\mu^2 < 0$ and for $\lambda > 0$ the minimum of the potential is not at $\phi = 0$ (Figure 2.1b). On the contrary, $V(\phi)$ has a local maximum there. It means that the system is unstable for the value of $\phi = 0$. Any small perturbation[3] can move the system from the unstable state of $\phi = 0$ to one of the two local minima. The choice of one of the two possible states of degenerated vacuum is called the *spontaneous breaking of the initial symmetry of the lagrangian.* After that the system state is not symmetric anymore and the solution of the equations of motion of the system is also not symmetric.

The $V(\phi)$ local minimum values $\phi = \pm v$ are called ϕ field *vacuum values.* For further description one has to choose one of the values of $\pm v$ to break the symmetry. For small oscillations and the value $+v$, after first-term expansion one obtains:

$$\phi(x) = v + \chi(x) \tag{2.15}$$

In the vacuum state the oscillations vanish (because of the vacuum value v). We have:

$$\begin{aligned} <0|\phi|0> &= v && (2.16)\\ <0|\chi|0> &= 0 && (2.17) \end{aligned}$$

Applying 2.15 to 2.11 one gets:

$$\begin{aligned} \mathcal{L} &= \frac{1}{2}[\partial_\alpha(v+\chi)][\partial^\alpha(v+\chi)] - \Big[\frac{1}{2}\mu^2(v+\chi)^2 + \frac{1}{4}\lambda(v+\chi)^4\Big] = \\ &= \frac{1}{2}(\partial_\alpha\chi)(\partial^\alpha) - \Big\{\frac{1}{2}\mu^2\Big[v^2 + 2v\chi + \chi^2\Big] + \end{aligned}$$

[3]A small perturbation means small in comparison to the characteristic energies of the system, e.g. self interaction energy

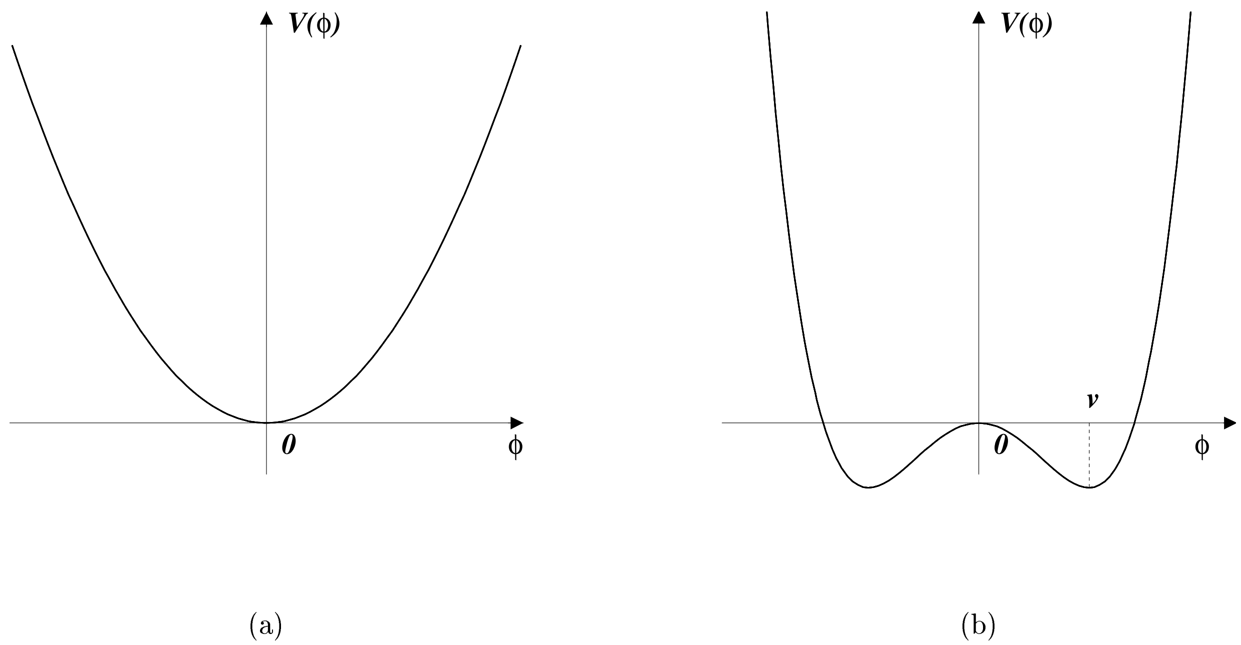

Figure 2.1: The shape of the $V(\phi)$ potential, defined as $V(\phi) = \frac{1}{2}\mu^2\phi^2 + \frac{1}{4}\lambda\phi^4$, for parameters: (a) λ >0 and μ^2 >0 and (b) λ >0 and μ^2 <0.

$$\begin{aligned} & \frac{1}{4}\lambda\Big[v^4 + 4v^3\chi + 6v^2\chi^2 + 4v\chi^3 + \chi^4\Big]\Big\} = \\ = \; & \frac{1}{2}(\partial_\alpha\chi)(\partial^\alpha\chi) - \Big\{\frac{v^2}{2}(\mu^2 + \frac{1}{2}\lambda v^2) + v(\mu^2 + \lambda v^2)\chi + \\ & \frac{1}{2}(\mu^2 + 3\lambda v^2)\chi^2 + \lambda v\chi^3 + \frac{1}{4}\lambda\chi^4\Big\} \end{aligned} \tag{2.18}$$

Using 2.14, the lagrangian can be written as:

$$\mathcal{L} = \frac{1}{2}(\partial_\alpha\chi)(\partial^\alpha\chi) + \frac{1}{4}\lambda v^4 - \frac{1}{2}(2\lambda v^2)\chi^2 - \lambda v\chi^3 - \frac{1}{4}\lambda\chi^4 \tag{2.19}$$

The expression $\frac{1}{2}(2\lambda v^2)\chi^2$ is a mass term and contains the mass of the field χ. Therefore, after the spontaneous symmetry breaking the lagrangian describes oscillations of the massive field χ around non-zero vacuum value v of the ϕ field. The mass of the field, on the tree level (in the Born approximation) is given by:

$$m_\chi = \sqrt{2\lambda v^2} = \sqrt{-\mu^2} \tag{2.20}$$

The langrangian 2.19 contains terms describing selfinteraction of the field χ (i.e. $-\lambda v\chi^3 - \frac{1}{4}\lambda\chi^4$). These terms, as well as the mass term, contain a free theory parameter – λ. Therefore we can define neither mass of the χ field, nor the strength of its selfinteractions. In the theory we acquire a massive fundamental particle – a spin 0 boson χ of unknown mass.

A more detailed discussion on this subject can be found in a publication by J. Iliopoulos [4].

2.2.2 Continuous abelian global symmetry

Let us replace now the scalar real field, described in the previous section, with a scalar complex one. We denote it ϕ again, and it contains two real fields, ϕ_1 and ϕ_2:

$$\phi = \frac{1}{\sqrt{2}}(\phi_1 + i\phi_2) \tag{2.21}$$

The lagrangian, describing ϕ field is given by:

$$\mathcal{L}_2 = (\partial_\alpha\phi)(\partial^\alpha\phi)^* - \mu^2\phi\phi^* - \lambda(\phi\phi^*)^2 \tag{2.22}$$

The lagrangian is invariant under a global gauge transformation, described with a θ parameter:

$$\phi \to \phi' = e^{-i\theta}\phi \tag{2.23}$$

where θ is a real number. The potential $V(\phi)$ is shown in Figure 2.2a.
The lagrangian 2.22, expressed with ϕ_1 and ϕ_2 is given by:

$$\mathcal{L}_2 = \frac{1}{2}(\partial_\alpha\phi_1)(\partial^\alpha\phi 1) + \frac{1}{2}(\partial_\alpha\phi_2)(\partial^\alpha\phi 2) - \frac{1}{2}\mu^2(\phi_1^2 + \phi_2^2) - \frac{1}{4}\lambda(\phi_1^2 + \phi_2^2)^2 \tag{2.24}$$

The minimum of the potential we find for $\phi =$ const., and with

$$\rho \equiv \phi\phi^* = \frac{\phi_1^2 + \phi_2^2}{2} \tag{2.25}$$

one gets (for $\lambda > 0$):

$$V(\rho) = \mu^2\rho + \lambda\rho^2 \tag{2.26}$$

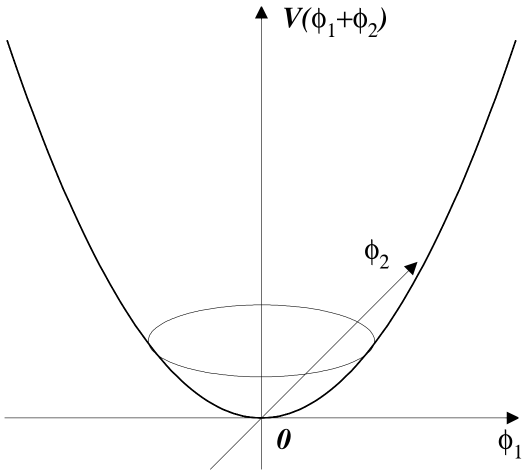

(a)

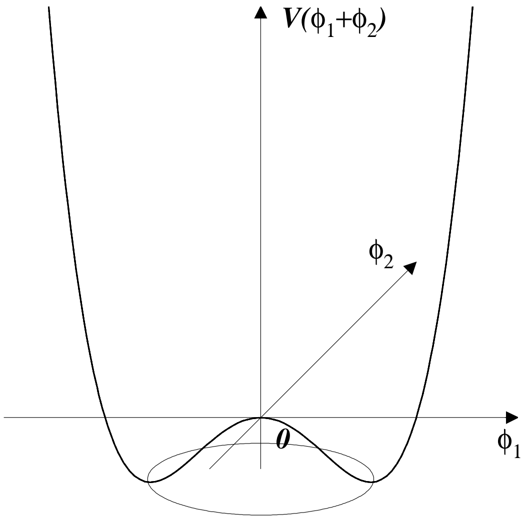

(b)

Figure 2.2: The shape of the $V(\phi)$ potential (two-dimension), defined by (2.22), for parameters: (a) λ >0 and μ^2 >0 and (b) λ >0 and μ^2 <0.

For $\mu^2 > 0$ the potential global minimum is at $\phi = 0$. It is a symmetrical solution. For this case the μ parameter (which is a real number) can be identified with the mass of the ϕ field. Therefore in this model one has two different scalar bosons, ϕ_1 and ϕ_2 of identical masses μ.

Let us consider the case where $\mu^2 < 0$. The potential of this case is shown in Figure 2.2b. The minimum of the potential is now for:

$$\rho_{min} = -\frac{\mu^2}{2\lambda} = \frac{\phi_{1\ min.}^2 + \phi_{2\ min.}^2}{2} \tag{2.27}$$

In the case of a lagrangian with a complex field one gets an infinite set of vacuum values, minimizing the potential. The solution is non-symmetric and the vacuum values (of the degenerated vacuum) are given by:

$$v \equiv |\phi_{min.}| = \sqrt{\phi_{min.}.\phi_{min.}^*} = \sqrt{\phi_{1\ min.}^2 + \phi_{2\ min.}^2} \tag{2.28}$$

Any non-symmetric vacuum state can be written as:

$$\phi_0 = |\phi_{min.}|e^{i\varphi} = \frac{v}{\sqrt{2}}e^{i\varphi} \equiv \frac{v}{\sqrt{2}}(cos\varphi + isin\varphi), \tag{2.29}$$

where φ is an azimuthal angle (a real number in the interval of $0 \leq \varphi \leq 2\pi$) in the the (ϕ_1, ϕ_2) plane. To go to further consideration one has now to choose one of vacuum values of the ϕ field, what means one *spontaneously breaks the symmetry*. Let us choose then: $\varphi = 0$, $\phi_{1\ min.} = v$ and $\phi_2 = 0$. We consider now small oscillations on the chosen vacuum value of the field ϕ. Let us expand the ϕ field and consider only the first term of the expansion:

$$\phi(x) = \frac{1}{\sqrt{2}}(v + \chi(x) + i\zeta(x)) \tag{2.30}$$

χ and ζ fields are real fields and they describe possible oscillations of the ϕ filed in two independent and orthogonal directions. Applying the expansion 2.30 to the lagrangian 2.22 one gets:

$$\begin{aligned}
\mathcal{L}_2 &= \frac{1}{2}[\partial_\alpha(\chi + i\zeta)\partial^\alpha(\chi + i\zeta)^*] - \frac{1}{2}\mu^2(v + \chi + i\zeta)(v + \chi + i\zeta)^* + \\
&\quad -\frac{\lambda}{4}[(v + \chi + i\zeta)(v + \chi + i\zeta)^*]^2 = \\
&= \frac{1}{2}(\partial_\alpha\chi)(\partial^\alpha\chi) + \frac{1}{2}(\partial_\beta\zeta)(\partial^\beta\zeta) - \frac{1}{2}\mu^2[v^2 + 2v\chi + \chi^2 + \zeta^2] + \\
&\quad -\frac{\lambda}{4}[(v + \chi)^4 + 2(v + \chi)^2\zeta^2 + \zeta^4] = \\
&= \frac{1}{2}(\partial_\alpha\chi)(\partial^\alpha\chi) + \frac{1}{2}(\partial_\beta\zeta)(\partial^\beta\zeta) + \frac{\lambda}{4}v^4 - \frac{1}{2}(2\lambda v^2)\chi^2 - 0\zeta^2 + \\
&\quad -\lambda v(\chi^3 + \chi\zeta^3) - \frac{\lambda}{4}\chi^4 - \frac{\lambda}{4}\zeta^4 - \frac{\lambda}{2}\chi^2\zeta^2
\end{aligned} \tag{2.31}$$

The terms $\frac{1}{2}(2\lambda v^2)\chi^2$ and $(-0\zeta^2)$ are mass terms. The latter one has zero next to the ζ field. It means that after the symmetry breaking the ζ field and a boson of the field remain massless. This boson is called *Goldstone (Nambu-Goldstone) boson*. Similar to the foregoing case of the discrete symmetry, one can see that all self-interaction terms as well as mass term for the χ filed contain the λ parameter, therefore one can estimate neither mass of the χ field nor strength of the self-interaction in the considered model. The term with the third power of χ and ζ fileds breaks invariance of the lagrangian under the transformation 2.23. Therefore, after the spontaneous symmetry breaking one gets a massive χ scalar boson, with mass $m_\chi = v\sqrt{2\lambda}$ and massless Goldstone boson ζ, which is a result of the spontaneous symmetry breaking [5, 6].

In such type of models after the spontaneous symmetry breaking, equations of motion have reduced symmetry with relation to lagrangian and contain massless bosons. Such a model cannot be applied for vector bosons, because it would break Lorenz invariance of the model.

However, the Salam–Weinberg Model has *local* continuous gauge symmetry, what makes the Higgs mechanism work.

A more detailed discussion on this subject can be found in [4] and [7].

2.2.3 Continuous abelian local gauge symmetry - the Higgs mechanism

We consider now a U(1) gauge invariant lagrangian of a complex scalar field $\phi = \frac{1}{\sqrt{2}}(\phi_1 + i\phi_2)$ with a massless gauge boson A_μ. The lagrangian of the interaction is given by:

$$\mathcal{L} = (D_\mu\phi)(D^\mu\phi)^* - \mu^2\phi\phi^* - \lambda(\phi\phi^*)^2 - \frac{1}{4}F_{\mu\nu}F^{\mu\nu} \tag{2.32}$$

where:

$$D_\mu = \partial_\mu - igA_\mu \tag{2.33}$$

$$F_{\mu\nu} = \partial_\mu A_\nu - \partial_\nu A_\mu \tag{2.34}$$

and g is a coupling constant of the interaction of the model. The lagrangian 2.32 is invariant under following local gauge transformations:

$$\phi(x) \rightarrow \phi^{'}(x) = e^{-i\theta(x)}\phi(x) \tag{2.35}$$

$$D_\mu\phi(x) \rightarrow D^{'}_\mu\phi^{'}(x) = e^{-i\theta(x)}[D_\mu\phi(x)] \tag{2.36}$$

$$A_\mu(x) \rightarrow A^{'}_\mu = V_\mu(x) - \frac{1}{g}\partial_\mu\theta(x) \tag{2.37}$$

where the phase θ of the ϕ field is a function of (x). As previously we consider $\lambda > 0$. For $\mu^2 > 0$ the V(ϕ) potential has its minimum for $\phi = 0$ and it is of shape shown in Figure 2.2a. The solution is symmetric and stable. The particle spectrum contains two massive scalar bosons, ϕ_1 and ϕ_2, each of mass μ. There is also one massless vector gauge field V$_\mu$.

For the case of $\mu^2 < 0$ the potential has the shape as shown in Figure 2.2b. The minimum energy corresponds to degenerate value of ϕ as a ring in the complex plane

$$\phi_{min} = \frac{v}{\sqrt{2}} = \sqrt{\frac{-\mu^2}{\lambda}} \tag{2.38}$$

and

$$\phi_0 = |\phi_{min}|e^{i\varphi} = \sqrt{\frac{-\mu^2}{2\lambda}}e^{i\varphi}, \quad 0 \le \varphi \le 2\pi. \tag{2.39}$$

where φ is an azimuthal angle counted from ϕ_1 axis towards ϕ_2 axis. As the lagrangian 2.32 is invariant under rotations in the complex plane of ϕ, any direction is equally good and with $\varphi = 0$:

$$\phi_0 = \phi_{min} = \sqrt{\frac{-\mu^2}{2\lambda}} \equiv \frac{v}{\sqrt{2}} \tag{2.40}$$

and

$$< 0|\phi_1|0 >= v, \qquad < 0|\phi_2|0 >= 0. \tag{2.41}$$

With a chosen ϕ the symmetry is broken. Extension of the minimum can be described with two real fields, χ and ζ:

$$\phi(x) = \frac{1}{\sqrt{2}}(v + \chi(x))e^{i\zeta(x)/v} = \frac{1}{\sqrt{2}}(v + \chi(x) + i\zeta(x) + ...) \tag{2.42}$$

One can identify fields χ and ζ with ϕ_1 and ϕ_2:

$$\chi = \phi_1 - v, \qquad \zeta = \phi_2 \tag{2.43}$$

One can make a suitable choice of the particular gauge function

$$\theta(x) = \frac{\zeta(x)}{v} \tag{2.44}$$

the expression 2.35 can be written as

$$\begin{aligned} \phi(x) \to \phi'(x) &= e^{-i\zeta(x)/v}\phi(x) = e^{-i\zeta(x)/v}[\frac{e^{i\zeta(x)/v}}{\sqrt{2}}(v + \chi(x))] = \\ &= \frac{1}{\sqrt{2}}(v + \chi(x)) \end{aligned} \tag{2.45}$$

The lagrangian 2.32 takes now form:

$$\mathcal{L} = -\frac{1}{4}F_{\mu\nu}F^{\mu\nu} + \frac{1}{2}g^2v^2A'_\mu A'^\mu + \frac{1}{2}(\partial_\mu\chi)^2 - \frac{1}{2}(2\lambda v^2)\chi^2 - \frac{1}{4}\lambda\chi^4 + \frac{1}{2}g^2(2v\chi + \chi^2)A'_\mu A'^\mu \tag{2.46}$$

In above form the lagrangian describes interaction of the massive vector boson $A_\mu^{'}$ with massive real field χ, which is called Higgs field. The Higgs boson and the $A^{'}$ boson masses are given by

$$m_\chi = \sqrt{2\lambda v^2}, \qquad m_{A'} = gv \tag{2.47}$$

To summarise: a complex scalar field and a masselss vector field, both with two degrees of freedom, as a result of the Higgs mechanism were transformed into one real scalar field of one degree of freedom and a massive vector boson field of three degrees of freedom. A massless spin 1 particle has two transverse polarised states while a massive spin 1 particle has an additional longitudinal polarised state. By choosing a specific gauge ζ field disappeares, if the ζ bosons are massless. It requires the vacuum state to be degenerate.

In order to extend presented Higgs mechanism from U(1) to SU(2)×U(1) gauge invariant Lagrangian of the electroweak theory one has to start with a complex scalar doublet:

$$\Phi = \begin{pmatrix} \phi^+ \\ \phi^0 \end{pmatrix} = \frac{1}{\sqrt{2}} \begin{pmatrix} \phi_1 + i\phi_2 \\ \phi_3 + i\phi_4 \end{pmatrix}, \tag{2.48}$$

and four massless vector bosons. There are four degrees of freedom from the scalar fields and eight from the vector bosons. Through the Higgs mechanism free massless boson fields in the lagrangian are transformed into one real scalar, three massive vector and one massless vector boson. The massless vector boson is to be identified with the photon and the single remaining scalar with the Higgs boson. Counting degrees of freedom again gives one from the Higgs boson, two from the photon and nine from the massive vector bosons.

Parameters in the potential

$$V(\Phi) = \mu^2 \Phi^\dagger \Phi + \lambda(\Phi^\dagger \Phi)^2 \tag{2.49}$$

are again λ >0 and μ^2 <0. The symmetry is broken by chosing

$$< 0|\Phi|0 >= \frac{1}{\sqrt{2}} \begin{pmatrix} 0 \\ v \end{pmatrix}, \qquad v = \sqrt{\frac{-\mu^2}{\lambda}} \tag{2.50}$$

what corresponds to $\phi_1 = \phi_2 = \phi_4 = 0$ and $\phi_3 = v$. One can parametrize the Φ doublet:

$$\Phi(x) = U^{-1}(\Xi(x)) \frac{1}{\sqrt{2}} \begin{pmatrix} 0 \\ v + H(x) \end{pmatrix} = \frac{1}{\sqrt{2}} e^{\frac{-i\xi_A(x)\sigma_A}{v}} \begin{pmatrix} 0 \\ v + H(x) \end{pmatrix}, \quad A = 1,2,3 \tag{2.51}$$

where $\Xi(x) = (\xi_1(x),\ \xi_2(x),\ \xi_3(x))$; σ_A are the generators of the SU(2) group. Expanding in small oscillations the fields around vacuum state, we have:

$$\Phi(x) = \frac{1}{\sqrt{2}}(v + h(x) + i\sigma_1\xi_1(x) + i\sigma_2\xi_2(x) + i\sigma_3\xi_3(x)) \begin{pmatrix} 0 \\ 1 \end{pmatrix} \tag{2.52}$$

and

$$< 0|H|0 >=< 0|\xi_A|0 >= 0, \qquad A = 1,\ 2,\ 3. \tag{2.53}$$

The lagrangian is invariant under local unitary gauge transformation:

$$\Phi(x) \to \Phi^{'}(x) = \phi(x)e^{i\sigma_A\theta_A(x)} \equiv U(\Theta(x))\Phi(x) \tag{2.54}$$

Parameters $\theta_A(x)$ are real numbers and $\Theta(x) = (\theta_1(x),\ \theta_1(x),\ \theta_1(x))$. One can set the parameters as:

$$\theta_A(x) = \xi_A(x), \quad A = 1,\ 2,\ 3. \tag{2.55}$$

The transformation 2.54 takes therefore the form:

$$\Phi(x) \to \Phi^{'}(x) = U(\Xi(x))\Phi(x) = \frac{1}{\sqrt{2}} \begin{pmatrix} 0 \\ v + H(x) \end{pmatrix} \tag{2.56}$$

In the analogous way for the previous example $\xi_A(x)$ fields disappear as longitudinal polarisation states and the gauge fields become massive.

Introducing masses of the vector bosons with one doublet of complex scalar fields is the simplest scenario. In principle, an infinite number of scalar fields can be introduced.

Masses of the particles in the standard model are given by:

$$m_H = \sqrt{2\lambda v^2}, \qquad m_W = \frac{1}{2}vg_2, \qquad m_Z = \frac{v}{2}\sqrt{g_1^2 + g_2^2} = \frac{m_W}{cos\theta_W}, \qquad m_\gamma = 0 \tag{2.57}$$

where g_1 and g_2 are coupling constant connected to U(1) and SU(2) groups, respectively, and θ_W the Weinberg angle. The vacuum expectation value can be extracted as

$$v = \frac{2m_W}{g_2} = 246 \text{ GeV} \tag{2.58}$$

but one can not establish the value of λ before measuring the Higgs mass.

A more detailed discussion on this subject can be found in [7] and [8].

2.2.4 Massive fermions

The gauge bosons have acquired mass through the spontaneous symmetry breaking via the Higgs mechanism. This mechanism has direct no influence on the mass of the fermions. However the Yukawa coupling between the scalar Higgs field and the fermions may generate their masses. While terms like $m_f\bar{f}f$ are not allowed in gauge invariant an renormalizable model, it is possible to build up mass terms for fermions containing scalar fields. In the full electroweak and Higgs sector part of the Standard Model lagrangian, the fermion-Higgs interaction term is

$$\mathcal{L}_{FH} = -\frac{1}{v} m_f \bar{\psi}_f \psi_f g_f. \tag{2.59}$$

For each fermion there is a specific coupling constant g_f, which is a free parameter. The effective interaction gives rise to a fermion mass of:

$$m_f = g_f \frac{v}{\sqrt{2}} \tag{2.60}$$

While it is impossible to put constraints on the Higgs mass and the Higgs-fermion couplings, one can see that the Higgs particle will couple to the fermion in proportion to their mass.

2.3 Extensions of the Standard Model

The choice of one doublet of scalar fields in the Higgs mechanism is called Standard Model (SM). A priori other multiplets can be used for Higgs mechanism, and moreover a more complex structure of the scalar sector could explain the difference between fermion masses and can give a new source of CP violation. Actually in the SM the CP violation source is included in the complex phase of CKM mixing matrix elements. However this source is not sufficient to explain the asymmetry between matter and antimatter in the universe [9]. Models in which the scalar sector has more than one doublet give new potential sources of CP asymmetry and make possible the baryogenesis at the scale of the weak interaction. There are more reasons to introduce a more complex structure in the scalar sector of SM, which will be explained in this section. As there is not much experimental information about Higgs sector, one should check also the implications of the more complicated Higgs sectors, both in the Standard Model and its extensions [8]. The extensions may contain additional scalar fields with non-zero vacuum value, and they may be singlets, doublets, triplets, or higher representations of SU(2) group of weak isospin that result in more Higgs particles. However the most common extensions are with Higgs doublets. They do not require fine tuning of Higgs potential parameters to give model properties in a good agreement with precise electroweak measurements.

In two-doublet extensions of the Higgs sector of the Weinberg-Salam model the ρ parameter, defined as

$$\rho = \frac{M_W^2}{M_Z^2 cos^2\theta_W} \tag{2.61}$$

is very close to 1 [10, 11]. This constraint is satisfied at the tree-level in a model with Higgs singlets and doublets, without any adjustment of parameters of the model [12]. Any version of the Standard Model with any number of Higgs doublets will satisfy this property. However, there are other ways to satisfy the $\rho \simeq 1$ constraint, which is discussed in [8].

Another major theoretical constraint on the Higgs sector comes from experimental limits on the FCNC (Flavour-Changing Neutral Currents). In the minimal Higgs sector FCNC at the tree-level are not present. This requirement has to be satisfied in non-minimal Higgs models. The solution is based on a theory of Glashow and Weinberg [13] and concerns FCNC in models with more than one Higgs doublet. It satisfies the FCNC condition if all fermions of a given electric charge couple to only one Higgs doublet (discussed in the book by J. F. Gunion et.al. [8]).

There are other conditions that must be satisfied by any model of electroweak symmetry breaking and they are described i.e. in the book by J. F. Gunion *et.al.* [8]. The conclusion is that there is some freedom in the Higgs sector, although the choice is not completely arbitrary. Models with multiple doublets are preferred for non-minimal Higgs structures [8]. The 2-Higgs-Doublet extension of the Standard Model is particulary attractive because it adds new phenomena, e.g. charged Higgs bosons ($H^{\pm}$). It is also the very minimal extension, i.e. it adds the fewest new arbitrary parameters. It satisfies theoretical constraints of $\rho \simeq 1$ and the absence of FCNC at the tree level (with apropriately chosen Higgs-fermion coupling).

2.3.1 2-Higgs-Doublet Model – General analysis

2HDM stands for 2-Higgs-Doublet Model. It describes the simplest Higgs sector extension in the Standard Model to two doublets. The Standard Model will be called here either SM or 1HDM (1-Higgs-Doublet Model).

We introduce two doublets Φ_1 and Φ_2 of $SU(2)_L$ made by complex scalar fields of hypercharge $Y(\Phi_1) = Y(\Phi_2 = 1$:

$$\Phi_1 = \begin{pmatrix} \phi_1^+ \\ \phi_1^0 \end{pmatrix} = \frac{1}{\sqrt{2}} \begin{pmatrix} \varphi_1 + i\varphi_2 \\ \varphi_3 + i\varphi_4 \end{pmatrix}, \qquad \Phi_2 = \begin{pmatrix} \phi_2^+ \\ \phi_2^0 \end{pmatrix} = \frac{1}{\sqrt{2}} \begin{pmatrix} \varphi_5 + i\varphi_6 \\ \varphi_7 + i\varphi_8 \end{pmatrix} \tag{2.62}$$

The choice of $Y(\Phi_1) = Y(\Phi_2) = 1$ is arbitrary (doublets Φ_1 and $\Phi_2^{'}$ of $Y(\Phi_1) = -Y(\Phi_2^{'}) = 1$ can be used instead).

The most general Higgs potential V(Φ_1, Φ_2) for two doublet model is given by:

$$\begin{aligned} V(\Phi_1,\Phi_2) \; = \; & \lambda_1(\Phi_1^\dagger\Phi_1 - v_1^2)^2 + \lambda_2(\Phi_2^\dagger\Phi_2 - v_2^2)^2 + \\ & \lambda_3[(\Phi_1^\dagger\Phi_1 - v_1^2) + (\Phi_2^\dagger\Phi_2 - v_2^2)]^2 + \\ & \lambda_4[(\Phi_1^\dagger\Phi_1)(\Phi_2^\dagger\Phi_2) - (\Phi_1^\dagger\Phi_2)(\Phi_2^\dagger\Phi_1)] + \\ & \lambda_5[\mathrm{R}e(\Phi_1^\dagger\Phi_2 - v_1 v_2 cos\eta]^2 + \lambda_6[\mathrm{I}m(\Phi_1^\dagger\Phi_2 - v_1 v_2 sin\eta]^2, \end{aligned} \tag{2.63}$$

where λ_i (i = 1,...,6) are, by hermiticity, real parameters. To achieve FCNC suppression the potential 2.63 must be invariant under following discrete symmetries:

$$\Phi_1 \to -\Phi_1 \quad \Phi_2 \to \Phi_2 \quad or \quad \Phi_1 \to \Phi_1 \quad \Phi_2 \to -\Phi_2 \tag{2.64}$$

Analogous symmetries one has to apply to right-handed quarks.

If the parameters λ_i are positive, the potential 2.63 has its minimum at

$$< 0|\Phi_1|0 >= \begin{pmatrix} 0 \\ v_1 \end{pmatrix} \equiv \frac{1}{\sqrt{2}} \begin{pmatrix} 0 \\ v_1^{'} \end{pmatrix}, \quad < 0|\Phi_2|0 >= \begin{pmatrix} 0 \\ v_2 e^{i\eta} \end{pmatrix} \equiv \frac{1}{\sqrt{2}} \begin{pmatrix} 0 \\ v_2^{'} e^{i\eta} \end{pmatrix} \tag{2.65}$$

The parameter η, which is a relative phase of two vacuum expectation values v_1 and v_2 in 2.63 is connected to the CP symmetry. If sin$\eta \neq$0 in the extended models, there is CP violation in the Higgs sector. Let us consider only sinη=0 case.

In the 2HDM and also supersymmetric extensions of the SM [8] the following parameter is introduced:

$$tg\beta \equiv \frac{v_2}{v_1} \tag{2.66}$$

where v_1 and v_2 are vacuum expectation values of the Higgs doublets.

As a result of the Higgs mechanism in the 2HDM, three degrees of freedom are absorbed by longitudinal polarisation of gauge bosons $W^\pm$ and Z bosons while they acquire mass. The remaining five degrees of freedom lead to existence of five physical Higgs bosons:

- two charged bosons: $H^\pm$ of quantum numbers $J^P = 0^+$

- two neutral bosons: H^0, h^0 of quantum numbers $J^{CP} = 0^{++}$
- one neutral boson: A^0 of quantum numbers $J^{CP} = 0^{+-}$

Masses of the bosons are functions of λ_i and v_j ($i = 1, ..., 6$, $j = 1, 2$) and there is a mixing between neutral H and h bosons with the the mixing angle α. Instead of one parameter λ in the Standard Model (1HDM), there are 6 parameters of 2HDM:

$$m_{H^\pm}, \qquad m_{H^0}, \qquad m_{h^0}, \qquad m_{A^0}, \qquad \mathrm{tg}\beta, \qquad \alpha$$

where $m_{H^0} \geq m_{h^0}$, and $\xi = 0$.

With five Higgs bosons there is a great number of possible couplings of the bosons to all particles in the model. A choice of certain couplings has experimental consequences. On the base of C and P quantum numbers of the bosons one can establish Higgs–vector fields allowed couplings within 2HDM (CP symmetry conserving in the Higgs sector). Below some example tree–level couplings of Higgs bosons–gauge fields are listed:

$$W^+W^-H^0,\ W^+W^-h^0,\ Z^0H^+H^-,\ Z^0H^0A^0,\ Z^0Z^0H^0,\ Z^0h^0A^0,\ Z^0Z^0h^0.$$

Higgs bosons H^0 and h^0 couplings to vector fields (denoted by Λ) in the 2HDM are different than in the 1HDM. They may be described by factors:

$$\frac{\Lambda(VVh^0)}{\Lambda(VVh^0_{1HDM})} = sin(\beta - \alpha), \quad \frac{\Lambda(VVH^0)}{\Lambda(VVh^0_{1HDM})} = cos(\beta - \alpha) \tag{2.67}$$

where V denotes vector bosons ($V = W^\pm$, Z^0) and h^0_{1HDM} is 1HDM Higgs boson. In the 2HDM model there are four different types of Higgs bosons-fermions couplings:

type I: all fermions couple only to Higgs field in the Φ_2 doublet, Φ_1 doublet is decoupled from fermions;

type II: *up* quarks couple to Φ_2 doublet, *down* quarks and charged leptons couple to the Higgs field in the Φ_1 doublet; this type of couplings is also present in the Minimal Supersymmetric extension of the Standard Model (MSSM).

type III: *up* quarks and charged leptons couple to Φ_2 doublet, *down* quarks couple to the Φ_1 doublet;

type IV: all quarks couple to the Higgs field in the Φ_2 doublet and charged leptons couple to the Φ_1 doublet.

There are no Higgs bosons couplings to neutrinos; in the Weinberg–Salam model after the Higgs mechanism, neutrinos remain massless, and this feature must be present also in models with extended Higgs sector. We will consider the type II of 2HDM (*2HDM(II)*), because the analysis presented here is devoted to this model.

Higgs–fermion couplings in the 1HDM are defined by:

$$\eta_f = \sqrt{2}\frac{m_f}{v}$$

where η_f is Yukawa coupling, a free parameter of 1HDM. The 2HDM Higgs–fermions couplings can be also described this way. Using 2.57 we get

$$\eta_f = \sqrt{2}\frac{m_f}{v} = \frac{g_2}{\sqrt{2}}\frac{m_f}{M_W} \tag{2.68}$$

As the analysis presented here concerns searches for neutral Higgs bosons, we confine ourselves to present only enhancement (suppression) factors of the neutral 2HDM Higgs bosons couplings to fermions in relation to 1HDM couplings in Table 2.2.

A more detailed discussion on this subject can be found in [8].

Table 2.2: Suppression (enhancement) factors of 2HDM Higgs bosons couplings in relation to 1HDM couplings to fermions. $\Lambda_{\phi f\bar{f}} \equiv \eta(f\bar{f}\phi)/\eta(f\bar{f}h^0_{1HDM})$, and $\phi = H^0$, h^0, A^0

	$u\bar{u}$, $c\bar{c}$, $t\bar{t}$	$d\bar{d}$, $s\bar{s}$, $b\bar{b}$, e^+e^-,$\mu^+\mu^-$,$\tau^+\tau^-$
$\Lambda_{H^0 f\bar{f}}$	$\sin\alpha/\sin\beta$	$\cos\alpha/\cos\beta$
$\Lambda_{h^0 f\bar{f}}$	$\cos\alpha/\sin\beta$	$-\sin\alpha/\cos\beta$
$\Lambda_{A^0 f\bar{f}}$	$-i\gamma_5\mathrm{ctg}\beta$	$-i\gamma_5\mathrm{tg}\beta$

Chapter 3

The experiment

3.1 LEP Accelerator

LEP stands for the **L**arge **E**lectron – **P**ositron collider, at CERN, the European Laboratory for Particle Physics, near Geneva, Switzerland. The machine was the world's largest particle accelerator. The operation of the LEP collider at CERN started in August 1989 and stopped in November 2000. It will be replaced by a new accelerating pp machine – LHC (**L**arge **H**adron **C**ollider). The main ring was situated in an underground tunnel. LEP had a shape of an octagon with rounded corners, with a circumference of 26.7 km. LEP's main goal was the detailed study of the electroweak interaction, by performing precision measurements of the relevant physical quantities and by searching for unexpected features. From 1989 to 1995 LEP was operating at the center-of-mass energy of the Z^0 resonance[1], corresponding to about 91.2 GeV (so called LEP1 phase). In 1995 data was collected at 130–136 GeV. Next year, 1996, run energy was about 161 GeV and also 172 GeV, in 1997 and 1998 – about 183 and 189 GeV respectively (LEP2 phase). In 1999 the center of mass energy reached 200 GeV and in the 2000 year – 209 GeV.

Before electrons and positrons were injected into the LEP ring, they had been accelerated up to energy of 20 GeV by a chain of preaccelerators:

- the LIL1, a 200 MeV electron linear accelerator (LINAC), produced positrons;
- the LIL2, a second LINAC, accelerated electrons and positrons up to 600 MeV;
- the 600 MeV electrons and positrons were then injected into the electron-positron accumulator (EPA), where the beams were then stocked;
- the Proton Synchrotron (PS) and Super Proton Synchrotron (SPS) were used for increasing the energy up to 3.5 GeV and 20 GeV respectively, for the final injection into LEP.

[1]Except of years 1992 and 1994 LEP was operating at variable energies close to Z^0 resonance.

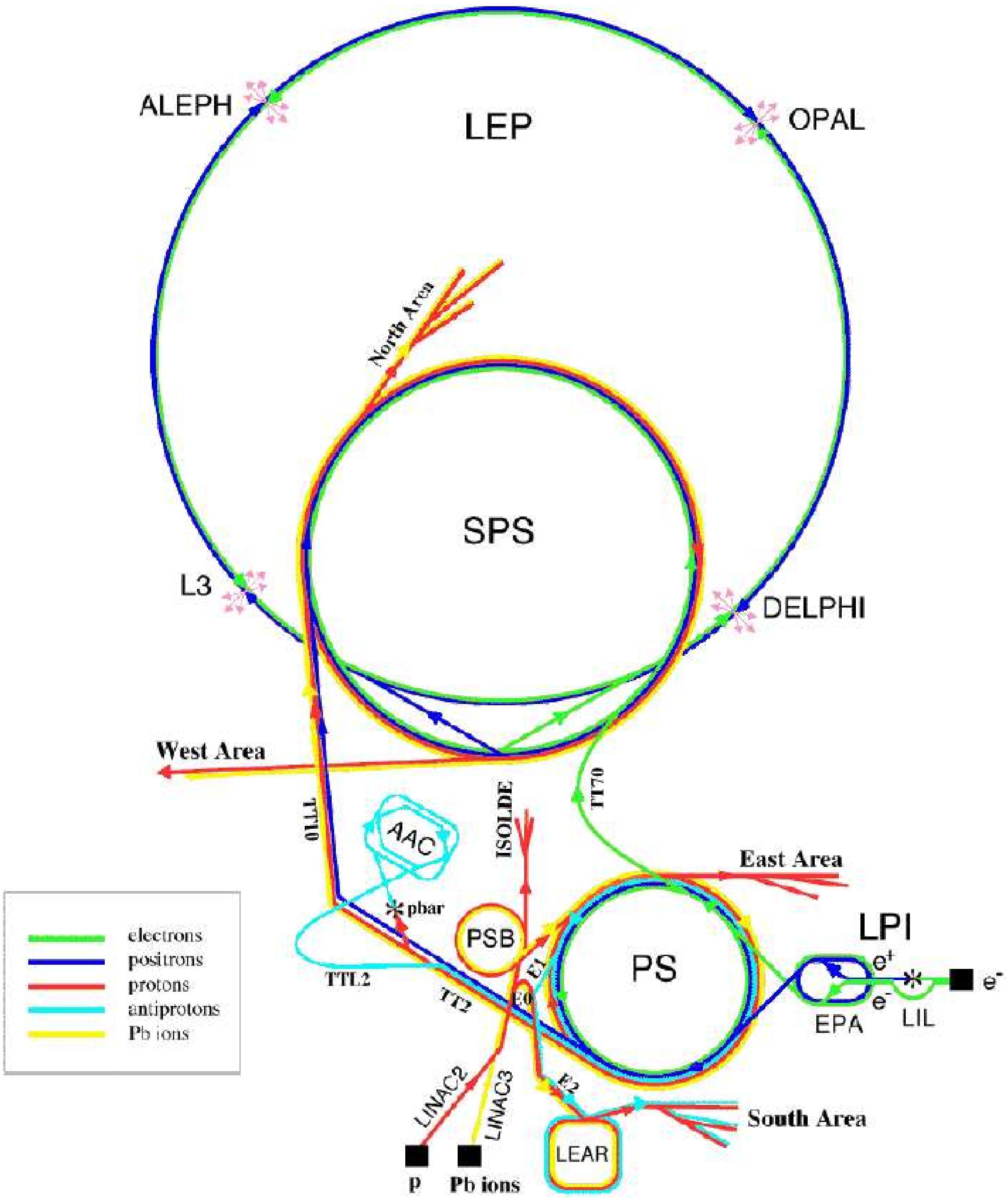

Figure 3.1: The LEP accelerating system

After the injection, beams were accelerated to an energy of about 45 GeV (LEP1 phase) or higher (LEP2 phase). The LEP accelerating system is shown in Figure 3.1. The beams collided at four points in the ring. At these interaction points four detectors - ALEPH (**A**pparatus for **LE**P **PH**ysics), DELPHI (**DE**tector with **L**epton, **P**hoton and **H**adron **I**dentification), L3 (**L**etter of intent **3**) and OPAL (**O**mni **P**urpose **A**pparatus for **L**EP) were installed. The detections systems were, in their global geometry, rather similar. They were essentially 4π detectors surrounding the interaction point. The global structure and main components were closely related to the general physics goals and had a large number of common features. Since the aim was to achieve as complete as possible analysis of the final state, they were general purpose detectors formed by layers of subdetectors with different characteristics.

An important parameter of an accelerator is the luminosity. The luminosity is defined as the number of beam particles that cross the collision region per unit of area per second. It can be expressed in machine parameters:

$$\mathcal{L} = f_{rev} \cdot k \cdot \frac{N^+N^-}{4\pi\sigma_x\sigma_y}[\mathrm{cm}^{-2}\ \mathrm{s}^{-1}\ ] \tag{3.1}$$

where f_{rev} is the LEP revlution frequency (11.25 kHz), k is the number of bunches (4 or 8), N^- and N^+ are the number of electrons and positrons per bunch ($\sim 2.5\times10^{11}$) and σ_x ($\simeq$100μm) and σ_y ($\simeq$10μm) are the bunch dimensions in the plane perpendicular to the beam direction[2]. Initially LEP had been operating with four bunches per beam. During the 1993 running period, the number of bunches could be doubled. Later LEP also operated using four bunches, each one consisting of four sub–bunches ("bunch–train mode"). The bunch systems were synchronized such that they crossed at four interaction points.

The LEP luminosities typically were of the order of from 10^{30} cm^{-2}s^{-1} up to a few times 10^{31} cm^{-2}s^{-1}. The time–integrated luminosity delivered by LEP is presented in Figure 3.2.

3.2 DELPHI Detector

DELPHI was one of the four detectors operating at LEP collider since 1989. It was designed as a general purpose detector for e$^+$e$^-$ physics with special emphasis on precise tracking and vertex determination and on particle identification.

The detector was a full 4π solid angle apparatus, with high granularity and precise vertex determination. Its length and diameter were over 10 m, and weight was 3500 tons. The DELPHI detector consisted of 19 sub–detectors and a super–conducting solenoid, providing uniform magnetic field of 1.23 T parallel to the z axis throughout the central tracking volume[3]. Outside

[2] x, y, z are defined such that electrons circulate in positive z direction (anti–clockwise), positive y is vertical (upwards) and positive x points to the center of LEP.

[3] i.e volume containing the barrel tracking detectors - the Vertex Detector (VD), the Inner Detector (ID), the Time Projection Chamber (TPC) and the Outer Detector (OD).

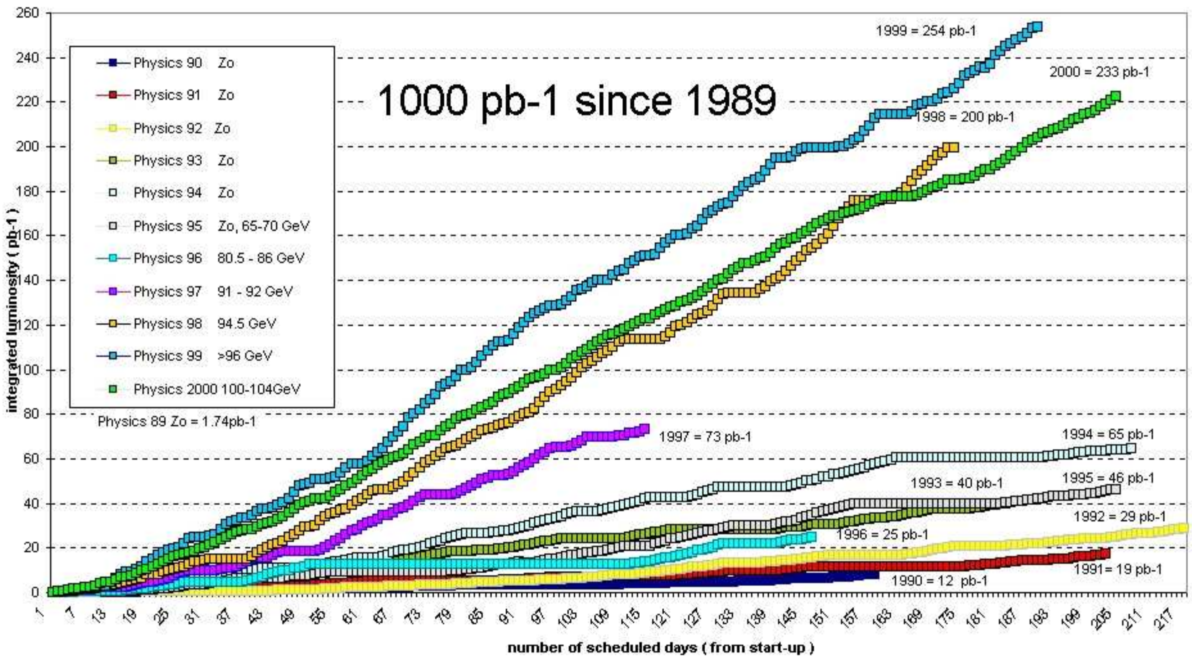

Figure 3.2: The time–integrated luminosity averaged over the four LEP experiments.

the solenoid there were hadronic calorimeter, being additionally a magnetic field return yoke and the most outer detectors – muon chambers. The detector had a layer–like structure (as it is shown in Figure 3.3), characteristic of most of contemporary high energy physics detectors. The whole detector can be divided into three geometrical sections: a barrel section, covering the region of polar angle[4] θ from 40° to 140° and two end–caps, covering the "forward" regions. The subdetectors of DELPHI are described in detail in [14] and its developments in [15].

On the basis of the role sub-detectors played in the particle reconstruction and identification, they could be divided into three main categories. Schematic view of DELPHI detector (with one end–cap) is shown in the Figure 3.3.

3.2.1 The Superconducting Solenoid

The barrel section contained a superconducting solenoid of 7.2 m length and an inner diameter of 5.2 m. The conductor, made of copper packed Nb-Ti, was operated at a temperature of 4.5°K and carried a current of 5000 A. This led to a magnetic field of 1.23 T, which allowed accurate momentum determination of charged particles from their curved trajectory. To ensure the homogeneity of the field, compensating coils were mounted on both end flanges of the main coil. The magnetic field also played an important role for those subdetectors whose design was based on charge drift in the z-direction. The drift parallel to the magnetic field strongly reduced

[4]The polar angle to the z axis is called θ and the azimuthal angle around the z axis is called ϕ; the radial coordinate is $R = \sqrt{x^2 + y^2}$.

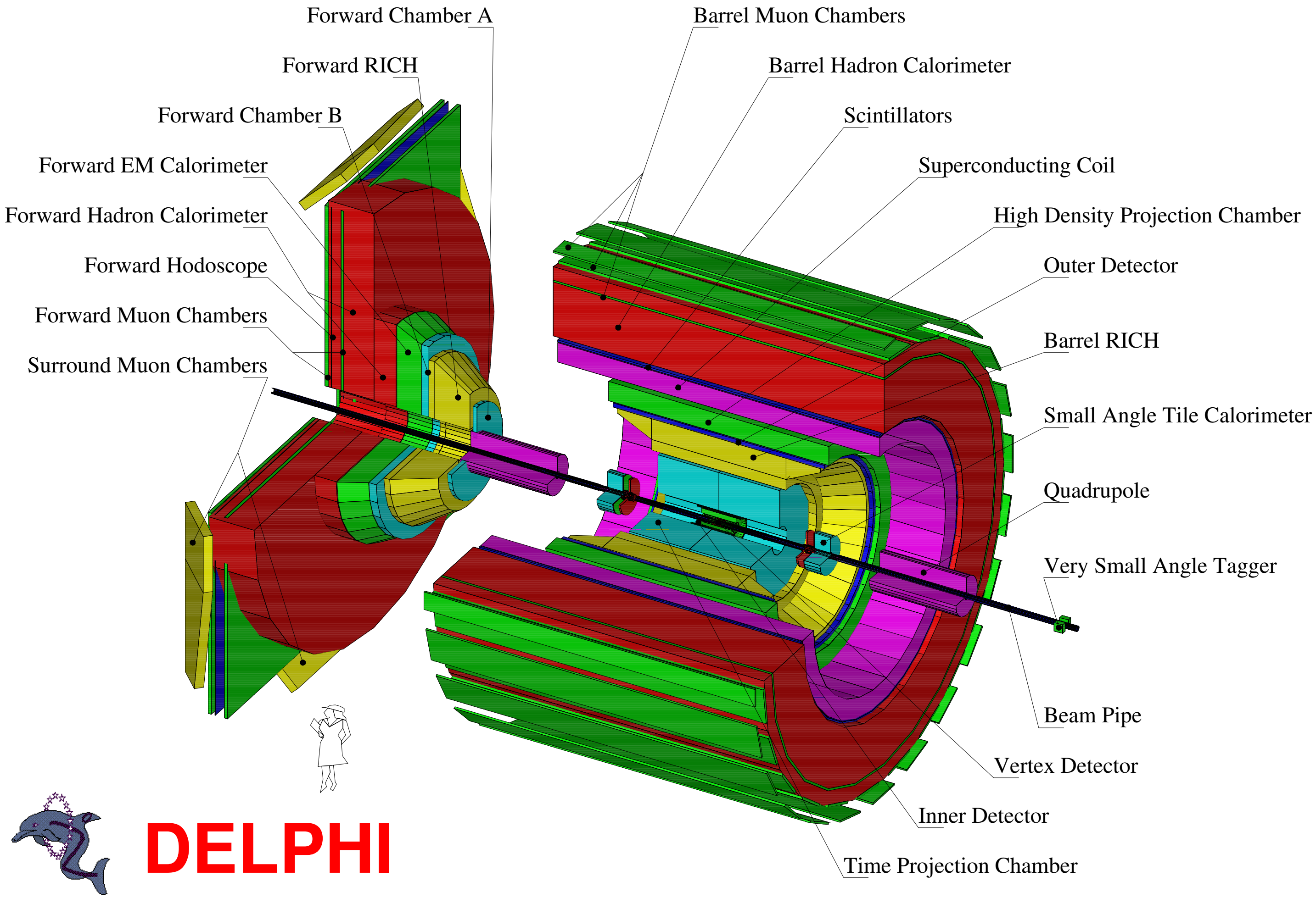

Figure 3.3: Schematic view of DELPHI detector.

transverse diffusion in Time Projection Chamber, the Barrel Ring Imaging Cherenkov counter and High density Projection Chamber (electromagnetic calorimeter). The radial component of the magnetic field was of the order of 10^{-4} of its longitudinal value.

3.2.2 Tracking Detectors

In the barrel part of the detector the following independent tracking devices were installed: the Vertex Detector (VD), the Inner Detector (ID), the Time Projection Chamber (TPC), the Outer Detector (OD) and the Barrel Muon Chambers (MUB). In the forward part there were: the Forward Chambers A and B (FCA and FCB) and the Very Forward Tracker (VFT). The tracking detector purpose was precise measurement of trajectories, and the precise determination of the directions and momenta of the charged particles.

Time Projection Chamber

The **T**ime **P**rojection **C**hamber (TPC) was the main tracking device of DELPHI detector. It provided also the charged particle identification trough the dE/dX measurement and contributed to the trigger decision[5] at the second and third level.

The TPC detector was in the magnetic field of DELPHI superconducting solenoid. It consisted of two cylinders of length of 134 cm each, with the active radial range between 29 cm and 122 cm, which were separated by a high voltage (20 kVolts) electrode, producing uniform electric field of 150 V/cm. A charged particle, when crossing the TPC, produced by ionization about 70 electrons/cm of gas (80% Ar, 20% CH_4). Under the action of the electric field these primary electrons drifted in the direction of the multi-wire proportional chambers (divided into 6 sections at each TPC end-plates). Every TPC sector had 16 rows of pads, what gives 16 space points per track. In each sectors there were 1680 pads. In front of the pads plates there were 3 levels of grid. The first one, called gate grid was used to collect the positive ions produced in the showers at the level of the sense wires. To close the electric lines for the ions, a small alternate potential ($\pm$30 V) was applied on 2 consecutive wires of this grid. The primary electrons, with larger drift velocity (6 cm/μs) than the ions (0.3 cm/ms), were not affected by this grid. The second, cathode grid was used to limit the electric field of the proportional chamber. The last one, which was the closest to the pad (the anode grid, at a HV of 1430 V) contained 192 active sense wires per sector, separated by 4 mm, performing the dE/dX measurement.

The detector provided points per particle trajectory at radii from 40 to 110 cm, where its polar acceptance covered angles from 39 to 141 degrees. At least three space points per track were given for $20^\circ \leq \theta \leq 160^\circ$.

The average tracking spatial resolution $\sigma_{R\phi}$ ranged from 180 to 280 μm (depending on the ϕ and z), and the average z resolution was 0.9 mm. The average resolution on ionization loss dE/dX measurement was about 6.5%$\cdot(dE/dx)$ for hadronic events.

[5] General description of the trigger system at DELPHI is given in Section 3.2.6.

The three coordinates were reconstructed as follows: x and y were given by the single pad hits distributions at the end of the drift volume on the collector plane and z was reconstructed by the charge drift time.

Vertex Detector and the Very Forward Tracker

The **V**ertex **D**etector (VD) was positioned closest to the interaction point. It was an advanced silicon detector providing very precise tracking, mainly in order to detect very short lived particles by extrapolating the tracks back towards the interaction point. The points provided by the VD were essential for a precise reconstruction of the interaction point of the e^+e^- collision and for the reconstruction of B meson decay vertices. The presence of the VD hits reduced the error on the secondary vertex reconstruction and in the tracks impact parameters.

The detector had been modified several times. In the latest version it consisted of three coaxial cylindrical layers of silicon strip detectors. Their average radii were 6.3, 9.0 and 10.9 cm. For polar angles of $44° \leq \theta \leq 136°$, a particle crossed all three layers of the VD[6]. It had a resolution of 11 μm in $R\phi$ and 13 μm in z. The double track resolution in $R\phi$ was ≤ 100 μm.

The **V**ery **F**orward **T**racker (VFT) was located on both sides (A and C)[7] of the Vertex Detector. It was built of two layers of mini strip and two layers of pixel detectors. The VFT covered the polar angle from 10 to 25 degrees. A pixel detector crown was built from 18 or 20 modules which were arranged on a cone. Each module had about 8000 detector elements. Each layer of the mini strip detector was built from two half rings with 6 detector modules each surrounding the beam pipe. Every module was formed by two single-sided strip detectors which were assembled back to back with perpendicular strip orientation. In total there were 48 modules consisting of 96 detectors.

Inner Detector

The **I**nner **D**etector (ID) was a tracking and triggering detector. It was located between the Vertex Detector and the Time Projection Chamber and provided intermediate precision position and trigger information. It consisted of two parts: the JET chamber and the Trigger Layers (TL). The JET chamber was a drift chamber, subdivided into 24 sectors of 15° in ϕ. Each sector consisted of 24 sense wires, measuring drift time. The drift gas used was CO_2 with a small admixture of Isobutane (iC_4H_{10}, 4.7%).

The polar angle coverage of the detector was $15° \leq \theta \leq 165°$. The JET chamber measured up to 24 Rϕ points on a track. The single wire resolution was of the order of 90 microns and the 2-track separation was of the order of 1 mm. The Trigger Layers, filled with admixture of argon (70%) and CO_2 (30%) surrounded the JET chamber. Each of them had a Multi Wire Proportional Counter with 192 sense wires, spaced by 8 mm, stretched parallel to the beam pipe

[6] the polar angle coverage for VD is $25° \leq \theta \leq 155°$

[7] the electron and positron directions in relation to the DELPHI detector position in the cave were denoted by A and C. Positrons circulated in the A→C direction.

and circular cathode strips giving $R-z$ information. The TL measured up to 5 points in Rϕ and z. The JET chamber and the Layers combined information resolves the left/right ambiguities on the position measured in the JET chamber.

Outer Detector

The **O**uter **D**etector (OD) provided precise direction measurement after the Barrel Ring Imaging Cherenkov detector. The OD was an element of the trigger system. It consisted of five layers of 4.7 m long drift tubes located between radii of 197 and 206 cm. The active length of the detector corresponded to polar angles from 42 to 138 degrees. Each layer provided three-dimensional information. The resolution in Rϕ was 110 μm. The z information was obtained from the measurement of the arrival time of the signal at both ends, with a resolution of 3.5 cm.

The OD provided fast trigger information in both Rϕ and z direction. Since it was positioned $\sim$2 m away from the interaction point, the OD points increased the lever-arm for the track reconstruction and thus enabled a precise determination of the momentum of a charged particle.

Dedicated electronics was used to produce the local trigger results for the first and second level. ID trigger data were correlated with the OD ones in order to reduce the rate due to cosmic and beam gas events. The IDOD trigger was very useful to cover the gaps between the TPC sectors.

Forward Chambers

The **F**orward **C**hamber **A** (FCA) and **F**orward **C**hamber **B** (FCB) were end-cap detectors. The sensitive area of the chambers corresponded to polar angles from 11 to 36 degrees and from 144 to 169 degrees.

The FCA distance from the interaction point was about 160 cm in z. It was positioned next to the endcaps of the TPC and the FCB between the RICH and electromagnetic calorimeter. On each side the FCA consisted of three double layers of drift chambers which were operated in limited streamer mode. To obtain optimal reconstruction of space points and a good resolution, the 3 layers were rotated by 120° with respect to each other. In normal conditions, the precision on the reconstructed track elements were 290μm (x), 240 μm (y) 8.5 mrad (θ) and 24 mrad (ϕ, averaged over θ). The chamber covered polar angles from 11 to 32 degrees and from 148 to 169 degrees.

The FCB was a conventional drift chamber consisting of 4 independent modules, 2 at each end-cap, at a distance of 275 cm in |z| from the interaction point. Each module was divided into 12 sense-wire planes. Like the FCA, 3 groups of 4 planes were rotated by 120° with respect to each other. The precision obtained on the reconstructed track elements was 150μm in the (x,y) plane, 3.5 mrad in the polar angle θ and 4/sinθ mrad in the azimuthal angle ϕ.

The FCA and FCB were the main DELPHI tracking detectors in the forward region. Apart from tracking information, both chambers provided also trigger information.

3.2.3 Calorimetry

The calorimeters measured the energy and position of charged and neutral particles. They served for the detection of particles via the total attenuation of their energy. The measurement giving both particle energy and approximate position relied on the detection of nuclear and electromagnetic cascades induced by it while passing through matter. There were two main kinds of calorimeters in DELPHI spectrometer: electromagnetic calorimeters (HPC, FEMC, STIC/SAT and VSAT) and hadron ones (HCAL). Electromagnetic calorimeters served additionally as a main source of electron identification. The STIC and VSAT were placed close to the beam pipe at large distances from the interaction point in order to measure the luminosity through elastic e^+e^- scattering at low angles.

Both kinds of calorimeters contained high density materials in which most particles were loosing all their energy, producing showers of secondary particles. The position and energy of these showers were reconstructed using active materials placed between the layers of high density materials. Only muons and neutrinos were not stopped. Muons were identified by a set of tracking chambers at the extreme outside of the detector, while neutrinos remained undetected.

High density Projection Chamber

The **H**igh density **P**rojection **C**hamber (HPC) was DELPHI electromagnetic calorimeter in the barrel region. It was situated between the OD and the super-conducting coil (inner radius = 208 cm, outer radius = 260 cm) and was arranged in a set of 6 rings along the beam pipe, each one consisting of 24 individual modules. Such a module provided a three dimensional reconstruction of electromagnetic shower. As such, the HPC was one of the largest time projecting gas calorimeters of its kind.

Each module was a small TPC with layers of dense material in the gas volume where electromagnetic showers develop. These layers were made from lead wires, which served as converter material and provided the drift field. Depending on the track angle of incidence, the lead converter thickness varied between 18 and 22 radiation lengths. The interleaved 8 mm gaps were flushed with an admixture of argon (80%) and CH_4 (20%).

The HPC was designed to reconstruct electromagnetic showers with high granularity while maintaining an adequate energy resolution.

The high granularity enabled an accurate spatial resolution of about 2 mrad in ϕ and in θ. This allowed good separation between showers from electromagnetically interacting particles and hadrons. The high granularity was also important in the identification of the π^0 particle, as it decays into two nearly parallel photons. The energy of electromagnetic particles was measured with resolution of $\sigma(E)/E=(32/\sqrt{E}+4.3)\%$ (E in GeV).

Forward Electromagnetic Calorimeter

The **F**orward **E**lectro**M**agnetic **C**alorimeter (FEMC) was situated in both endcaps of DELPHI detector. It consisted of two 5 m diameter disks (made of Cherenkov lead-glass blocks). The front faces were placed at $|z| = 284$ cm, covering the polar angles from 8 to 35 and 145 to 172 degrees. Each block was mounted in the detector to point near to the interaction region. A tilt of about 1° was applied in order to avoid any particle escaping undetected in the insensitive regions between the blocks.

The operation of lead-glass Cherenkov counters was based on the collection of Cherenkov light emitted by the charged tracks of a shower. For the readout in the magnetic field phototriodes were used. The relative precision on the measured energy was parametrized as :

$$\sigma(E)/E = 0.03 + (0.12/\sqrt{E}) + (0.11/E)$$

where E is in GeV. For neutral showers of energy larger than 2 GeV, the average precision on the reconstructed hit position in x and y projected to $|z| = 284$ cm was about 0.5 cm. the FEMC contributed to the trigger decision at all levels.

Hermeticity detectors

In order to cover the holes in the electromagnetic calorimetry and provide full hermeticity of the detector, various lead-scintillator sandwich counters and so called ϕ Taggers were placed directly after the ϕ cracks between the HPC modules.

Electromagnetic calorimeters STIC and VSAT

The **S**mall angle **TI**le **C**alorimeter (STIC) was a sampling lead-scintillator calorimeter formed by two cylindrical detectors placed on either side of DELPHI interaction region at a distance of 220 cm. It covered an angular region between 29 and 185 mrad in polar angle (from 6.5 to 42 cm in radius). Its aim was to measure energy of electrons and photons produced at small angles with respect to the beam axis. The cylinders had projective geometry and a tower structure defined by 47 scintillator tiles. The light produced in the scintillator was read by wavelength shifting optical fibres, placed perpendicularly to the scintillator layers. The energy resolution at 45 GeV is 3%. The spatial resolution of the calorimeter alone was 1.5 degrees in ϕ) and from 300 μm to 1 mm in radius. The resolution of the silicon strips (1.7 mm pitch) over the measure of radial coordinate is 400μm. The expected systematic error in luminosity measurement was 0.2%.

The **V**ery **S**mall **A**ngle **T**agger (VSAT) consisted of 4 calorimeter modules. Such a module was composed of 12 silicon diodes. It detected electrons and positrons coming from Bhabha scattering between 5 and 7 mrad.

Three silicon strip planes, 5×5 cm^2 in size with 1 mm pitch and placed at 5,7 and 9 radiation lengths into the modules were used for the (x, y) shower position measurement. There were two planes for the X measurement with 32 strips and one for the y-measurement with 48 strips. Full depletion and operation voltages were equal to +25 V for both types of strip planes.

A lead block with 10 radiation lengths thickness was placed on back side of each module in order to decrease the number of parasite (not coming from interaction point) events like photon's or off-momentum lepton's hits from the back.

Hadron Calorimeter

The hadron calorimeter was a sampling gas detector incorporated in the magnet yoke, with the barrel part covering polar angles between 42.6 and 137.4 degrees, and two end-caps between polar angles of 11.2–48.5 and 131.5–168.8 degrees.

The barrel was constructed of 24 modules with 20 layers of limited streamer mode detectors. They were inserted into 2 cm slots between 5 cm iron plates in each module. The modularity of end-caps was similar to the barrel with a sampling depth of 19 layers. The detectors were wire chambers which consisted of a plastic cathode forming 8 cells of 0.9×0.9cm with one anode wire (80μm made of copper-beryllium) in each. The inner surface of the cathode cells was coated with graphite varnish.

The hadron calorimeter contained by far the largest volume of gas in DELPHI, and operated with relatively low Isobutane content: Ar/CO_2/Isobutane (10/60/30 %). With this gas mixture an average charge of 10 pC was induced on external readout boards with an HV of 4 kV. The energy resolution was

$$\sigma(E)/E = (112/\sqrt{E} + 21)\% \text{ (E in GeV)}.$$

HCAL contributed to the trigger decision with signals corresponding to three energy thresholds: 0.5, 2 and about 5 GeV.

3.2.4 Particle identification

The identification of charged particles in DELPHI relied on the specific ionization energy loss per unit length (dE/dX) in the TPC and emission of the Cherenkov radiation. Neutral hadrons and photons could be identified via the total attenuation of their energy in the calorimeters.

TPC and VD

Both detectors are described in the part concerning tracking detectors. They were used for the track reconstruction (TPC and VD) and for particle identification through the measurement of ionization energy loss, dE/dX (TPC).

Ring Imaging Cherenkov Detectors

The charged hadron identification in DELPHI was based on using the **R**ing **I**maging **CH**erenkov (RICH) technique. It was based on the measurement of the emitted Cherenkov radiation from ultra relativistic particles. The RICH system in DELPHI comprised of the Barrel RICH (BRICH) in the central region and two endcap detectors, which formed the Forward RICH (FRICH). It might be worth mentioning that DELPHI was the first experiment that used RICH detectors on the large scale.

Charged particles moving through a transparent dielectric medium with a velocity v larger than the phase velocity of light in that medium (i.e. c/n, where n is the refractive index of the medium) emit radiation at a specific angle with respect to the direction of flight. The angle between the propagation direction of the particle and the emitted radiation, the so-called Cherenkov angle, θ_C, is given by:

$$\cos\theta_C = \frac{1}{\beta n} = \frac{\sqrt{1+m^2/P^2}}{n},$$

where m and P are the mass and momentum of the particle and $\beta = v/n$. Therefore, the velocity of a particle can be determined by measuring the Cherenkov angle. Since the momentum is known from the tracking detectors, the mass can be determined and the particle is, consequently, identified. For a given refractive index, with the increase of a particle's momentum the Cherenkov angle achieves a certain value, which is independent on the particle's mass. Below the threshold velocity, $\beta_{th} = 1/n$, no photons are emitted. The principle of DELPHI RICHes operation is illustrated in Figure 3.4.

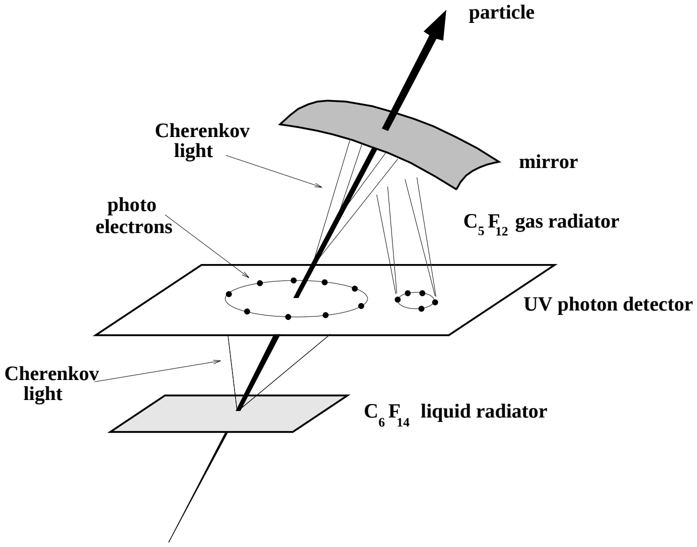

Figure 3.4: The principle of DELPHI RICH detector operation.

The DELPHI RICH contained two radiators of different refractive indices. The liquid radiator (C_6F_{14}) was used for particle identification in the momentum range from 0.7 to 8 GeV/c. The gas radiator (C_4F_{10} in the forward part and C_5F_{12} in the barrel) was used for 2.5 to 25 GeV/c. It was kept at a temperature of 40°C and a pressure of 1033 mbar.

Barrel RICH covered polar angles between 40 and 140 degrees and FRICH covered the angles $15° < \theta < 35°$ and $145° < \theta < 165°$.

Photons were focused onto photosensitive time projection chambers, 48 in the BRICH and 24 in each of FRICHes. The three coordinates of the photon conversion point were determined by detecting the generated electron, referred to as the photoelectron. The Cherenkov angle was then reconstructed. An uncertainty of the angle value was also computed, which depended on photon conversion point and on the quality of the tracking information.

The identification power of the RICH depended on the accuracy of the Cherenkov angle measurement and on the number of the photoelectrons detected. The angular precision per photoelectron varied from 2.5 mrad in forward gas RICH to 13.3 mrad in the barrel liquid. Angular precision per track varied from 1.2 mrad to 5.2. The given numbers were obtained for $e^+e^- \to Z \to \mu^+\mu^-$ events.

Muon Chambers

The **M**uon **C**hambers (**M**uon **B**arrel **C**hambers - MUB, **M**uon **F**orward **C**hambers - MUF and **S**urrounding **M**uon **C**hambers - SMC) were farthest from the collision point, since muons are the only charged particles that can traverse the lead and iron of both calorimeters essentially unaffected. Most muons of momenta above 2 GeV/c were expected to penetrate the Muon Chambers, whereas other charged particles were stopped by this material. Muon identification was achieved by comparing the extrapolations of the reconstructed tracks with the hits in the Barrel (MUB that covered polar angles from 53.0 to 88.5 degrees and from 91.5 to 127.0 degrees) and Forward (MUF that covered polar angles from 20 to 42 degrees and from 138 to 160 degrees) muon drift chambers. In 1994 a layer of Surrounding Muon Chambers (SMC) based on limited streamer tubes was installed outside the endcaps to close the gap between the barrel and forward regions.

Each layer of the barrel muon chamber contained two staggered planes of drift tubes, which had a maximum drift distance of 10 cm to the central anode wire. The z coordinate was measured through a delay line, by comparing the time difference at both ends. The first layer was situated inside the return yoke after about 90 cm of iron, at 20 cm from the outer edge. The second layer was mounted on the outside of the iron. The third layer was positioned at 50 cm outside the return yoke and covers the regions that were left out by the first two layers, with a large overlap. The barrel muon chambers covered a polar region from 53° to 127°. Their resolution was approximately 3 mm in $r\phi$ and 2.5 cm in z.

The forward muon detector consisted of two detection planes in each of the two end-caps of DELPHI. Each plane was made of 4 modules called quadrants, with dimensions 450 cm×450 cm×8 cm. Each quadrant contained two layers of 22 drift chambers crossed at 90 degrees. The basic detector cell was a 20 cm wide drift chamber equipped with a single anode wire and parallel delay line, used to determine the orthogonal coordinate. Each drift chamber provided 3 measurements: the drift time and the propagation times of the induced anode pulse to both ends of the delay line. Because of the small number of charged particles crossing our detector, it was impossible to monitor the behaviour of each chamber individually. The monitoring was thus done at the layer level and the detector counted a total of 32 layers.

The accuracy on the x and y coordinates was of the order of 5 mm, depending on whether these coordinates were reconstructed in the drift direction or along the delay lines.

Scintillator counters

In DELPHI detector there were two systems of scintillator counters, **T**ime **O**f **F**light counters and **F**orward **HO**doscope scintillator.

HOF was designated to produce fast and practically stand-alone trigger on muon event in endcap regions (and single halo muon). The first level HOF's Forward and Backward triggers were used by corresponding Muon Chambers. The detector also gave the information on the hit space position and timing which was used for some other detectors calibration. Due to its fast response (less than 50 ns) HOF was able to determine in what bunch in a train did the event happen. The scintillators were located behind the Forward Hadron Calorimeter.

The Time Of Flight detector consisted of a single layer of 192 scintillation counters along the beam axis. They were situated between the Hadron Calorimeter and the solenoid. The TOF counters provided fast trigger information that allows to distinguish the beam–beam interaction from a cosmic ray event.

3.2.5 Luminosity measurement

In e^+e^- colliders luminosity is measured by counting the number of events of a process with a clear experimental signature, with high statistics and with a cross section which can be calculated theoretically with high precision. The chosen process is Bhabha scattering at small angles, which proceeds almost entirely through the exchange of a photon in the t-channel. In DELPHI the absolute luminosity was measured using the Small angle TIle Calorimeter (STIC) and the Very Small Angle Tagger (VSAT). A precise luminosity measurement was essential for the electroweak precision measurements, and up to now the precision of 0.09% [16] has been achieved.

3.2.6 Trigger

The aim of the trigger system was to select interesting physics events with the highest possible efficiency, keeping the background events rate at a reasonable level[8]. In order to cope with high luminosities and large background rates DELPHI trigger scheme consisted of four successive levels (T1, T2, T3 and T4), reducing the beam crossing rate of 45 (in the four bunch mode) or 90 (in the eight bunch mode) kHz, to a data recording rate of a few Hz. The first two trigger levels (T1 and T2) were combinations of trigger signals from the subdetectors and were synchronous with respect to the Beam Cross Over signal (BCO). That means the decisions

[8] Please note that in the low cross section interactions (like at LEP) the main goal of the trigger system is to collect as many collisions of the primary particles as only possible. This is in contrast with the high cross section interaction (like at LHC) where the trigger system has to be as selective as possible. Of course, in both cases the trigger system has to filter out the events not coming from the primary particle collisions (like beam-gas interactions, electronic noise, etc.

of T1 and T2 were taken after a fixed period of time (3.5μs for T1 and 39μs for T2) after the bunch crossing. The last two levels (T3 and T4) were software filters and were performed asynchronously with respect to the BCO. The T3 and T4 decisions are taken approximately 20 ms and 500 ms after the BCO. The fourth trigger level was capable of fully reconstructing the event. It rejected about a half of the background events remaining after T3.

Each subdetector contributed to the trigger decision with data generated by the respective subtrigger processors. The overlapping geometrical acceptance of the different detectors provided substantial redundancy between the different trigger conditions. This feature of DELPHI trigger ensured high and stable efficiency over long running periods.

The redundancy between the different trigger components also made it possible to determine both the trigger efficiency and its maximal error with good precision. The global trigger efficiency for electron and muon pairs was consistent with 1 at the level of 0.0001 for polar angles between 20 and 160 degrees. Even for single tracks, provided their momentum transverse to the beam exceeded 1 GeV/c, the efficiencies in the barrel (between 42 and 138) and forward (between 10 and 32) and backward 148 and 170) regions exceeded 95%.

The selection criteria were implemented in tables read by the trigger processors. They were made out of several combinations of signals from the different subdetectors.

The data acquisition system (DAS) of DELPHI was responsible for the full chain of data taking, from the subdetectors to the storage on disk or magnetic tape. It had 17 partitions, each corresponding to a subdetector or a part of a subdetector.

Most of the elements of DELPHI provided information directly in 3 dimensional form, which was read out via about 200,000 electronic channels by 72 dedicated microprocessors. The data were then merged to form an event and shipped to a central set of computers where they were logged onto mass storage for subsequent analysis. A typical event contained 1MB of information.

Design and construction of DELPHI detector had taken 7 years. Data had been taken every year typically throughout the spring, summer and autumn. During the data-taking periods, LEP and the detectors were operated 24 hours a day. Winter was reserved for a long shutdown, used for maintenance and modifications (including upgrading of LEP as well as of the detectors).

The DELPHI detector is the only one of the four that remained in its cave as an exhibition object. It was moved from its working position to give place to the new experiment (LHCb at LHC accelerator) now under construction.

3.2.7 Event reconstruction and simulation

The raw data stored by the DAS were treated by a dedicated event reconstruction program DELANA, described in [17]. It gave as an output a reduced amount of data. At the output level, the information from the different subdetectors was associated, defining the final state particles with kinematic characteristics to be used in the analysis codes. DELANA is divided into parts that were executed in the following sequence:

- reconstruction of the information in every subdetector,

- tracks search, fit and extrapolation of a particle trajectory,
- combination of the information from the calorimeters,
- global reconstruction,
- particle identification,
- vertex reconstruction.

The DELANA code uses a data structure of several levels, TANAGRA (Track ANAlysis and GRAphics) [18] to store the information of the various reconstruction steps.

Very important for any physics analysis is the possibility of comparing the selected data with an equivalent sample of simulated data. After a sample of events has been generated for the interesting physics process, or processes, the detector effects must be included. The code performing the simulation of DELPHI detector is DELSIM (DELphi SIMulation program) [19].

The information about the specific conditions of the detector at a given moment (e.g. calibration constants, specific information modes for some of the subdetectors) needed for the simulation and reconstruction programs are kept in a data base.

Chapter 4

Light Higgs bosons production processes

In this chapter Higgs bosons production processes, available at LEP are described. A description of the Yukawa process is given here, as a new possibility for search for a light h^0 or A^0 Higgs boson within 2HDM(II).

4.1 Higgs bosons production processes at LEP

In the LEP collider there are two main processes that 2HDM Higgs bosons may be produced in:

- **the Bjorken process:** $e^+e^- \longrightarrow Z^{(\star)} \longrightarrow Z^{(\star)}h^0$. In this process the Higgs boson h^0 is radiated off the Z^0 or $Z^{0\star}$ boson (see Figure 4.1). $Z^\star$ is a virtual (off mass shell) Z^0 boson, i.e. its mass is lower (in the case shown in Figure 4.1a) or higher (in the case shown in Figure 4.1b) than the mass of the real Z^0. The process is analogous to the *Bremsstrahlung* and often called *Higgsstrahlung*. It is possible in both the 1HDM and 2HDM models.

  As it is a tree-level process, only H^0 or h^0 bosons may be produced (see chapter 2), if kinematically allowed. The Bjorken process may occur in the following ways:

  - $e^+e^- \longrightarrow Z^0 \longrightarrow Z^{0\star}h^0$. The process is available for LEP1 energies (at the Z^0 peak – Figure 4.1a.)
  - $e^+e^- \longrightarrow Z^{0\star} \longrightarrow Z^0h^0$. This process is being searched for at LEP2 energies ($E_{cms} > Z^0$). See Figure 4.1b.

  The coupling $Z^0Z^0h^0$ for this process in the 2HDM is suppressed by the factor $\sin(\beta-\alpha)$ with relation to the process in the 1HDM, as given in (2.67). The cross section suppression factor for 2HDM Bjorken process is then proportional to $\sin^2(\beta-\alpha)$ in relation to similar process in the Standard Model:

$$\sigma(e^+e^- \to Z \to hZ^\star) = \sigma_{SM}(e^+e^- \to Z \to H_{SM}Z^\star) \times sin^2(\beta-\alpha)$$

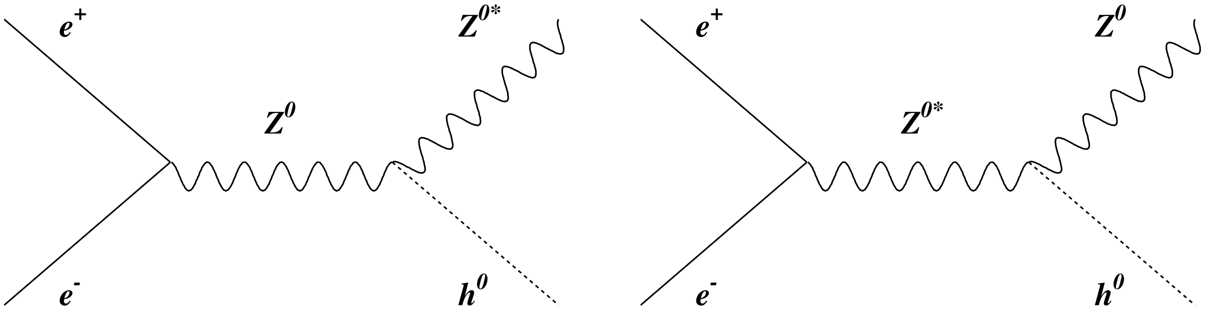

Figure 4.1: The Bjorken (*higgsstrahlung*) process. The left diagram illustrates the process available at LEP1 energies and the right diagram – the LEP2-available process.

- **pair production process:** $e^+e^- \longrightarrow A^0h^0$. The process is not possible in the 1HDM. In the 2HDM at the tree-level also A^0H^0 and H^+H^- pair production is possible. The Feynman diagram for the pair production is shown in Figure4.2. The process is complementary to the *higgsstrahlung*, i.e. the cross section in the 2HDM in relation to a similar 1HDM process is proportional to $\cos^2(\beta - \alpha)$:

$$\sigma(e^+e^- \to Z \to hA) = \sigma_{SM}(e^+e^- \to Z \to \nu\bar{\nu}) \times cos^2(\beta - \alpha)\lambda^{\frac{3}{2}}$$

where $\lambda = (1 - \kappa_h - \kappa_A)^2 - 4\kappa_h^2\kappa_A^2$ is a phase space factor, with $\kappa_i = m_i^2/m_Z$ [8]

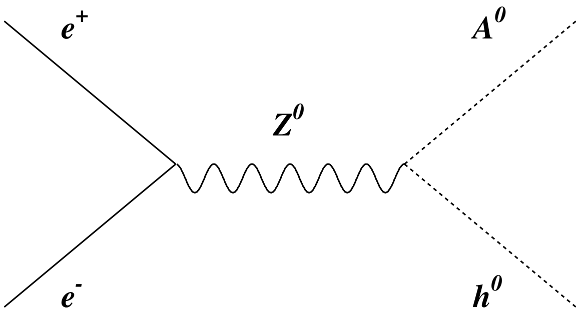

Figure 4.2: The pair production Feynman diagram.

4.2 Possible existence of one light neutral Higgs boson

As it was said in the previous section, 2HDM h^0 coupling to Z^0 boson is suppressed by a factor $\sin(\beta - \alpha)$ (equation 2.67) in comparison to the 1HDM Higgs boson, what makes the respective cross section in the Bjorken process suppressed by the factor $\sin^2(\beta-\alpha)$. The fact of non-observation of the Bjorken process (as presented in publications of LEP experiments [20, 21, 22, 23]) allows to derive a mass limit for the SM Higgs boson. At the same time any negative search provides a limit on the appropriate cross-section. In the Standard Model the Higgs production cross-section at LEP depends on its mass and available energy. Within 2HDM model one gets also constraints on the $\sin(\beta-\alpha)$. From recent experimental results, presented in an article by M. Krawczyk *et.al* [24] one can deduce that if $\sin^2(\beta-\alpha)$ is small, then the h^0 boson of arbitrary low mass cannot be seen in the Bjorken process in the LEP data, what means that the existence of such a boson cannot be excluded. Analyses, performed by L3 [23] and OPAL [22] put 95% C.L. limits on $\sin^2(\beta-\alpha)$ from the Higgs boson search at LEP as functions of M_{h^0} (Figure 4.3).

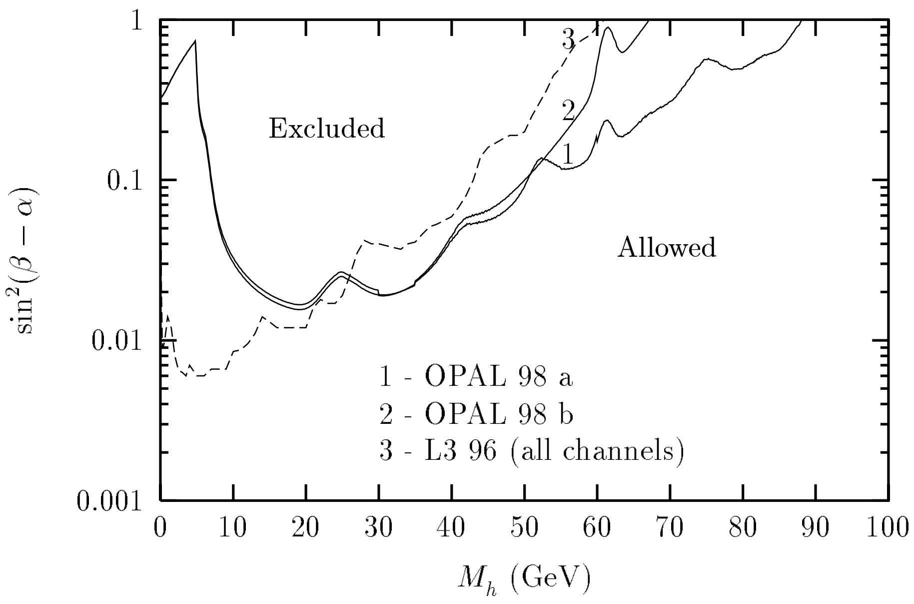

Figure 4.3: 95% C.L. limits on $\sin^2(\beta-\alpha)$ from the Higgs boson search at LEP as a function of M_{h^0}. Lines 1 and 2 are the OPAL results. Line 3 is L3 result.

In the A^0h^0 pair production mechanism the ZAh coupling is proportional to $\cos(\beta-\alpha)$, and the cross-section to $\cos^2(\beta-\alpha)$. When $\sin^2(\beta-\alpha)$ is close to zero, the pair production recovers its full strength. To explain the non-observation of the process it is enough to assume that the mass of one of the Higgs bosons is large enough, to make the process kinematically forbidden. In the case of 2HDM the masses of A^0 and h^0 are not related [8]. Thus the model provides two scenarios with a light Higgs boson:

- The h^0 is light and the A^0 is heavy. In that case the Zh coupling must be small (which is equivalent to $\sin^2(\beta-\alpha)\sim 0$ within 2HDM

- The A^0 is light and the h^0 is heavy.

In both scenarios the light neutral Higgs boson cannot be observed via the pair production or Bjorken process at LEP. However, in the 2HDM there are additional degrees of freedom in the Higgs sector and Higgs–fermion Yukawa couplings can be altered. Within 2HDM(II) the ratio of Yukawa coupling, comparing to the corresponding SM coupling is given by:

- $\sin\alpha/\cos\beta$ for the down-type quarks and leptons and $\cos\alpha/\sin\beta$ for the up-type quarks in the case of h^0;

- $\sin\beta/\cos\beta = \tan\beta$ for the down-type quarks and leptons and $\mathrm{ctan}\beta$ for the up-type quarks in the case of A^0;

There are at least two possibilities to be considered: $\tan\beta \gg 1$ or $\tan\beta \ll 1$. From the experimental point of view the latter case is already excluded by a search for $Z \to h(A)\gamma$ process [25]. Taking this into account we will restrict our considerations to the possibility that the coupling to the down-type fermions is enhanced. It opens a possibility for a search of the Higgs boson via the third production mechanism at LEP1, the so called Yukawa process.

4.3 Yukawa process

In the Yukawa process h^0 or A^0 Higgs boson is radiated off a fermion f or antifermion $\bar{f}$, coming from decay of the Z (see Figure 4.4):

$$e^+e^- \to Z^0 \to f\bar{f}h^0,\ h^0 \to f\bar{f}, \qquad e^+e^- \to Z^0 \to f\bar{f}A^0,\ A^0 \to f\bar{f} \tag{4.1}$$

The process should, in fact, be treated as an effective three-body process; the diagrams (containing Higgs boson radiation off a fermion and anti-fermion) interfere. In the process one of the fermions, coming from the Z^0 decay is virtual and returns to the on-shell mass state by radiating off the Higgs boson.

The Yukawa process is available either in 1HDM and 2HDM. In both models the cross-section for the Yukawa process is supressed by a factor $(m_f/m_W)^2$ in comparison to the Bjorken process. Thus, in the 1HDM model, the cross-section is too small to observe the Yukawa process can at LEP energies. As was said above, the Higgs boson–fermion couplings can be altered in 2HDM for large values of $\tan\beta$. The cross section for the Yukawa process is then enhanced if A^0 is radiated off down-type quark and charged lepton. The h^0 boson couplings to fermions depend also on the α parameter. However, small value of $\sin^2(\beta-\alpha)$, necessary for existence of a light h^0 boson within 2HDM, indicates the relation of $\alpha \simeq \beta$. Therefore the h^0 couplings to

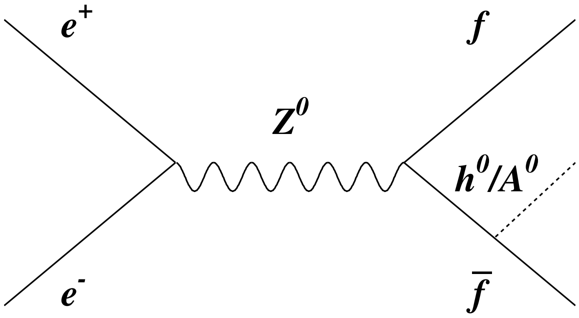

Figure 4.4: The Yukawa process

down-type fermions can be described with good approximation by tanβ factor (and ctanβ for up-type fermions, respectively).

Even for large values[1] of tanβ, from the experimental point of view, only considering the heaviest available fermions ($\mathbf{b\bar{b}}$ and $\tau^+\tau-$ pairs) makes sense. In this case one can distinguish three mass intervals for the light Higgs boson masses as far as final topologies are considered:

- $m_{A/h} < 2m_\tau$

  For this interval the Higgs boson A^0 or h^0 decays into light leptons (e or μ) or light quarks. Then in the final state there are $\tau^+\tau^-$ or $b\bar{b}$ pairs (coming from the Z boson decay) accompanied by a narrow, low multiplicity jet of e or μ leptons, or light hadrons.

- $2m_\tau < m_{A/h} < 2m_b$

  The dominant decay channel for Higgs bosons for this interval are $\tau^+\tau^-$ pairs, for they are the heaviest available down-type fermions. This gives $b\bar{b}\tau^+\tau^-$ and $\tau^+\tau^-\tau^+\tau^-$ final states[2].

- $m_{A/h} > 2m_b$

  Above 2m$_b$ threshold Higgs bosons decay mostly to $b\bar{b}$ pairs, what gives $b\bar{b}b\bar{b}$ and $\tau^+\tau^-b\bar{b}$ final states. In this mass region also decay $A^0/h^0 \to \tau^+\tau^-$ occurs, but the branching ratio for this process is too small in comparison to $A^0/h^0 \to b\bar{b}$ decay to consider the channel to be effective for the A^0/h^0 search.

For the first mass interval the relevant Monte Carlo generator was not available to the author. Because of small Higgs boson mass, non-perturbative effects should be included in the calculation of the Higgs branching ratios. Such effects are also important for the threshold behaviour on top

[1]In the presented analysis the value of tanβ was set to 30, see Chapter 5

[2]In such a notation the first fermion pair is coming from the Z^0 decay, and the second one from A^0 or h^0 decay

of the different $\beta^{1/2}$ and $\beta^{3/2}$ kinematic factors[3] for CP-odd and CP-even scalars, respectively. We will restrict our consideration then to the Higgs boson masses above $2m_\tau$ threshold.

Searches for a very light A^0 and h^0 Higgs bosons ($m_{A/h} < 4$ GeV/c^2) in the 2HDM have been performed in other experiments. First results for the Yukawa process have been given in ALEPH experiment [26]. The limits on the (m_{A^0}, tanβ) plane, coming from non-observation of the Yukawa process are shown in Figure 4.5.

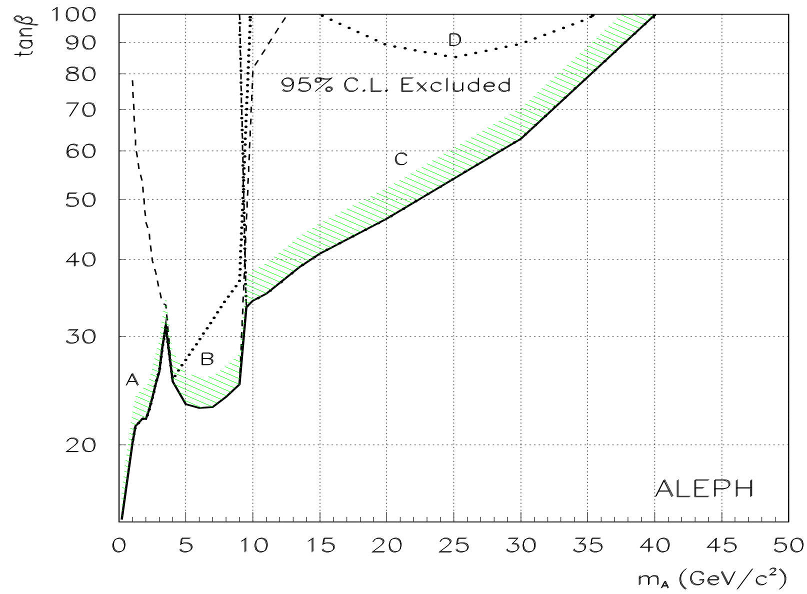

Figure 4.5: 95% C.L. excluded region in the (m_A, tanβ) plane for four (A, B, C, D) combined analyses performed by the ALEPH collaboration. The 95% C.L. excluded region is above the hatched full curve.

The Yukawa couplings to down-type quarks and charged leptons of a very light scalar or a pseudoscalar Higgs boson, with mass below 10 GeV/c^2, are constrained in form of upper limits by the low energy data [27] for processes: $Z^0 \to Z^{0\star}h^0$, $\eta' \to \eta h^0$, $\eta \to \pi^0 h^0$, $\pi \to e\nu h^0$, with Higgs bosons decaying to e^+e^- and $\gamma\gamma$. Also the analysis of the decay $Z \to h/A\gamma$ at LEP [25, 24] gave upper and lower limits for tanβ.

In the 2HDM model, $(g-2)_\mu$, muon anomalous magnetic moment, can receive radiative corrections at the one loop level from couplings of A^0 and h^0 to muons in triangle diagrams [28](and the references therein). The size of the radiative corrections is proportional to the coupling of μ to the Higgs bosons. This implies a very stringent bound on tanβ, because the coupling of muon to A^0 is directly proportional to tanβ. In a review article [28] and its update [29] a discussion concerning a very light A^0 Higgs boson, one- and two-loop graph contributions to the muon magnetic moment $(g-2)_\mu$ are presented (as shown in Figure 4.6), giving constraints

[3]Kinematic factor $\beta \equiv v/c$ should not be mixed up with vacuum expectation values ratio tan$\beta \equiv v_2/v_1$.

on the (m_{A^0}, tanβ) plane based on calculations described in published articles denoted by CLY [30], AY [31], J [32] and DH [33].

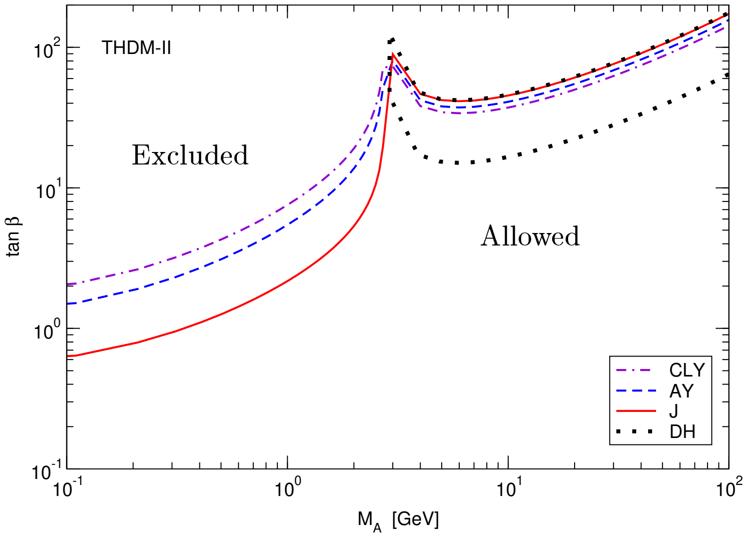

Figure 4.6: The regions in the tanβ versus M_A plane of the 2HDM(II) model, allowed by the $(g-2)_\mu$ data. The allowed region is below the curves. The curves are results of calculations presented in publications described in the text.

The relevant branching fractions in the Yukawa process for masses above $2m_\tau$ threshold are presented in Figure 4.7. The cross-sections are plotted in Figure 4.8. One can distinguish four distinct final topologies at LEP1, schematically drawn in Figure 4.9.

The topology with four b quarks in the final state provides the highest reach in the Higgs mass. For $m_{A/h} > 2m_b$ this final state is dominant over $b\bar{b}\tau^+\tau^-$ in the entire kinematically available interval. In the final state there are three or four jets, depending on A^0/h^0 mass – the lighter the Higgs boson is, the more likely it creates a single jet (the three-jet system is shown in Figure 4.9a.) In the previous LEP analyses of the Yukawa Higgs production [34, 26] this channel was considered to be overwhelmed by the QCD background and in consequence not used. In the next analysis [35] gluon splitting into $b\bar{b}$ pair in $Z^0 \to b\bar{b}$ decays was used to set a limit on the $b\bar{b}h(A) \to b\bar{b}$ contribution. The latest analysis [36] presented a search dedicated to Yukawa $4b$ production and was used also for an A^0h^0 pair production search.

The topologies $b\bar{b}\tau^+\tau^-$ and $\tau^+\tau^-b\bar{b}$ are almost identical, but in the latter one – where the Higgs boson, produced with $\tau^+\tau^-$ pair, decays into a pair of b quarks – the separation of τ decay products from the hadronic jets is in average better than in the former case. As it is less affected by the $Z^0 \to q\bar{q}g(g)$, it suffers from a very low cross section (see Figure 4.8). The former process, on the other hand, has a high background. One must require stringent isolation criteria for τ decay products or restrain to the purely leptonic τ decay channels. In this thesis the analysis dedicated only to the first topology is presented. The topologies $b\bar{b}\tau^+\tau^-$ and $\tau^+\tau^-b\bar{b}$ are schematically shown in Figure 4.9b and 4.9c, respectively.

Finally the 4τ topology is relatively simple from the experimental point of view, but it suffers from intrinsic 4-lepton background, small cross-section and small branching ratio above the $2\mathrm{m}_b$ threshold within 2HDM(II). However one should remember that models where one Higgs doublet couples exclusively to charged leptons, are not excluded providing room for a light Higgs boson with vanishing coupling to the Z^0 boson and enhanced couplings to leptons. The 4τ topology is presented in Figure 4.9d.

The cross-sections for Yukawa process in data collected above Z^0 peak (LEP2 phase) are too small to extract the signal from relatively large background. For example, at Z^0 energies, with 46.89 pb^{-1} data collected in 1994 year by the DELPHI detector, one expects 470.7±21.7 events of Yukawa process in the $h^0b\bar{b} \to b\bar{b}b\bar{b}$ (m_{h^0} = 15 GeV/c^2) final state. The cross section for this process is 9.90±0.02 pb. For comparison, for LEP2 energy of 189 GeV, with 158.07 pb^{-1} data collected in 1998 year the expected number of events for the same process is only 1.55±1.24 and the cross section is $(9.80\pm0.21)\times10^{-3}$ pb. Taking into account efficiencies of the analysis in this final state (described in Section 5) the search for Yukawa process at LEP2 cannot be conclusive.

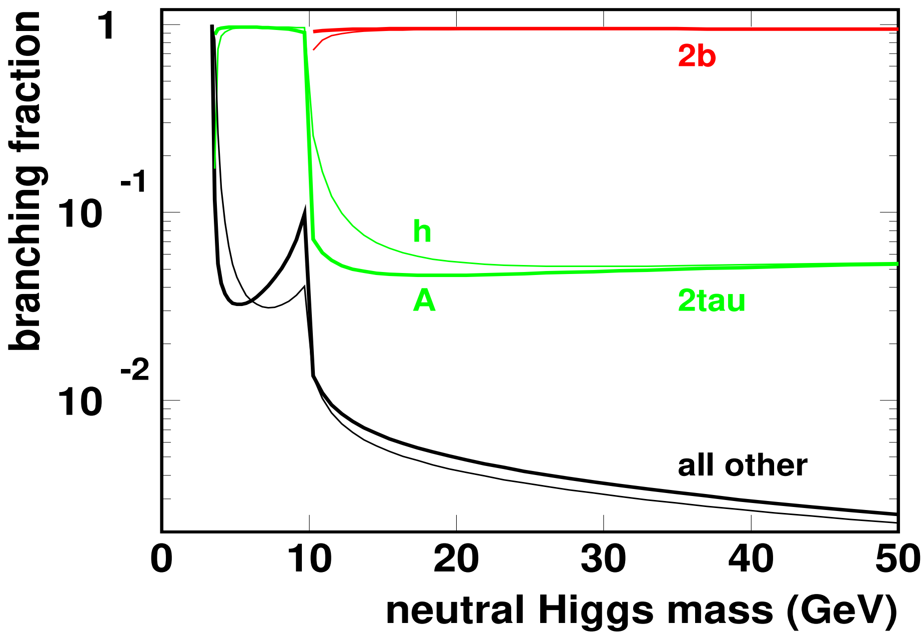

Figure 4.7: Branching fractions for h^0 and A^0 Higgs bosons in 2HDM(II) model, for masses 4-50 GeV/c^2. Plots are presented for tanβ=30 and $\alpha = \beta$. Thick and thin lines represent branching fractions for A^0 and h^0 boson respectively. The differences for low masses come from different kinematic factors for h^0 and A^0 (see text).

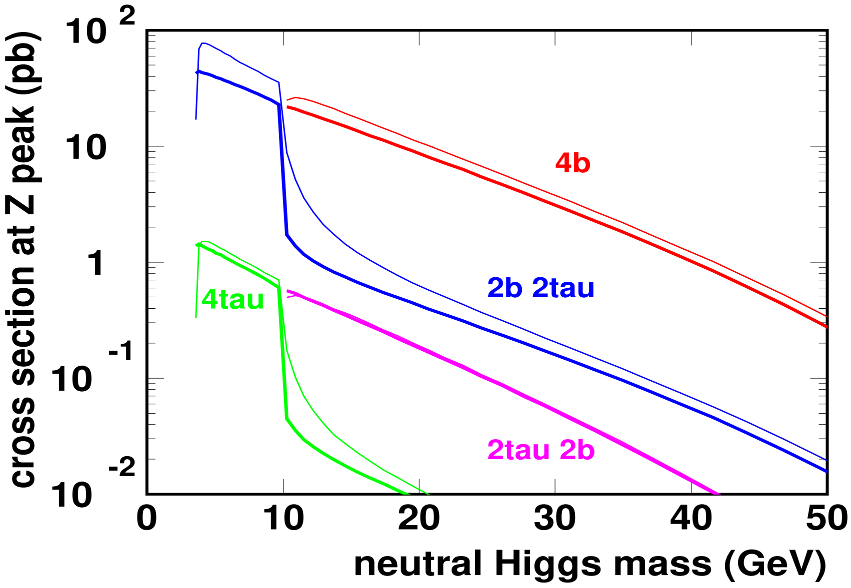

Figure 4.8: Cross sections for h^0 and A^0 Higgs bosons production in the Yukawa process in 2HDM(II) model. The cross sections are given for E_{cms}= 91.25 GeV, and Higgs bosons masses 4-50 GeV/c^2. Thick and thin lines represent cross sections for A^0 and h^0 boson respectively, and for tanβ=30, $\alpha = \beta$.

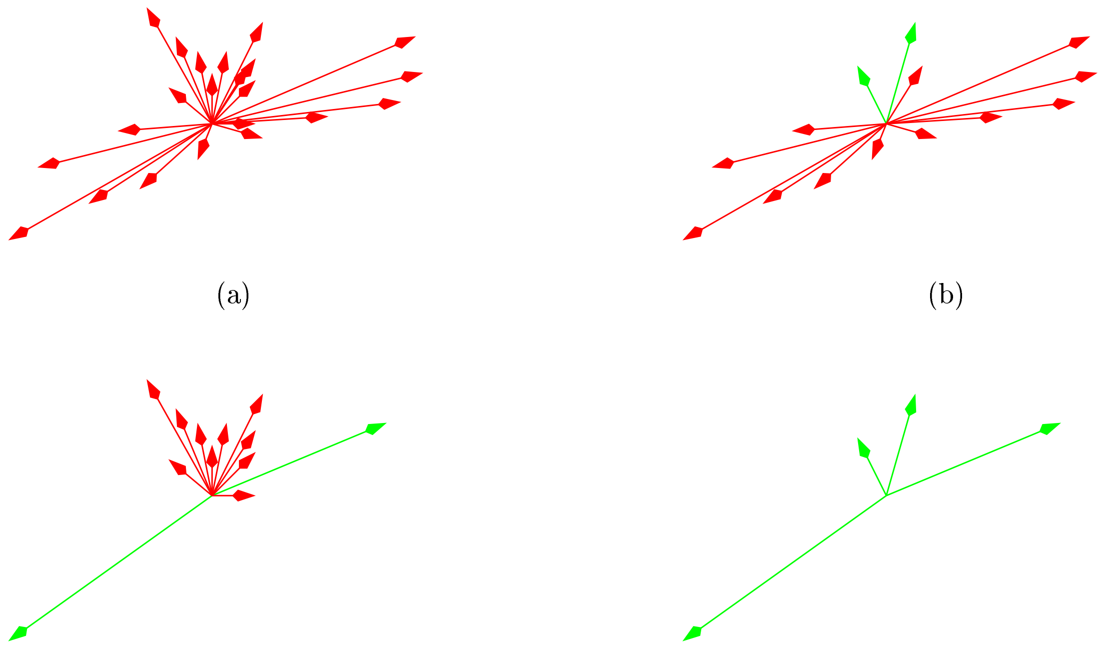

(a) (b)

(c) (d)

Figure 4.9: The Yukawa process final topologies: $b\bar{b}b\bar{b}$ (a), $b\bar{b}\tau^+\tau^-$ (b), $\tau^+\tau^-b\bar{b}$ (c) and $\tau^+\tau^-\tau^+\tau^-$ (d). Green arrows represent decay products of τ leptons (e, μ, charged hadron, or slim, low multiplicity jet of hadrons). Red arrows represent particles coming from decays of hadrons, containing b-quark.

Chapter 5

Analysis

In this chapter the search for light Higgs bosons A^0 and h^0 in the Yukawa process is described. The analysis concerns $Z^0 \to b\bar{b}h^0(A^0)$ and $Z^0 \to \tau^+\tau^- h^0(A^0)$ processes at energies in the center of mass at and around the Z^0 peak (LEP1 phase).

The search done by the author concerns $\tau^+\tau^- b\bar{b}$ and $\tau^+\tau^-\tau^+\tau^-$ final states and is a partial contribution to the whole analysis concerning Yukawa process at DELPHI experiment. The analysis of the $b\bar{b}b\bar{b}$ final state was made by other members of DELPHI collaboration. Its description is given here to give to the reader a full view of the search in the Yukawa process at DELPHI.

Preliminary analyses concerning Yukawa production have been submitted by L3 and ALEPH collaborations to Brussels EPS'95 [34] and Warsaw HEP'96 [26] conferences respectively. Similar analysis has been made by OPAL collaboration [37]. DELPHI analyses of the Higgs production in the Yukawa process were submitted to Tampere EPS'99 [35], Budapest EPS'2001 [36] and Lepton Photon'2001 [36] conferences. Later results, presented in this thesis are a part of a paper submitted to ICHEP2002 conference in Amsterdam [38]. A publication containing these results is in the last phase of internal (DELPHI) revision.

5.1 Data samples and simulation

The data used in this analysis amounts to 80.3 pb^{-1} collected by the DELPHI detector at LEP1, during the years 1994 and 1995. The subsamples and corresponding center-of-mass energies are listed in Table 5.1.

Table 5.1: Center-of-mass energies and corresponding luminosities used in the analysis.

year	1994	1995		
$\sqrt{s}$ (GeV)	91.2	89.44	91.31	92.96
$\mathcal{L}$ (pb^{-1})	46.89	9.02	15.23	9.20

Monte Carlo samples of background and signal events have been produced using `PYTHIA` [39], `KK2f` [40], `EXCALIBUR` [41] and `WPHACT` [42] event generators. Standard Model background samples represent 2 – 100 times the luminosity collected at LEP1, depending on the process type. The signal events were produced at Z^0 resonance with `PYTHIA` generator and program including external matrix-element expressions described in article of M. Krawczyk and J. Kalinowski [43] (see [39], section "*How to include external process in PYTHIA*"). The A^0 and h^0 bosons were taken to be radiated off primary b-quarks or τ-leptons, and decayed into τ-pairs or b-quark pairs. All generated particles were subsequently decayed and hadronized using `JETSET` [39] and then processed through a program `DELSIM` [15] that simulates particles behavior in DELPHI detector. The Yukawa production sample (signal sample) numbers of events, masses of the Higgs bosons and types of final states are shown in Table 5.2.

Table 5.2: The Higgs boson Yukawa production Monte Carlo samples for $\tau^+\tau^-\tau^+\tau^-$, $b\bar{b}\tau^+\tau^-$ and $b\bar{b}b\bar{b}$ final states. The $\tau^+\tau^-b\bar{b}$ final state was not considered in the Yukawa production search at DELPHI experiment.

Signal process	Higgs mass values used in MC generation (GeV/c^2)	No. of events generated for each mass value
$e^+e^- \to \tau^+\tau^-h^0(A^0)$, $h^0/A^0 \to \tau^+\tau^-$	4.1, 7, 9.5, 10, 12, 15, 20, 30, 40, 50	10000
$e^+e^- \to b\bar{b}h^0(A^0)$, $h^0/A^0 \to \tau^+\tau^-$	4.1, 7, 9.5, 10, 12	10000
$e^+e^- \to b\bar{b}h^0(A^0)$, $h^0/A^0 \to b\bar{b}$	11, 13, 15, 20, 30, 40, 50, 60, 70	5000

In all subsequent figures presented in the analyses description the Monte Carlo distributions are normalised to the data luminosity. Representative Higgs boson signal of mass indicated in the figures, is normalised to the data luminosity with cross section given for corresponding mass and tan$\beta = 30$, and scaled by a factor given in the figure in order to show its shape.

5.2 Search in the $\tau^+\tau^-\tau^+\tau^-$ topology

In the $\tau^+\tau^-\tau^+\tau^-$ topology (called also 4τ topology) the following process is considered:

$$e^+e^- \to Z^0 \to \tau^+\tau^-h^0, \text{ or } e^+e^- \to Z^0 \to \tau^+\tau^-A^0,$$

where the Higgs boson decays to $\tau^+\tau^-$ pair.

In the mass interval $2m_\tau < m_{A/h} < 2m_b$, probability of decay into $\tau^+\tau^-$ pair is about 95% of all decays of h^0 and A^0 Higgs bosons. Above $2m_b$ threshold the branching fraction diminishes quickly to about 5%.

Of the four considered final states shown in Figure 4.9 the 4τ topology (Figure 4.9a) is the one that gives relatively clear signature. In Table 5.3 τ^- decay branching fractions are given. Dominating decay modes are 1- and 3-prong modes and they were used in the 4τ channel analysis. Only 4- and 6-prong final states were considered. The 4-prong topology arises from 1-prong decay of each of the τ leptons in the final state. In the 6-prong topology one of the τ leptons decays into three charged particles and remaining τ leptons decay in the 1-prong mode.

Table 5.3: Branching fractions Γ_i/Γ for selected modes of τ^- lepton decays. Given values are taken from *Particle Physic Booklet, July 2002.* "Neutrals" stands for γ's and/or π^0's, "$h^\pm$" stands for $\pi^\pm$ or $K^\pm$. The τ^+ modes are charge conjugates of the modes below.

τ^- decay modes	fraction Γ_i/Γ
Modes with one charged particle	
particle$^-\nu_\tau$ + 0 or more neutrals + 0 or more K^0	(85.35±0.07)%
where:	
$\mu^-\bar{\nu}_\mu\nu_\tau$	(17.37±0.06)%
$e^-\bar{\nu}_e\nu_\tau$	(17.84±0.06)%
$h^-\nu_\tau$ + 1 or more neutrals	(36.91±0.14)%
other	(13.23±0.06)%
Modes with three charged particles	
$h^+\ h^-\ h^-\ \nu_\tau$ + 0 or more neutrals	(14.57±0.07)%
Other modes	(0.08±0.01)%

Taking into account mentioned 4- and 6-prong final states one gets 53.07% and 37.8% initial efficiency of all 4τ possible final states. Other topologies ($\sim$9%) would not improve significantly the search efficiency, while suffering from overwhelming QCD background.

5.2.1 Background types

There are several background types that may give a signature similar to the signal:

Beam–gas collisions are results of beam electrons interactions with remnant gas atoms in the accelerator beam pipe. They usually create a single, low-multiplicity jet of low visible energy.

Photons radiated off particles may convert in the detector and be not recognized, giving additional tracks, especially in Z^0 decays to leptons. They may also fake the signal for low multiplicity hadronic events.

The $Z^0 \to \tau^+\tau^-$ decays are the main background for the Yukawa Higgs boson production in the $\tau^+\tau^-\tau^+\tau^-$ final state, mostly in the topology, where one of τ leptons decays in the 3-prong mode and another one in the 1- or 3-prong mode (1+3 and 3+3 prong topologies). The Feynman diagram for this process is shown in Figure 5.1a.

The Z^0 hadronic decays. In such decays a relatively small number of hadrons is created with signal-alike signature (Figure 5.1b).

Four–fermion events originate from initial and final state radiation (denoted ISR and FSR, respectively). They give very alike signature. Especially $\tau^+\tau^-\tau^+\tau^-$ events make an irreducible background (Figure 5.1c–f).

Two–photon collisions are characterized by small visible invariant mass, large missing energy and large longitudinal momentum with respect to the beam axis. Most particles produced in the interaction usually escape detection disappearing in the beam pipe. However a few particles may reach the barrel part of the detector giving signal-like signature. The diagram for this type of background is shown in Figure 5.1h.

5.2.2 The four–prong event selection

In the four prong event selection only events with exactly four good tracks were accepted, giving total charge equal to zero. A track was considered good if it satisfied the following conditions:

- the measured momentum of the track p_{tot} was greater than 0.4 GeV;
- track length L_{tr} was at least 30 cm;
- its polar angle $|\theta|$ was above 20°,
- its impact parameter towards the event vertex, measured along the beam direction, ip_z, was smaller than 3 cm;
- the track was seen in the TPC [44].

In the signal process four τ leptons are produced, and a part of energy is carried out by neutrinos, coming from the τ leptons decays. Events are characterized by missing visible invariant mass and low multiplicity. Two particles of the opposite charge, being products of τ leptons decays coming from the Higgs boson decay, would give a system, called "**minimal $\pm$ mass**".

Background processes are eliminated by dedicated selection criteria.

And so, the beam–gas interactions and photon conversions were rejected by demanding:

- the sum of charges to be zero;
- the sum of the distances of the closest approach to the beam spot to be smaller than 300μm;

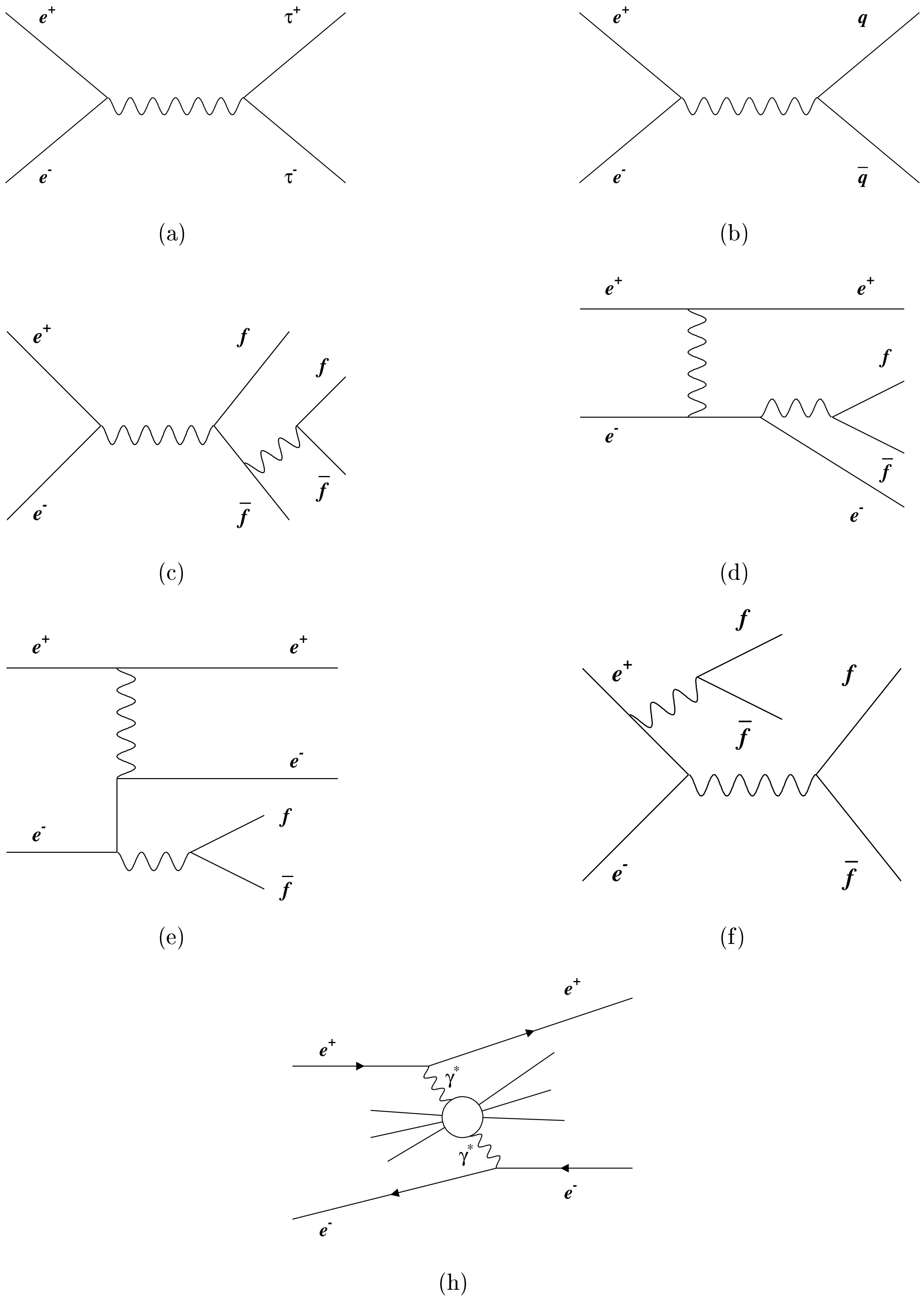

Figure 5.1: Background processes in the Yukawa process 4τ final state: $Z^0 \to \tau^+\tau^-$ decays (a); $Z^0 \to q\bar{q}$ hadronic decays (b); four–fermion events (c) and (f) in the s channel , (d) and (e) in the t channel; two–photon collisions (h). In the figures (c), (d), (e) and (f) "f" denotes quarks: u, c, s, d, b and leptons: e, μ, τ; wavy lines represent Z^0 or γ.

- an existence of charged particle with an angle greater than 90° with respect to the pair of oppositely charged particles of minimal invariant mass;
- γ conversions were reconstructed by the pattern recognition program and further treated as photons. Residual conversions were rejected by requiring minimal invariant $\pm$ mass, $M_{\pm}$, to be greater than 200 MeV/c^2.

The $\gamma\gamma$ events were rejected by requiring:

- the missing momentum along the beam axis, p_{mis} to be smaller than 35% E_{cms};
- the missing transverse momentum, p_{Tmiss}, greater than 5% E_{cms}, or the visible mass, M_{vis}, greater than 25 GeV/c^2.

At this stage of analysis 11876 events were selected in data when 11911±168 were expected from the Monte Carlo simulation, with the identical selection criteria.

The cuts described above (i.e. beam–gas collisions, photon conversion and $\gamma-\gamma$ interactions cuts) establish the preselection level. This means that events at this level satisfy the foregoing criteria.

The main source of background consists of $Z^0 \rightarrow \tau^+\tau^-$ events, in the 1+3 prong topology (described in section 5.2.1, shown in Figure 5.2a and 5.2b).

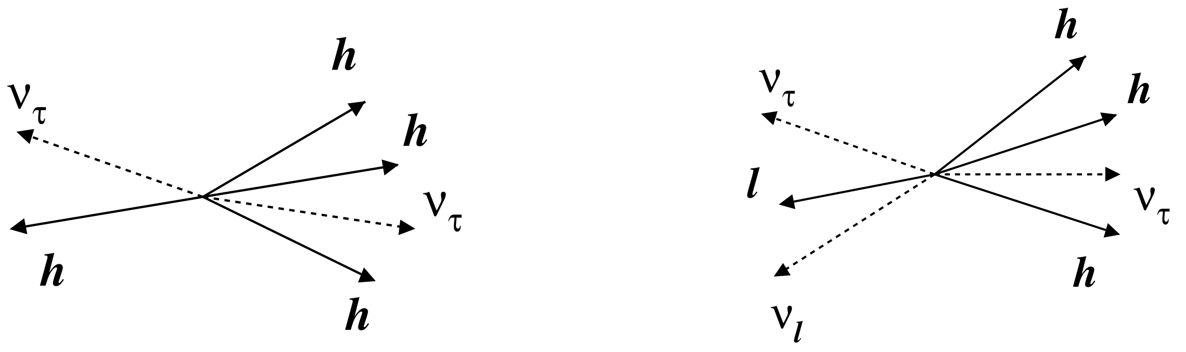

(a) (b)

Figure 5.2: 1+3 prong topologies in $Z^0 \rightarrow \tau^+\tau^-$ decays; "h" stands for charged hadron ($\pi^\pm$ or $K^\pm$), "ℓ" stands for $e^\pm$ or $\mu^\pm$, "ν" stands for both neutrino and anti-neutrino. One of the τ leptons decays in the 3-prong mode and another one in 1-prong mode with a hadron (h) (a), or a lepton (b) in the final state.

They are rejected by demand that the smallest invariant mass created by three of the four tracks, $M_{triplet}$, was greater than 2 GeV/c^2 (Figure 5.3).

Remaining $\tau^+\tau^-$ events originate from the 3+3 prong topology, where one charged particle is missed in each of two hemispheres of the event (Figure 5.4). They are rejected by requirement

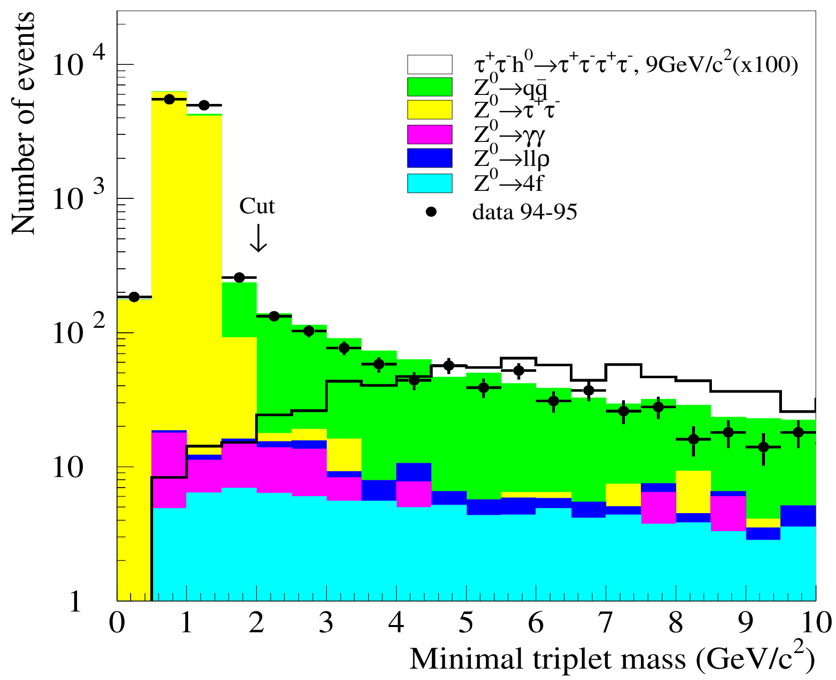

Figure 5.3: Minimal triplet mass (see description in text) in the four-prong topology after the preselection cuts. The dots represent data, histograms – different background types, black line represents typical Higgs boson signal (here – h^0 bosons, m_{h^0} = 9 GeV/c^2), scaled by a factor of 100 in order to show its shape. The arrow indicates the cut described in the text – events on the left side of the arrow are rejected.

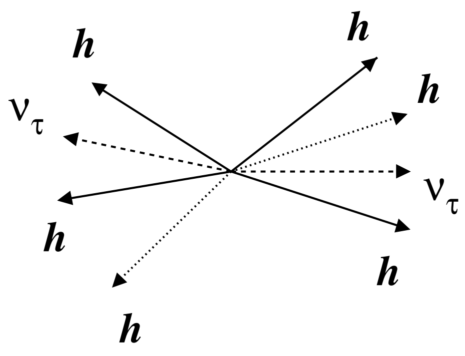

Figure 5.4: 3+3 prong topology in $Z^0 \to \tau^+\tau^-$ decays with one charged particle missing in each hemisphere; "h" stands for charged hadron ($\pi^\pm$ or $K^\pm$), "ν" stands for both neutrino and anti-neutrino, dotted and dashed lines represent particles not detected.

that an invariant mass of particles recoiling against the "minimal ± pair", M_{rec2} is greater than 2 GeV/c^2. After these cuts 8.78±3.23 events of 9200±166 (at the preselection level), coming from $Z^0 \to \tau^+\tau^-$ decays are expected to remain in data. At this stage 574 events were selected in data and 605.1±17.7 expected.

Most of the remaining background events are expected to be hadronic decays of Z^0. The reduction of this background was performed by the following requirements:

- more than 10% of the visible mass M_{vis} was carried by the pair recoiling against "minimal ± pair";
- the total multiplicity N_{tot} in the event should not exceed 10.

At this level of the analysis 137 events are found in data, while 145.8±6.7 are expected.

Majority of the residual events are leptonic and lepto-hadronic four-fermion ones. The four-fermion events that do not contain τ leptons are eliminated by demand that visible invariant mass M_{vis} should be smaller than 60 GeV/c^2. The remaining events are $\tau^+\tau^- f\bar{f}$ (f=e, μ, π) and irreducible genuine second order electro-weak 4τ events. The visible invariant mass after anti–τ and anti–$q\bar{q}$ cuts is presented in Figure 5.5.

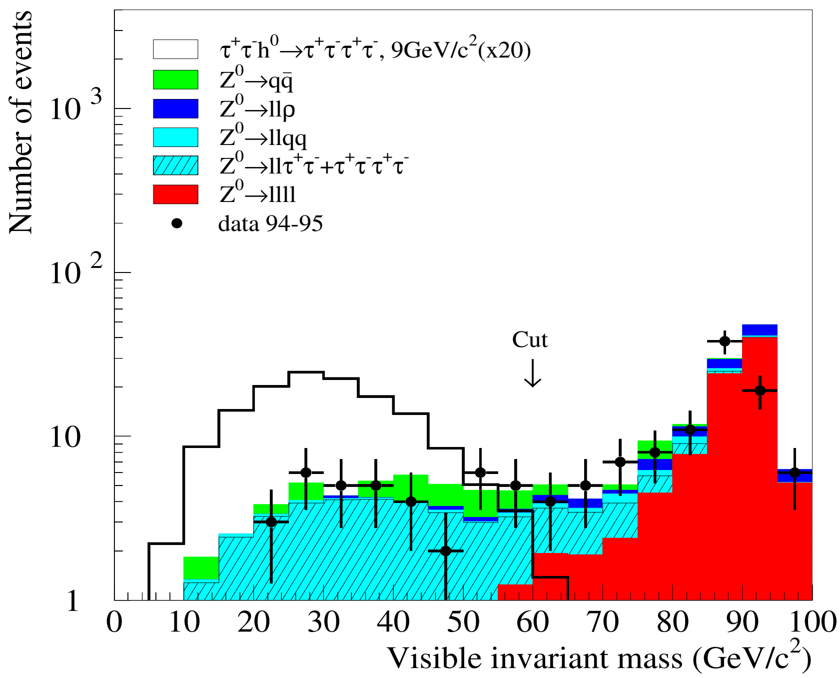

Figure 5.5: Visible invariant mass for the four-prong analysis in the 4τ final state of the Yukawa process, after $\tau^+\tau^-$ and $q\bar{q}$ cuts. Dots represent data and histograms different background types. Black line represents typical Higgs h^0 boson signal (m_{h^0} = 9 GeV/c^2), scaled by a factor of 20 to show its shape. The arrow indicates the cut described in the text – events on the right side of the arrow are rejected.

To eliminate the first category a special 4τ selection was applied:

- one of the particles creating the "minimal $\pm$ pair" must be identified as a lepton;
- the other particle in this pair cannot be identified as a lepton of the same flavour;
- particles creating the pair recoiling against the "minimal $\pm$ pair" cannot be identified as leptons of the same flavour.

After all the cuts described above, an additional one was applied. The invariant mass of the "minimal $\pm$ pair", $M_{\pm}$ had to be greater than 1 GeV/c^2 (Figure 5.6).

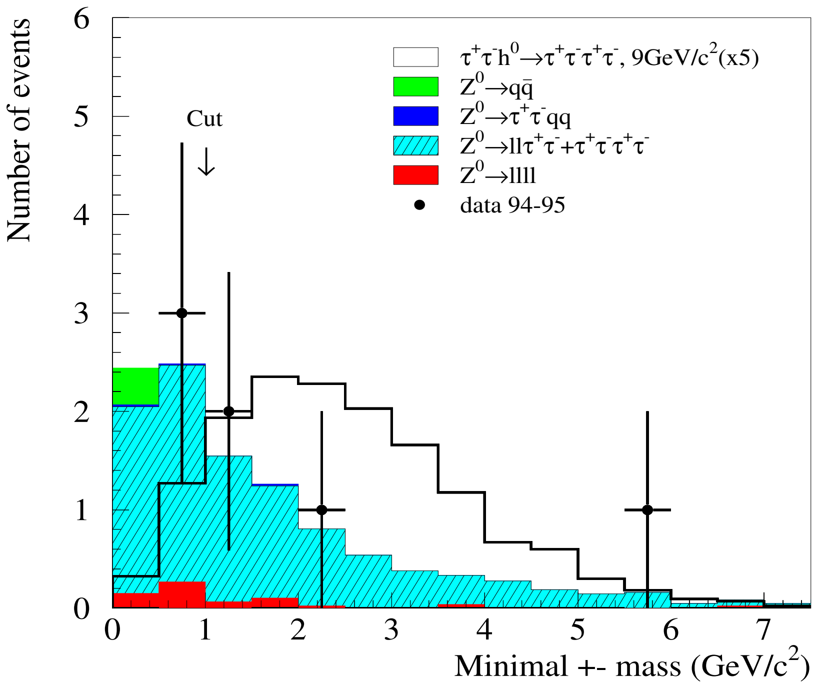

Figure 5.6: Mass of the "minimal $\pm$ pair" in the four-prong analysis. The picture shows events remaining after $\tau^+\tau^-$ and $q\bar{q}$ cuts, and the cuts for visible mass and pro-4τ selection. Dots represent data and histograms – different background types. Black line represents typical Higgs h^0 boson signal (m_{h^0} = 9 GeV/c^2), scaled by a factor of 5 to show its shape. The arrow indicates the cut described in the text – events on the left side of the arrow are rejected.

The final number of 4 events in data was found and 4.09$\pm$0.47 events were expected from the MC simulations, where 0.248$\pm$0.083 are predicted to come from $\ell\ell\ell\ell$ ($\ell = e, \mu$), 3.830$\pm$0.459 from $\ell\ell\tau\tau$ and 0.013$\pm$0.012 from $q\bar{q}\tau\tau$ events. The final signal efficiencies for the Higgs bosons are shown in Table 5.4. The signal efficiency is defined as a ratio of the number of events that passed all selection criteria $N_{all\ cuts}$ to the number of events before any cut was applied N_0 (see Table 5.2):

$$\epsilon_s = \frac{N_{all\ cuts}}{N_0}$$

Example four-prong events that passed the described analysis selection criteria, for MC signal simulation (h^0 Higgs boson, $m_{h^0} = 9$ GeV/c^2) and real data are displayed in Figures 5.7 and 5.8 respectively. The events are shown with DELGRA program [45], an interactive program that provides event information in graphic form.

Table 5.4: Final signal efficiencies for A^0 and h^0 Higgs bosons in the four-prong analysis of $\tau^+\tau^-\tau^+\tau^-$ final state.

Higgs boson mass (GeV/c^2)	h^0 efficiency (%)	A^0 efficiency (%)
4.1	3.02±0.17	3.19±0.18
7.0	5.27±0.23	5.62±0.24
9.0	5.80±0.24	5.93±0.24
10.5	5.97±0.24	5.67±0.24
12.0	6.32±0.25	6.24±0.25
15.0	5.94±0.24	6.23±0.25
20.0	6.12±0.25	5.74±0.24
30.0	6.24±0.25	5.82±0.24
40.0	6.52±0.26	6.26±0.25
50.0	6.24±0.25	5.86±0.24

5.2.3 The six–prong event selection

In order to improve the selection efficiency in 4τ channel, events with the 1+1+1+3 prong decay mode (6–prong final states) were included in this analysis.

Events with exactly six good charged particles of total electric charge equal to zero, seen in the TPC were considered. The same track selection criteria were applied as for four-prong events (section 5.2.2). The preselection cuts, described in the previous section concerning $\gamma\gamma$, beam–gas and γ conversions were applied in the 6–prong event selection as well. In the data 6733 events pass the preselection criteria, while 6760.9±84.8 are expected from the MC simulations.

Since one of τ leptons is expected to decay in the 3–prong mode, the smallest invariant mass of a triplet system $M_{triplet}$ should not exceed m_τ. The cut was applied at 1.8 GeV/c^2 (Figure 5.9) with an additional requirement that the total triplet momentum p_{3tot} was greater than 3 GeV/c. Since then the triplet is treated as a pseudo-particle, and the six-prong topology becomes a pseudo-four one (as it is shown in Figure 5.10).

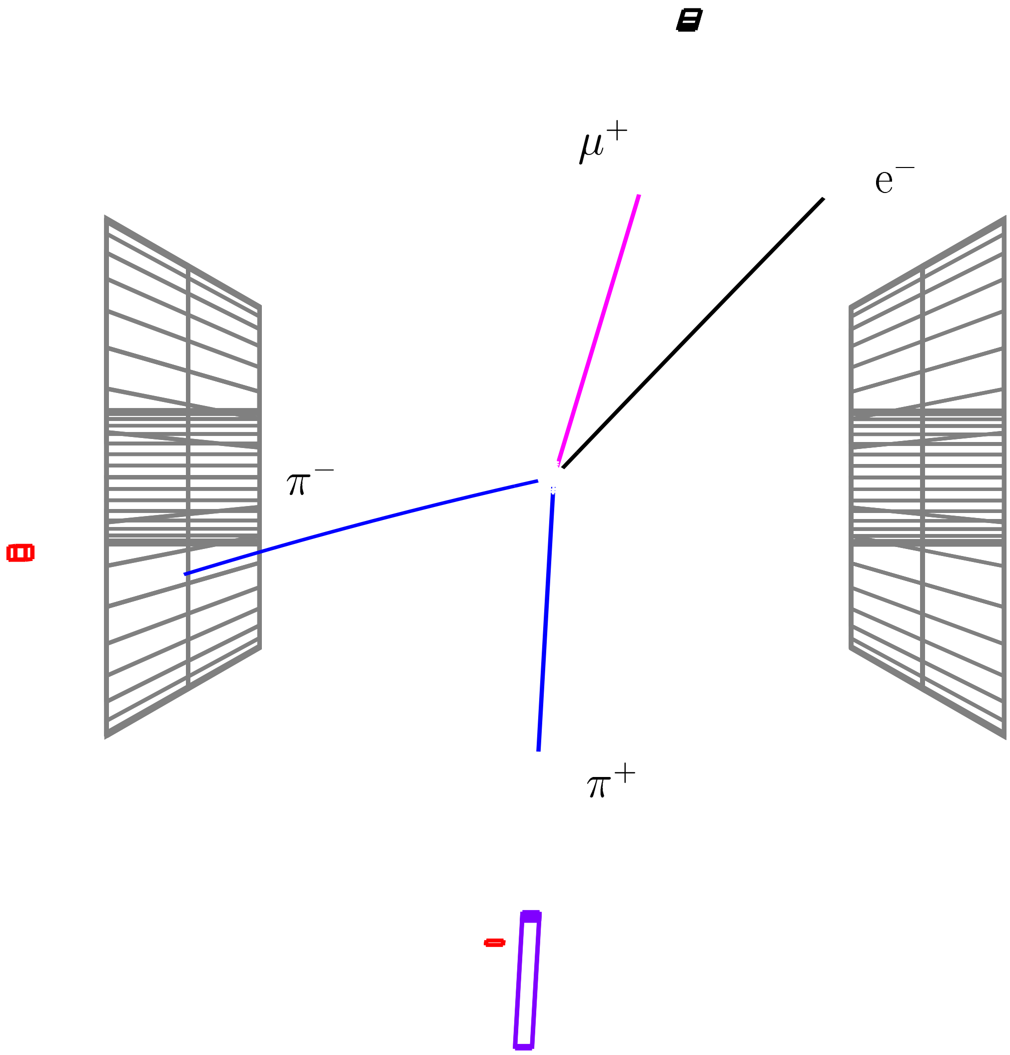

Figure 5.7: Typical Higgs boson (here: h^0, $m_{h^0} = 9$ GeV/c^2) simulated event of the four-prong $\tau^+\tau^-\tau^+\tau^-$ final state, seen in DELPHI detector. The event satisfies all selection criteria described in the text. Four charged particles were identified: e^- ($p_{e^-} = 7.2$ GeV/c), μ^+ ($p_{\mu^+} = 15.5$ GeV/c), π^- ($p_{\pi^-} = 24.2$ GeV/c) and π^+ ($p_{\pi^+} = 9.3$ GeV/c). Different kinds of particles are displayed with different colors. Forward RICH detector is displayed in grey, in order to show the orientation of the display – see the detector schematic view and description in Chapter 3. Color cuboids represent energy deposits in the hadron calorimeter (not displayed here for legibility).

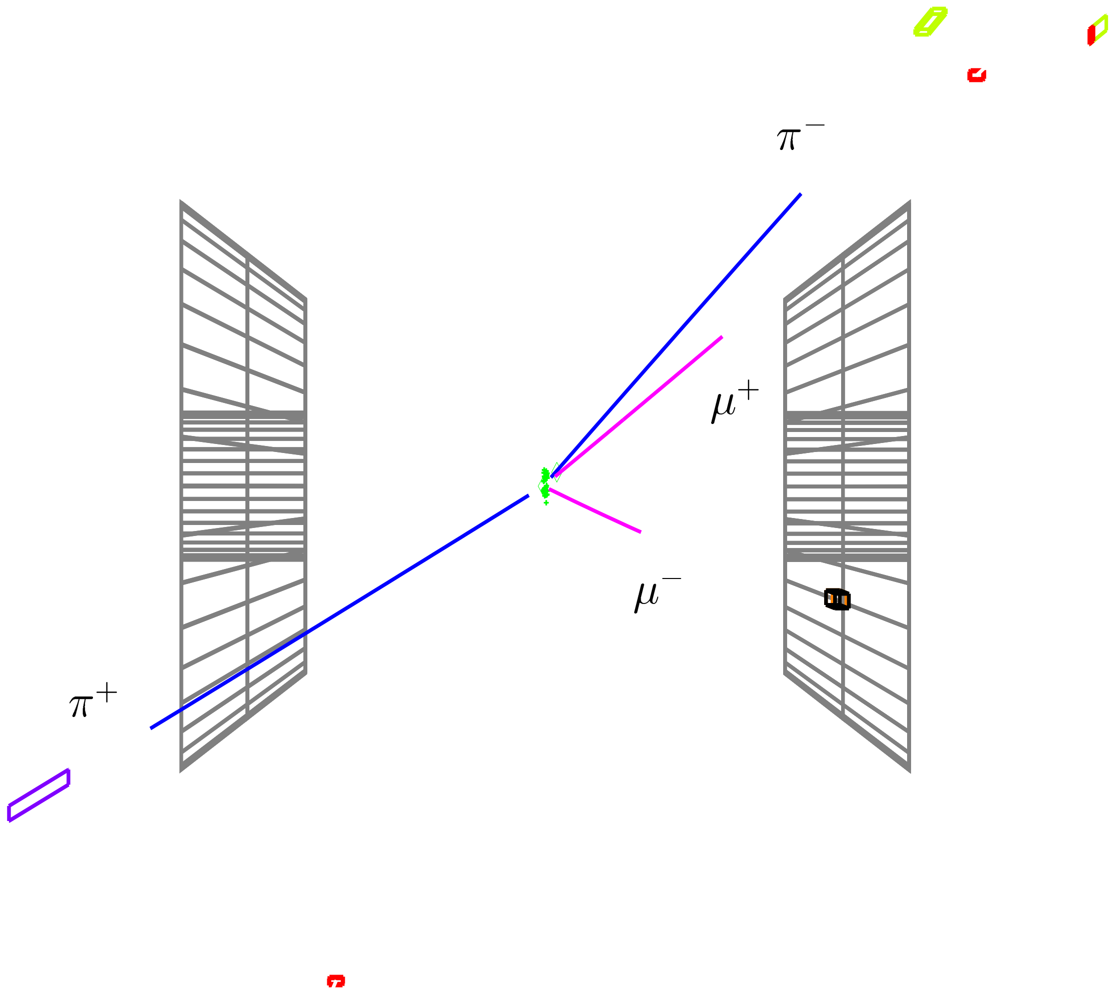

Figure 5.8: Real data event of the four-prong $\tau^+\tau^-\tau^+\tau^-$ final state, seen in DELPHI detector. The event satisfies all selection criteria described in the text. Four charged particles were identified: π^- (p_{π^-} = 17.7 GeV/c), π^+ (p_{π^+} = 16.3 GeV/c), μ^- (p_{μ^-} = 18.1 GeV/c) and μ^+ (p_{μ^+} = 3.5 GeV/c). Different kinds of particles are displayed with different colors. Forward RICH detector is displayed in grey, in order to show the orientation of the display – see the detector schematic view and description in Chapter 3. Color cuboids represent energy deposits in the hadron calorimeter (not displayed here for legibility).

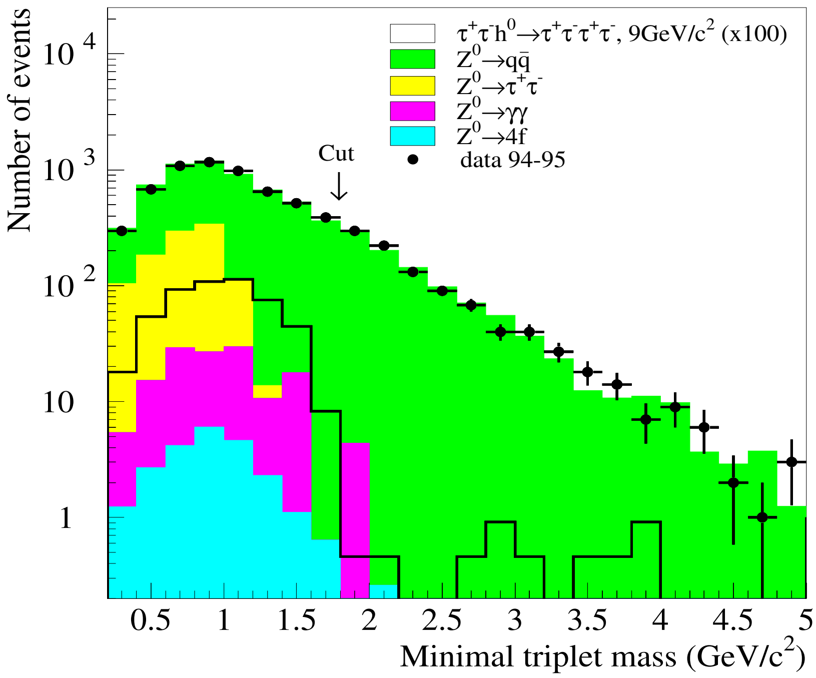

Figure 5.9: Minimal triplet mass (see description in text) in the six-prong topology after the preselection cuts. The dots represent data, histograms – different background types, black line represents typical Higgs boson signal (here – h^0 bosons, $m_{h^0} = 9$ GeV/c^2, scaled by a factor of 100, in order to show its shape. The arrow indicates the cut described in the text – events on the right side of the arrow are rejected.

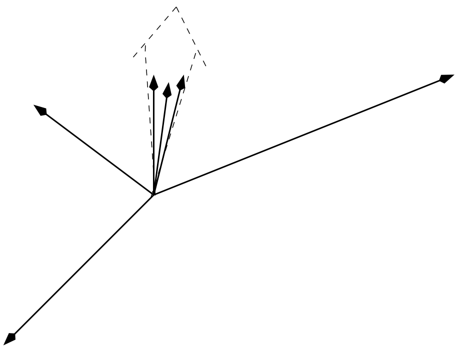

Figure 5.10: In the 6-prong topology one of τ leptons decays in 3-prong mode. The three particles are treated as one pseudo-particle. Arrows represent charged particles, coming from τ leptons decay.

To reject low multiplicity hadronic Z^0 decays and $\tau^+\tau^-$ pairs in the 3+3 prong topology, the mass recoiling against the smallest triplet mass, M_{rec3} was required to exceed 4 GeV/c^2 (Figure 5.11). Moreover, the visible energy M_{vis} was required to be less than 80 GeV/c^2, and the total multiplicity N_{tot} smaller than 13.

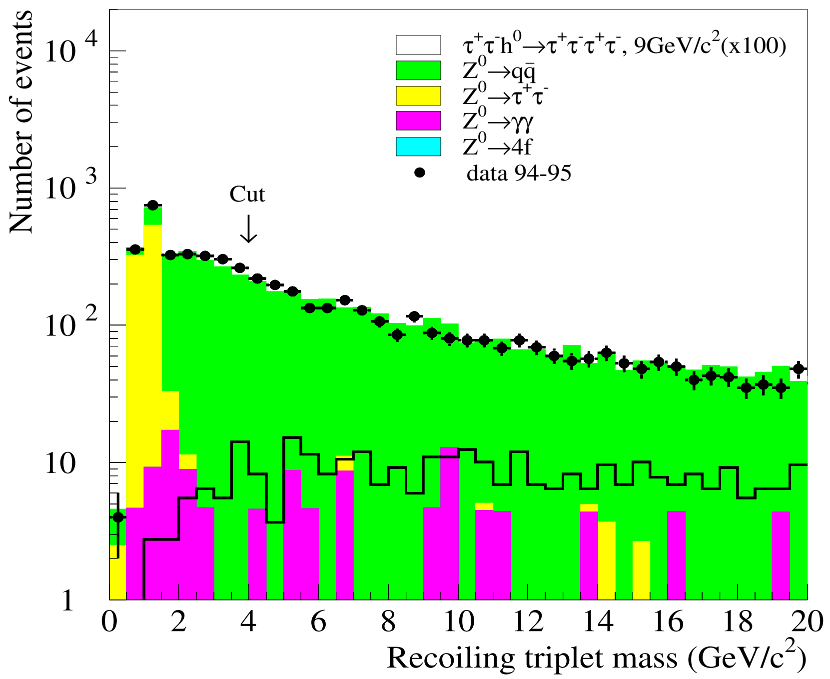

Figure 5.11: Mass of the system of particles recoiling the triplet of minimal mass (see description in the text) in the six-prong topology after the cuts described in the text. The dots represent data, histograms – different background types, black line represents typical Higgs boson signal (here – h^0 bosons, m_{h^0} = 9 GeV/c^2, scaled by a factor of 100 in order to show its shape. The arrow indicates the cut described in the text – events on the left side of the arrow are rejected

At this stage 58 events were selected in the data, when 61.8±11.7 were expected from MC of which 52.3±5.7 were predicted to be of $Z^0 \to q\bar{q}$ origin.

To eliminate remaining $Z^0 \to q\bar{q}$ and $\tau^+\tau^-$ events one identified lepton among the particles recoiling against the triplet was demanded. The cut on the "minimal ± pair", $M_\pm$ was applied at 1 GeV/c^2 (Figure 5.12). After all these cuts 4 events remained in the data in 6–prong topology, when 5.96±1.50 events were expected, where 3.38±1.43 come from $q\bar{q}$, 1.90±0.15 from $\tau^+\tau^-\ell^+\ell^-$ + $\tau^+\tau^-\tau^+\tau^-$ and 0.62±0.13 from $\ell^+\ell^-q\bar{q}$+$\tau^+\tau^-q\bar{q}$. The final signal efficiencies for the Higgs bosons in the 6-prong topology analysis are shown in Table 5.5.

Example six-prong events that passed the described analysis selection criteria, for MC signal simulation (h^0 Higgs boson, m_{h^0} = 9 GeV/c^2) and real are displayed in Figures 5.13 and 5.14 respectively.

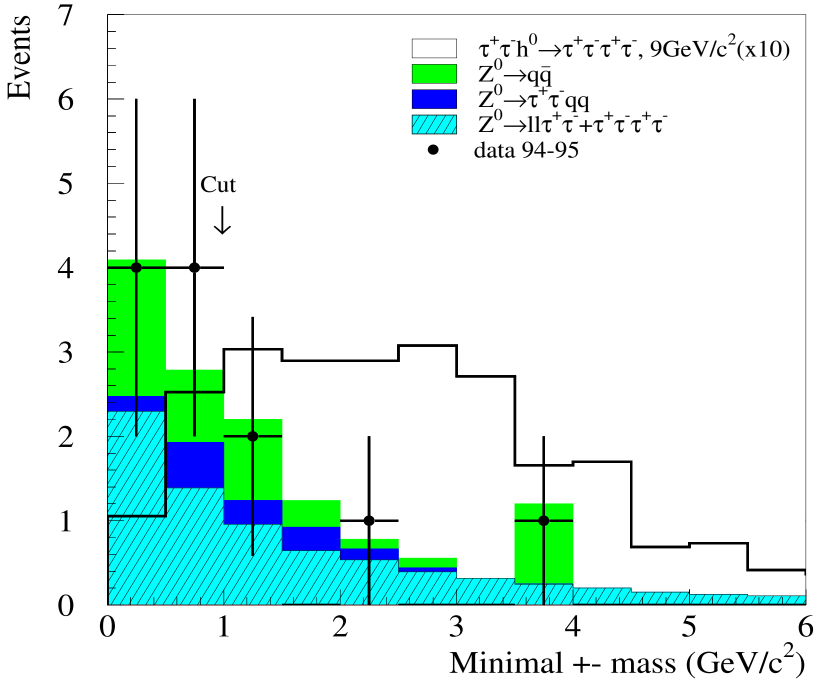

Figure 5.12: Mass of the "minimal ± pair" in the six-prong analysis after cuts described in the text. Dots represent data and histograms – different background types. Black lines represents typical Higgs h^0 boson signal (m_{h^0} = 9 GeV/c^2), scaled by a factor of 10 in order to show its shape. The arrow indicates the cut described in the text – events on the left side of the arrow are rejected.

Table 5.5: Final signal efficiencies for A^0 and h^0 Higgs bosons in the six-prong analysis of $\tau^+\tau^-\tau^+\tau^-$ final state.

Higgs boson mass (GeV/c^2)	h^0 efficiency (%)	A^0 efficiency (%)
4.1	2.39±0.15	2.46±0.16
7.0	3.93±0.20	4.32±0.21
9.0	4.46±0.21	4.59±0.21
10.5	4.28±0.21	4.61±0.21
12.0	4.74±0.22	4.60±0.21
15.0	4.65±0.22	4.78±0.22
20.0	5.59±0.24	4.75±0.22
30.0	5.46±0.23	5.35±0.23
40.0	5.46±0.23	5.28±0.23
50.0	5.64±0.24	5.21±0.23

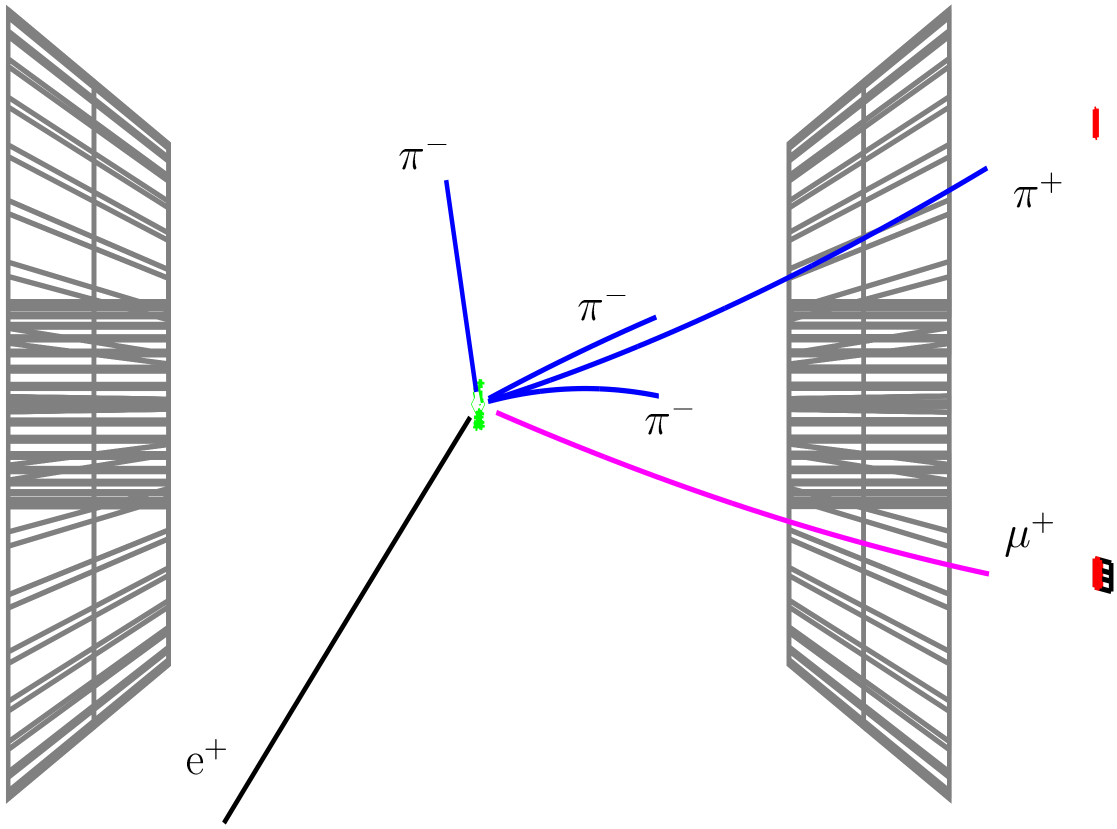

Figure 5.13: Typical Higgs boson (here: h^0, $m_{h^0} = 9$ GeV/c^2) simulated event of the six-prong $\tau^+\tau^-\tau^+\tau^-$ final state, seen in DELPHI detector. The event satisfies all selection criteria described in the text. Six charged particles were identified: e^+ ($p_{e^+} = 13.9$ GeV/c), μ^+ ($p_{\mu^+} = 3.7$ GeV/c), 3 π^- ($p_{\pi^-} = 1.4$, 5.5 and 18.2 GeV/c) and π^+ ($p_{\pi^+} = 2.6$ GeV/c). Different kinds of particles are displayed with different colors. Forward RICH detector is displayed in grey, in order to show the orientation of the display – see the detector schematic view and description in Chapter 3. Color cuboids represent energy deposits in the hadron calorimeter (not displayed here for legibility).

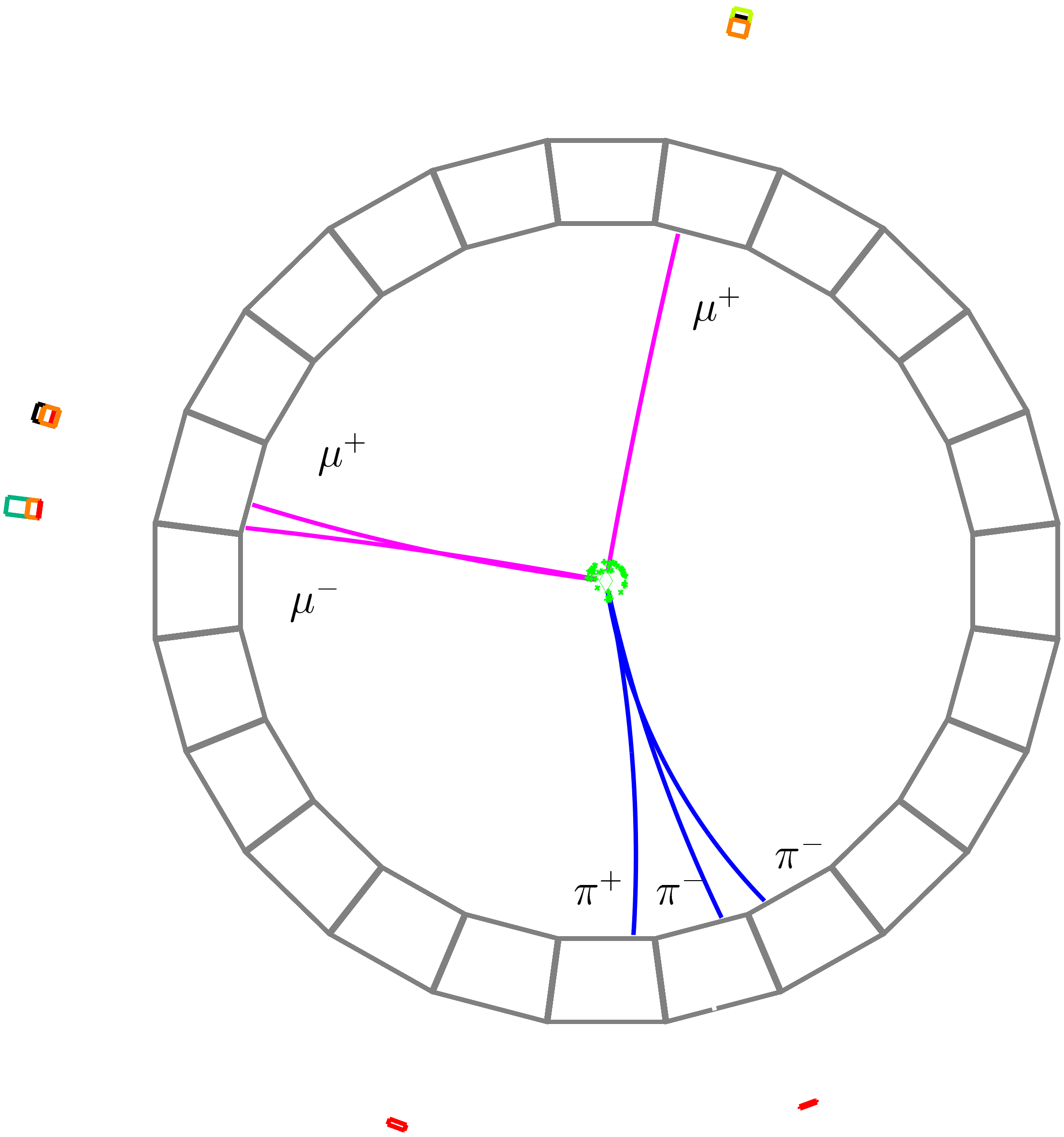

Figure 5.14: Real data event of the six-prong $\tau^+\tau^-\tau^+\tau^-$ final state, seen in DELPHI detector. The event satisfies all selection criteria described in the text. Six charged particles were identified: 2 π^- (p_{π^-} = 1.3 and 3.6 GeV/c), π^+ (p_{π^+} = 3.1 GeV/c), 2 μ^+ (p_{μ^+} = 4.4 and 13.7 GeV/c) and μ^- (p_{μ^+} = 14.6 GeV/c). Different kinds of particles are displayed with different colors. Barrel electromagnetic calorimeter is displayed in grey, in order to show the orientation of the display – see the detector schematic view and description in Chapter 3. Color cuboids represent energy deposits in the hadron calorimeter (not displayed here for legibility).

5.2.4 Systematic errors

Systematic uncertainties are evaluated by inspection of the differences in rejection between data and expected background. The examination was performed at the preselection level and for each cut. This means that every cut efficiency for data and the MC simulation was checked at the preselection level, giving i-cut efficiencies: ϵ_{iDATA} and ϵ_{iMC}. The efficiencies ϵ_i are defined as a ratio of the number of events that passed $i-$th cut N_i to the number of events at the preselection level N_{pres}:

$$\epsilon_i = \frac{N_i}{N_{pres}}$$

Then a relative difference is defined for every cut [46]:

$$\mathrm{err}_i = \frac{|\epsilon_{iDATA} - \epsilon_{iMC}|}{\epsilon_{iMC}}$$

Under assumption that the uncertainties are uncorrelated, the total systematic error for the MC simulation is:

$$\mathrm{Err}_{totMC} = \sqrt{\sum_i \mathrm{err}^2_{iMC}}$$

The signal systematic uncertainty err_{is} for the signal sample was rescaled by a factor considering MC and the signal efficiencies for every cut [47]:

$$\mathrm{err}_{is} = \mathrm{err}_{iMC} \cdot \sqrt{\epsilon_{is} \cdot (1 - \epsilon_{is})} / \sqrt{\epsilon_{iMC} \cdot (1 - \epsilon_{iMC})}$$

where ϵ_{is} is the signal efficiency after i-cut and err_{is} is signal uncertainty for the i-cut and added in quadrature:

$$\mathrm{Err}_{tots} = \sqrt{\sum_i \mathrm{err}^2_{is}}$$

Systematic error evaluation for four-prong and six-prong analysis, for MC simulations and for A^0 and h^0 signals are given in Table 5.6.

Table 5.6: Evaluation of systematic errors on efficiency in 4τ analysis.

	four-prong analysis syst. error (%)	six-prong analysis syst. error (%)
'94 + '95 MC	16.47	3.64
h^0 signal, $\mathrm{m}_{h^0} =$ 4.1 GeV/c^2	9.03	2.48
7.0 GeV/c^2	11.11	2.62
9.5 GeV/c^2	11.81	2.66
10.0 GeV/c^2	12.10	2.71
12.0 GeV/c^2	12.35	2.73
15.0 GeV/c^2	12.44	2.76
20.0 GeV/c^2	12.54	2.83
30.0 GeV/c^2	12.65	2.82
40.0 GeV/c^2	12.74	2.83
50.0 GeV/c^2	12.64	2.81
A^0 signal, $\mathrm{m}_{A^0} =$ 4.1 GeV/c^2	9.16	2.50
7.0 GeV/c^2	11.33	2.67
9.5 GeV/c^2	11.84	2.75
10.0 GeV/c^2	12.07	2.69
12.0 GeV/c^2	12.28	2.75
15.0 GeV/c^2	12.38	2.80
20.0 GeV/c^2	12.48	2.75
30.0 GeV/c^2	12.66	2.81
40.0 GeV/c^2	12.64	2.81
50.0 GeV/c^2	12.45	2.80

5.3 Search in the $b\bar{b}\tau^+\tau^-$ topology

In the $b\bar{b}\tau^+\tau^-$ ($2b2\tau$) topology, the Higgs boson is radiated off b or $\bar{b}$ quark:

$$e^+e^- \to Z^0 \to b\bar{b}h^0, \text{ or } e^+e^- \to Z^0 \to b\bar{b}A^0,$$

and decays into $\tau^+\tau^-$ pair. In the mass interval $2m_\tau < m_{A/h} < 2m_b$ h^0 and A^0 Higgs bosons decay mostly into $\tau^+\tau^-$ (see section 5.2). In the final state two jets, coming from b quarks hadronization, are expected. The products of τ leptons decays may "hide" in the b jets, or create one or two jets, depending on mass and energy of the Higgs boson. The possible topologies are then two- three- and four-jet. To optimize the analysis, three-jet topology was considered, where decay products of τ leptons that come from the Higgs boson create a single, collimated, low multiplicity jet. The other two jets are expected to be of high multiplicity, coming from b-quarks decays.

5.3.1 Background types

Three types of background were considered to give a signature similar to the signal:

Two–photon collisions description is given in Section 5.2.1. This kind of background can be almost entirely removed by the preselection cuts;

Four–fermion processes are mainly $e^+e^- \to Z^0 \to f\bar{f}$ events with initial or final state radiation. They can be divided into two classes: $\ell^+\ell^-\ell^+\ell^-$ and $q\bar{q}f\bar{f}$ $(f = q,\ \ell)$. The first class is eliminated by the preselection cuts. The latter class contains events very alike the signal (i.e. $b\bar{b}\ell^+\ell^-$, where the charged lepton (e, μ, τ) pair comes from final state radiation).

The Z^0 hadronic decays. This kind of background consists of $e^+e^- \to Z^0/\gamma \to q\bar{q}$ events, with gluons radiated off the quarks. Especially $b\bar{b}g$ events are very likely to have the signal characteristics, what makes it main background.

The two-photon collisions and the four-fermion background processes are illustrated in Figure 5.1, the Z^0 hadronic decays are shown in Figure 5.15.

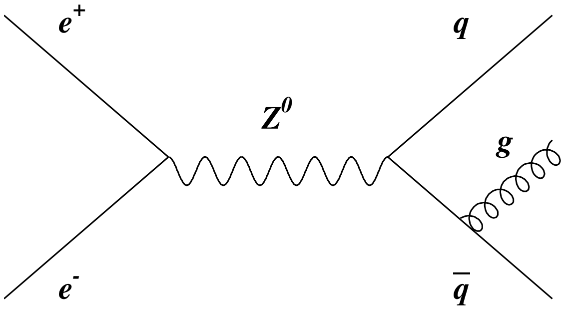

Figure 5.15: The background process $e^+e^- \to Z^0/\gamma \to q\bar{q}g$ for the $b\bar{b}\tau^+\tau^-$ final state; "q" stands for u, c, d, s, and b quarks.

5.3.2 The event selection

In presented analysis all events were reconstructed in 3-jet topology. DURHAM algorithm [48] was used for jet clustering. General description of the clustering algorithms is given in Appendix A. DELPHI b-quark tagging algorithm [49] was then applied for jets and for whole events as well. The higher value of b-tagging variable, the larger probability that a jet or an event contains a b–quark (quarks).

Only events with total multiplicity $\mathrm{N}_{tot} > 10$ were considered. The $2 \to 3$ jet resolution parameter y_{32} of DURHAM algorithm was required to be greater than 0.01 (Figure 5.16). Events with the event b-tagging variable B_{evt} value greater than 0. were accepted. This cut suppresses most of non-b $q\bar{q}$ events and eliminates almost entirely $\gamma-\gamma$ background. These cuts establish the preselection level. At this stage 309115 events were found in data, while 310204±390 expected from Monte Carlo simulations.

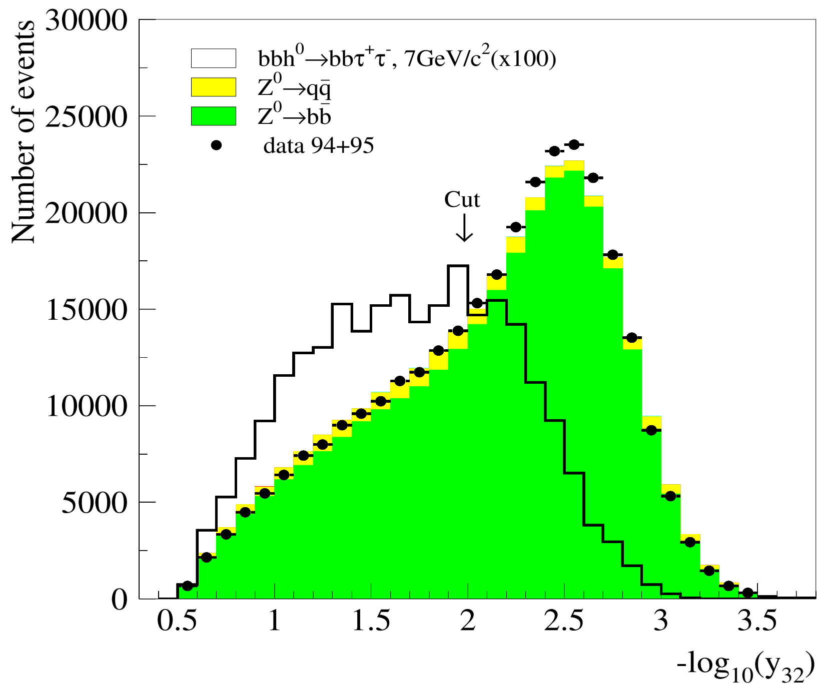

Figure 5.16: Distance measure y_{32} in DURHAM algorithm for $2b2\tau$ analysis after event B$_{evt}$ cut. On the horizontal axis -log(y_{32}) value is shown. The cut value equal to 0.01 (see description in text) corresponds to -log(y_{32}) = 2. The dots represent data. Only two main kinds of background are shown (histograms) – other background processes give small contribution and are not visible. Black line represents typical h^0 Higgs boson signal (m$_{h^0}$ = 7 GeV/c^2, scaled by a factor of 50 in order to show its shape. The arrow indicates the cut described in the text – events on the right side of the arrow are rejected.

Jets in every event were then classiffied according to their b-tagging values x_{bi}. The jet with the highest b–tagging value (x_{b1}) is called "1^{st} jet", with the medium value (x_{b2}) – "2^{nd} jet". One expects that decay products of τ leptons that come from the Higgs boson to create a low multiplicity and the smallest b–value jet (called "3^{rd} jet").

After the preselection cuts, remaining background consists mostly of $Z^0 \to q\bar{q}$ events. Events with gluons radiated off the quarks are very alike the signal. Gluon jets are usually of high multiplicity, with low b-tagging variable value.

The first two jets (of highest and medium b-tagging value – 1^{st} and 2^{nd} jet) had to be b-tagged well enough. Cuts on their x_{b1} and x_{b2} values were set to be higher than 0. and -1., respectively. This cut leaves mostly $Z^0 \to b\bar{b}$ events.

To avoid bad–clustered events, which are originally back-to-back (two-jet, $q\bar{q}$ events, where several tracks were assigned to the 3^{rd} jet), one requires the angular distance (α) between the 1^{st}

and 2^{nd} jet direction to be less than 154°, or more than 206° : $|\cos\alpha_{12}|$ <0.9 At this stage 38165 events are found in data, while 38384.68±127.31 are expected from Monte Carlo simulations.

The 3^{rd} jet is supposed to be induced by the τ pair and is expected to be of low multiplicity (only charged particles, with the total momentum $p_{tot} > 1$ GeV/c were taken into account, as shown in Figure 5.17), containing at least one identified electron or muon:

- number of charged particles in the 3^{rd} jet: $1 \leq N_{ch} \leq 3$,
- number of leptons in the 3^{rd} jet: $N_{lepton} \geq 1$.

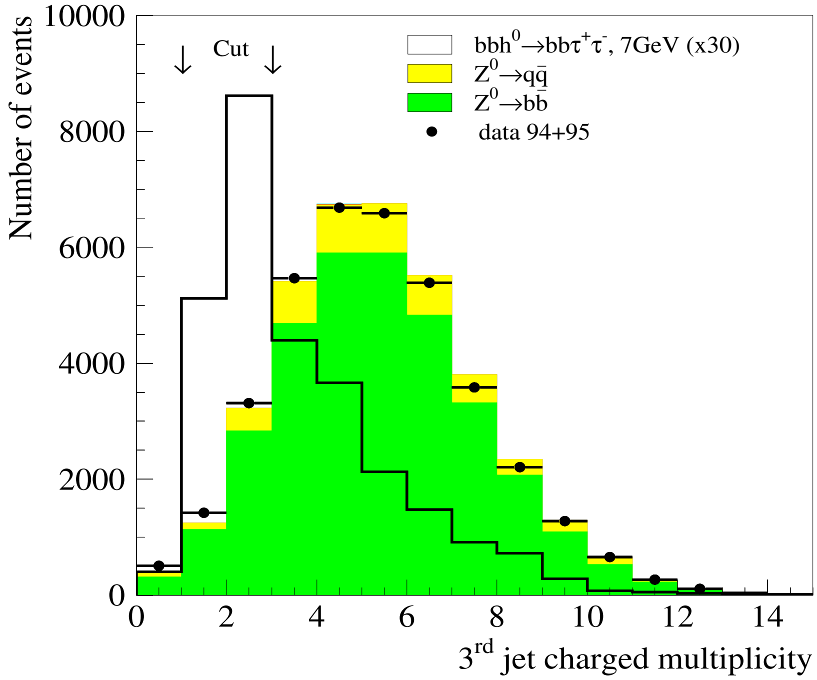

Figure 5.17: 3^{rd} jet charged multiplicity after the cuts concerning x_{b1}, x_{b2} and $\cos\alpha_{12}$ variables. The dots represent data. Only two main kinds of background are shown (histograms) – other background processes give small contribution and are not visible. Black line represents typical h^0 Higgs boson signal (m_{h^0} = 7 GeV/c^2, scaled by a factor of 30 to show its shape. Arrows indicate the cut described in the text. Events between the arrows are accepted.

The 3^{rd} jet is expected to be relatively narrow, differing from a gluon jet in $b\bar{b}g$ events (which is usually broad and of high multiplicity), while both kinds of jets are supposed to be of low b-tagging value. Width of the 3^{rd} jet (defined as the angle between two the most distant tracks in the jet) had to be less or equal to 50° ($\cos(width_3) \geq 0.64$). The width is 0 ($\cos(width_3)$ = 1) for a single-track jet. The variable is shown in Figure 5.18

As in the 3^{rd} jet at least one identified lepton is required, an additional cut was applied: the transverse momentum of the identified lepton p_{T-out} to be greater than 1 GeV/c. It was

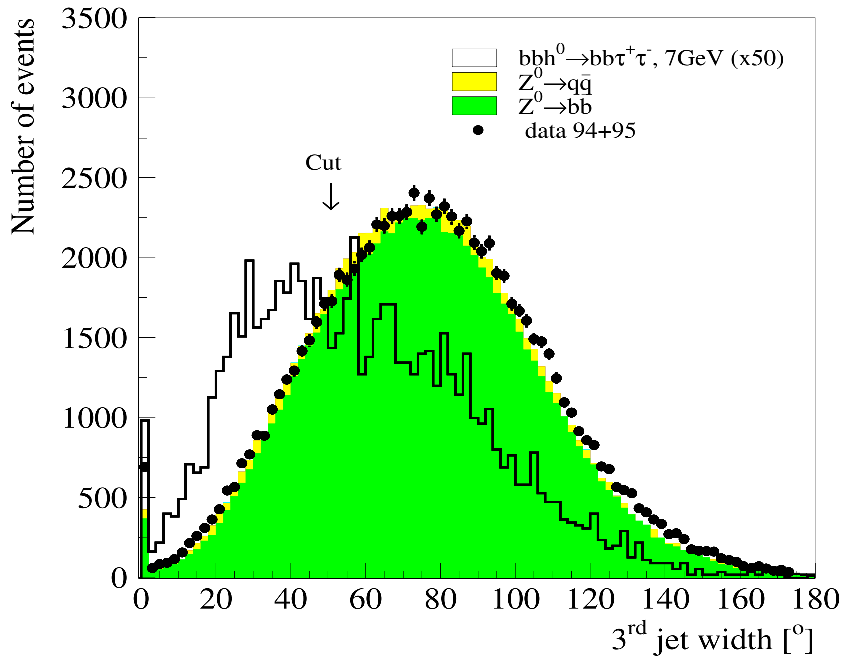

Figure 5.18: 3^{rd} jet width, treated as angular distance between two most distant tracks in the jet (see description in the text), after the cuts concerning x_{b1}, x_{b2} and cosα_{12} variables. The dots represent data. Only two main kinds of background are shown (histograms) – other background processes give small contribution and are not visible. Black line represents typical h^0 Higgs boson signal (m$_{h^0}$ = 7 GeV/c^2), scaled by a factor of 50 to show its shape. The arrow indicates the cut described in the text – events on the right side of the arrow are rejected.

achieved by "removing" the lepton from the jet and taking its p_T value as of external particle in relation to "reduced" 3^{rd} jet (Figure 5.19).

The sum of the total momenta $p_{tot1} + p_{tot2}$ of the two tracks with the highest momentum over the measured energy in the 3^{rd} jet, E$_3$ was expected to be greater than 0.5 (Figure 5.20).

After all described cuts 7 events remained in the data when 10.53±2.34 events were expected, of which 10.06±2.33 are $q\bar{q}$ events, 0.42±0.15 come from $\ell\ell q\bar{q}$ ($\ell = e,\ \mu$) and 0.05±0.02 from $\tau^+\tau^-q\bar{q}$ process. The final signal efficiencies for the Higgs bosons in the $b\bar{b}\tau^+\tau^-$ analysis are shown in Table 5.7.

Example events that passed the described analysis selection criteria, for MC signal simulation (A^0 Higgs boson, m$_{A^0}$ = 7 GeV/c^2) and real data are displayed in Figures 5.21 and 5.22 respectively.

5.3.3 Systematic errors

The method of systematic errors evaluation used for the $b\bar{b}\tau^+\tau^-$ final state was the same as described in Section 5.2. Systematic errors for the present analysis, for MC simulations and for A^0 and h^0 signals are given in Table 5.8.

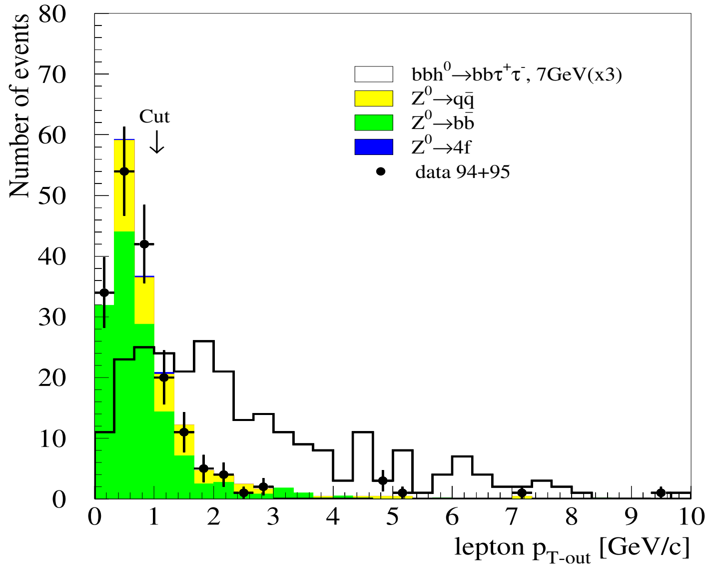

Figure 5.19: Identified lepton p_{T-out} in the 3^{rd} jet, after cuts described in the text. The dots represent data, histograms – different background processes. Black line represents typical h^0 Higgs boson signal (m_{h^0} = 7 GeV/c^2), scaled by a factor of 3 in order to show its shape. The arrow indicates the cut described in the text – events on the left side of the arrow are rejected.

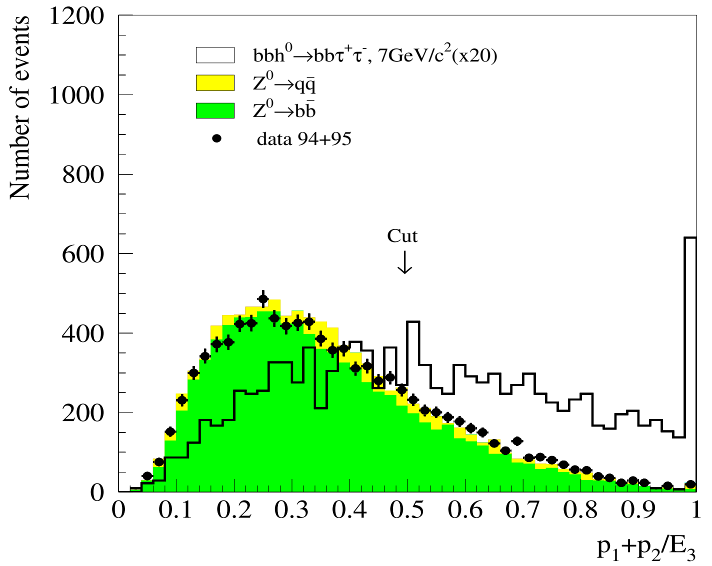

Figure 5.20: The sum of the total momenta $p_{tot1} + p_{tot2}$ of the two tracks with the highest momentum over the measured energy in the 3^{rd} jet, E$_3$, after cuts described in the text. The dots represent data, histograms – different background processes. Black line represents typical h^0 Higgs boson signal (m_{h^0} = 7 GeV/c^2), scaled by a factor of 20 in order to show its shape. The arrow indicates the cut described in the text – events on the left side of the arrow are rejected.

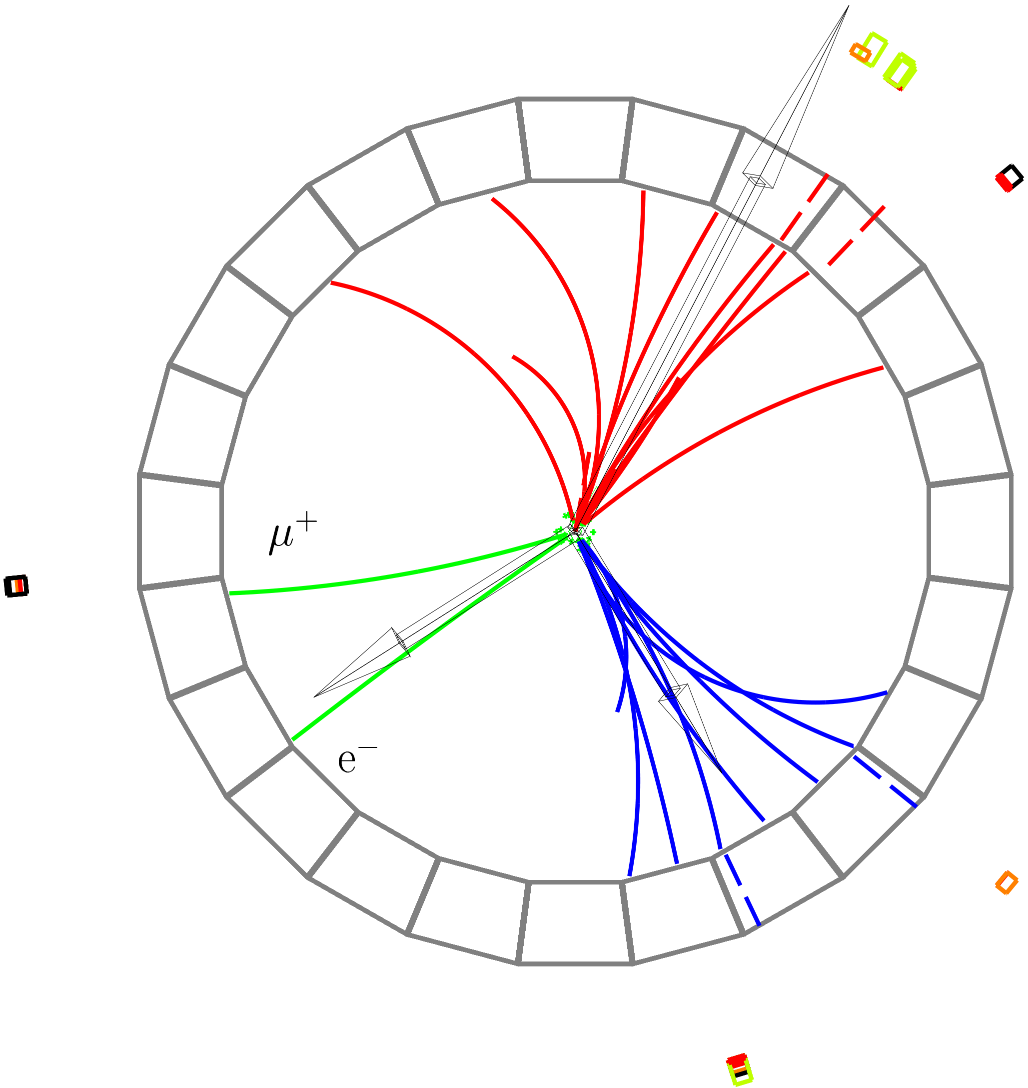

Figure 5.21: Typical Higgs boson (here: A^0, m$_{A^0}$ = 7 GeV/c^2) simulated event of the $b\bar{b}\tau^+\tau^-$ final state, seen in DELPHI detector. The event satisfies all selection criteria described in the text. Three jet in the event were reconstructed: they are displayed with different colors. Arrows represent jet momenta. Jet b-tagging values were found to be x$_{b1}$ = 2.51 for the red jet, x$_{b2}$ = 1.28 for the blue jet and x$_{b3}$ = 0.03 for the green jet. The latter consists of two leptons: e$^-$ (p$_{e^-}$ = 15.6 GeV/c) and μ^+ (p$_{\mu^+}$ = 2.9 GeV/c). Dashed lines represent neutral particles. Barrel electromagnetic calorimeter is displayed in grey, in order to show the orientation of the display – see the detector schematic view and description in Chapter 3. Color cuboids represent energy deposits in the hadron calorimeter (not displayed here for legibility).

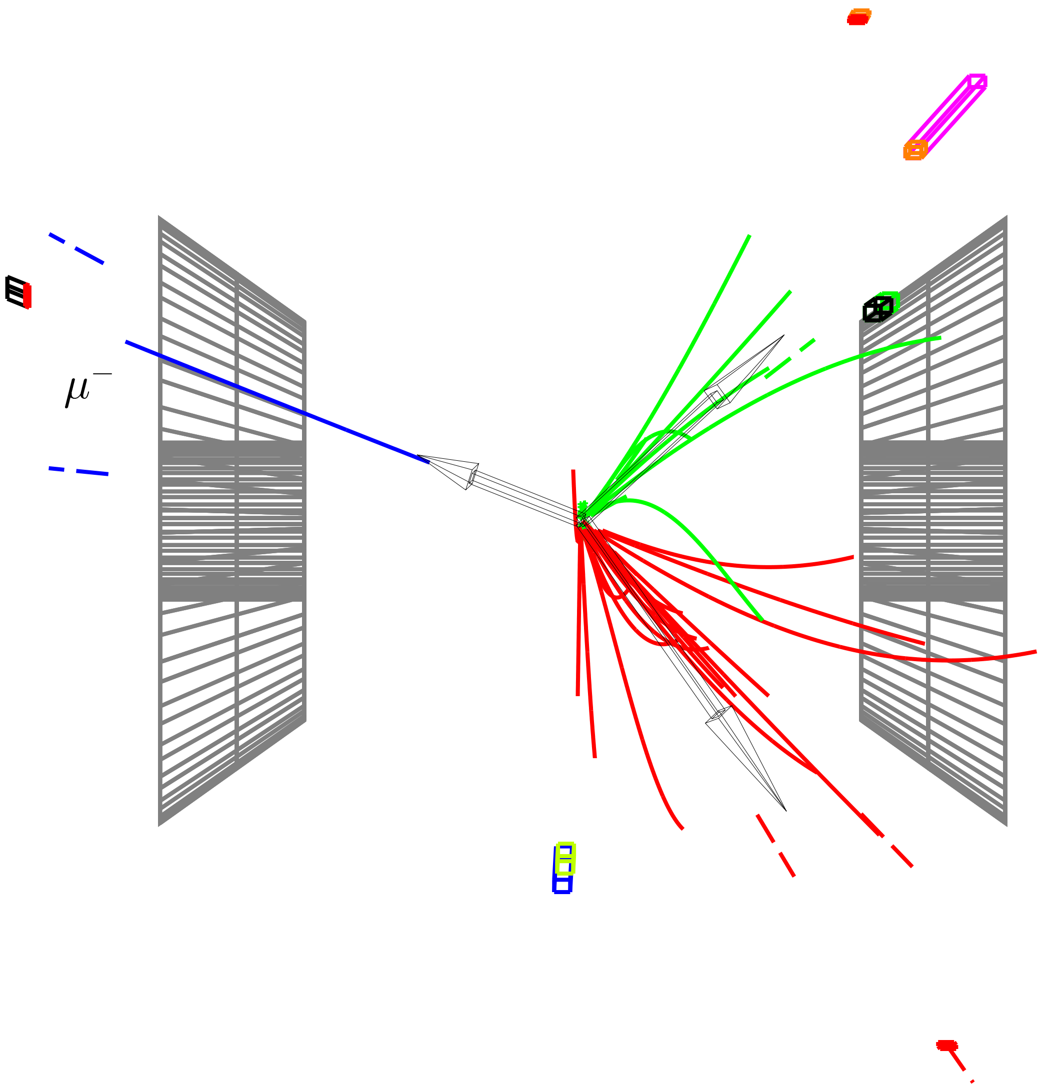

Figure 5.22: Real data event of the $b\bar{b}\tau^+\tau^-$ final state, seen in DELPHI detector. The event satisfies all selection criteria described in the text. Three jet in the event were reconstructed: they are displayed with different colors. Arrows represent jet momenta. Jet b-tagging values were found to be x_{b1} = 1.10 for the green jet, x_{b2} = -0.69 for the red jet and x_{b3} = -0.83 for the blue jet. The latter consists of one lepton: μ^- (p_{μ^-} = 9.2 GeV/c). Dashed lines represent neutral particles. Forward RICH detector is displayed in grey, in order to show the orientation of the display – see the detector schematic view and description in Chapter 3. Color cuboids represent energy deposits in the hadron calorimeter (not displayed here for legibility).

Table 5.7: Final signal efficiencies for A^0 and h^0 Higgs bosons in the analysis of $b\bar{b}\tau^+\tau^-$ final state.

Higgs boson mass (GeV/c^2)	h^0 efficiency (%)	A^0 efficiency (%)
4.1	0.80±0.09	1.03±0.10
7.0	1.12±0.11	1.43±1.12
9.5	1.27±0.11	1.78±0.13
10.0	1.48±0.12	1.76±0.13
12.0	1.58±0.13	1.65±0.13

Table 5.8: Evaluation of systematic errors on efficiency in $2b2\tau$ analysis.

	syst. error (%)
'94 + '95 MC	11.97
h^0 signal, m$_{h^0}$ = 4.1 GeV/c^2	4.68
7.0 GeV/c^2	4.84
9.5 GeV/c^2	5.03
10.0 GeV/c^2	5.06
12.0 GeV/c^2	5.16
A^0 signal, m$_{A^0}$ = 4.1 GeV/c^2	5.35
7.0 GeV/c^2	5.27
9.5 GeV/c^2	5.27
10.0 GeV/c^2	5.25
12.0 GeV/c^2	5.32

5.4 Search in the $b\bar{b}b\bar{b}$ topology

In the $b\bar{b}b\bar{b}$ ($4b$) topology, the Higgs boson is radiated off b or $\bar{b}$ quark:

$$e^+e^- \to Z^0 \to b\bar{b}h^0, \text{ or } e^+e^- \to Z^0 \to b\bar{b}A^0,$$

and decays into $b\bar{b}$ pair. Higgs bosons of mass close to the $b\bar{b}$ threshold will produce a single jet, containing both b quarks that may be glued to one of the b jets created from the Z^0 decay. This may cause 3, or even 2-jet topology. For heavier Higgs bosons, of mass of about half of the Z^0 mass one expects a 4-jet topology. Taking this into account, two selections were developed, corresponding to 3- and 4-jet event reconstructions respectively.

First analysis in this final state [35] was based on a reinterpretation of DELPHI measurement of gluon splitting into $b\bar{b}$ [50]. The gluon splitting, present in Z decays to b-quarks, induces an irreducible background to Yukawa production of light Higgs bosons in the $4b$ topology. The Feynman diagram for this kind of background is presented in Figure 5.15. Analysis in this topology was not performed by the author of this thesis and is described in detail in [38].

5.4.1 The event selection

The events are required to contain at least 6 charged particles. At this stage all events were reconstructed in 3-jet topology. The 2→3 jet resolution parameter y_{23} of DURHAM algorithm [48] should be greater than 0.01. For all reconstructed jets, the b-tagging values x_{bi} are computed and ordered from higher to lower b-likeness. The b-tagging variable value of the most b-tagged jet, x_{b1}, is required to be greater than 0.

The preselection eliminates all kinds of background except of hadronic decays of Z^0. Non-b hadronic events are reduced as well. After this step, all events are reconstructed as 3-jet events and 4-jet events in turn.

The final selection relies on the least tagged jets, i.e. on the x_{b3} variable value in the 3-jet topology and on the sum $x_{b34} = x_{b3} + x_{b4}$ in the 4-jet topology. Figure 5.23 displays the distributions of these variables. In the Monte Carlo simulation a gluon splitting constant fixed to $g_{b\bar{b}}$=1.5×10^{-3} was used. This value is about a factor 2 lower than current world average, whereas the central value of the theoretical evaluation is $g_{b\bar{b}}=1.8^{+0.4}_{-0.5}\times10^{-3}$ [51]. A fit to the $b\bar{b}$ and $b\bar{b}g \to b\bar{b}b\bar{b}$ components of the data was performed and also displayed in Figure 5.23. The fit to data shows that the value of the gluon splitting contribution is larger than used in the simulation. The value of the fit gives $g_{b\bar{b}}=(4.5\pm0.7)\times10^{-3}$ for 3-jet reconstruction, and $g_{b\bar{b}}=(4.7\pm0.7)\times10^{-3}$ for 4-jet reconstruction [38]. The DELPHI measurement of this constant [50] gives $g_{b\bar{b}}=(3.3\pm1.0(\text{stat})\pm0.8(\text{syst}))\times10^{-3}$. Because of large uncertainties that affect the gluon splitting measurements, the value coming from the fit was conservatively not taken into account for background estimation.

In both 3-jet and 4-jet analyses, two channels were defined for the final analysis. The channels are denoted "bin 1" (for 1.25< x_{b3} <1.5 in the 3-jet analysis and for 0.55< x_{b34} <1.0 in the 4-jet analysis) and "bin 2" (for 1.5< x_{b3} in the 3-jet analysis and for 1.0< x_{b3} in the 4-jet analysis), and are shown in Figure 5.23. They were chosen to have a similar expected background, and at least 1-2% efficiency in "bin 2" for signal events. Numbers of expected and observed events in the bins defined above are given in Table 5.9.

Table 5.9: Number of observed events and expected background in the Yukawa $b\bar{b}b\bar{b}$ analysis.

			$q\bar{q}$ bkg.	data (94-95)
3-jet topology:	bin1	1.25< x_{b3} <1.5	2.2 ± 0.9	5
	bin2	1.5< x_{b3}	3.2 ± 1.1	5
4-jet topology:	bin1	0.55< x_{b34} <1.0	3.4 ± 1.1	7
	bin2	1.0< x_{b3}	3.5 ± 1.0	4

Estimation of the systematic uncertainty related to the residual differences between b-tagging efficiency in data and in the simulation was based on studies presented in DELPHI paper [49], where it was shown that a 10% difference is a conservative upper bound in the case of high b-jet selection purity (Figure 20 of [49]). This uncertainty was assumed and added in quadrature to the statistical uncertainty from the limited size of simulation samples.

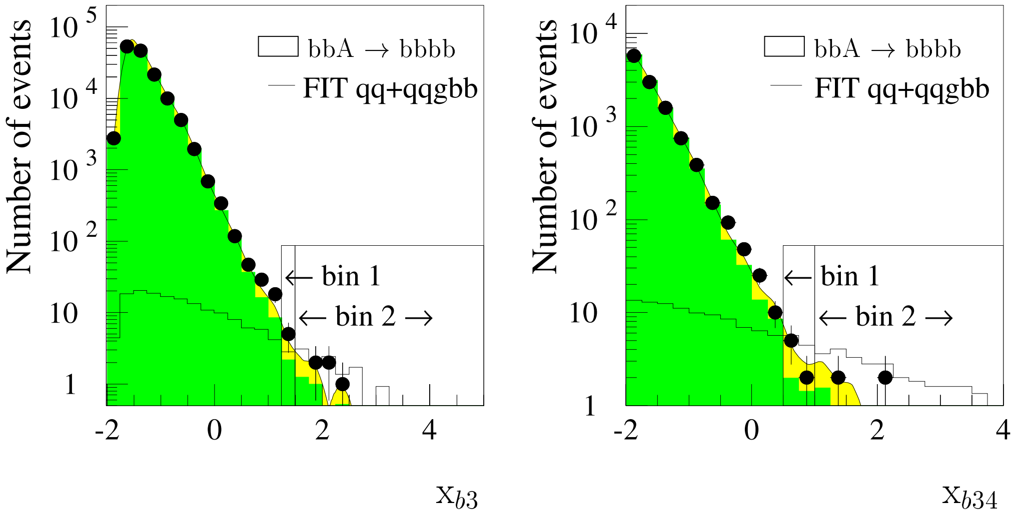

Figure 5.23: Data to simulation comparison for two relevant variables, used in the Yukawa $b\bar{b}b\bar{b}$ analysis. Dark histogram represents the Standard Model $q\bar{q}$ background with $g_{b\bar{b}}$=1.5×10^{-3}. Dots represent data. A fit to data is displayed (curve with yellow shadow underneath) – see text. The non-shaded histogram represents typical A^0 Higgs boson signal variables distribution (m$_{A^0}$ = 40 GeV/c^2), scaled arbitrary in order to show its shape. Boxes denoted "bin1" and "bin2" indicate cuts described in the text – only events in the drawn boxes were accepted.

Selection efficiencies for Yukawa production of A and h bosons are shown in Table 5.10. The 3-jet analysis in general performs better than the 4-jet one for small Higgs boson masses; consequently it was used for Higgs masses up to 12 GeV/c^2. The 4-jet analysis was used for higher masses.

Example events that passed the described analysis selection criteria, for MC signal simulation (h^0 Higgs boson, m$_{h^0}$ = 40 GeV/c^2) and real data are displayed in Figures 5.24 and 5.25 respectively.

Table 5.10: Final signal efficiencies for A^0 and h^0 Higgs bosons in the analysis of $b\bar{b}b\bar{b}$ final state.

mass (GeV/c^2)	3-jet efficiency (%)		4-jet efficiency (%)	
	bin 1	bin 2	bin 1	bin 2
m$_h$=11	0.5 ± 0.1	1.2 ± 0.2	0.4 ± 0.1	0.5 ± 0.1
13	0.6 ± 0.1	0.7 ± 0.1	0.7 ± 0.1	0.4 ± 0.1
15	0.4 ± 0.1	0.8 ± 0.1	0.9 ± 0.1	1.1 ± 0.1
20	0.5 ± 0.1	1.0 ± 0.1	1.1 ± 0.2	1.5 ± 0.2
30	0.7 ± 0.1	1.2 ± 0.2	1.8 ± 0.2	2.1 ± 0.2
40	0.6 ± 0.1	1.5 ± 0.2	1.8 ± 0.2	2.4 ± 0.2
50	0.6 ± 0.1	0.9 ± 0.1	1.3 ± 0.2	1.8 ± 0.2
60	0.3 ± 0.1	0.7 ± 0.1	1.0 ± 0.1	1.0 ± 0.1
70	0.4 ± 0.1	0.5 ± 0.1	0.3 ± 0.1	0.3 ± 0.1
m$_A$=11	0.6 ± 0.1	1.4 ± 0.2	0.9 ± 0.1	0.5 ± 0.1
13	0.5 ± 0.1	1.3 ± 0.2	0.8 ± 0.1	0.7 ± 0.1
15	0.5 ± 0.1	1.0 ± 0.1	1.1 ± 0.2	1.3 ± 0.2
20	0.5 ± 0.1	1.1 ± 0.2	1.4 ± 0.2	1.8 ± 0.2
30	0.5 ± 0.1	1.3 ± 0.2	1.7 ± 0.2	2.2 ± 0.2
40	0.4 ± 0.1	1.5 ± 0.2	1.8 ± 0.2	2.2 ± 0.2
50	0.5 ± 0.1	1.1 ± 0.1	1.7 ± 0.2	1.8 ± 0.2
60	0.4 ± 0.1	1.0 ± 0.1	0.8 ± 0.1	1.2 ± 0.2
70	0.1 ± 0.1	0.4 ± 0.1	0.2 ± 0.1	0.2 ± 0.1

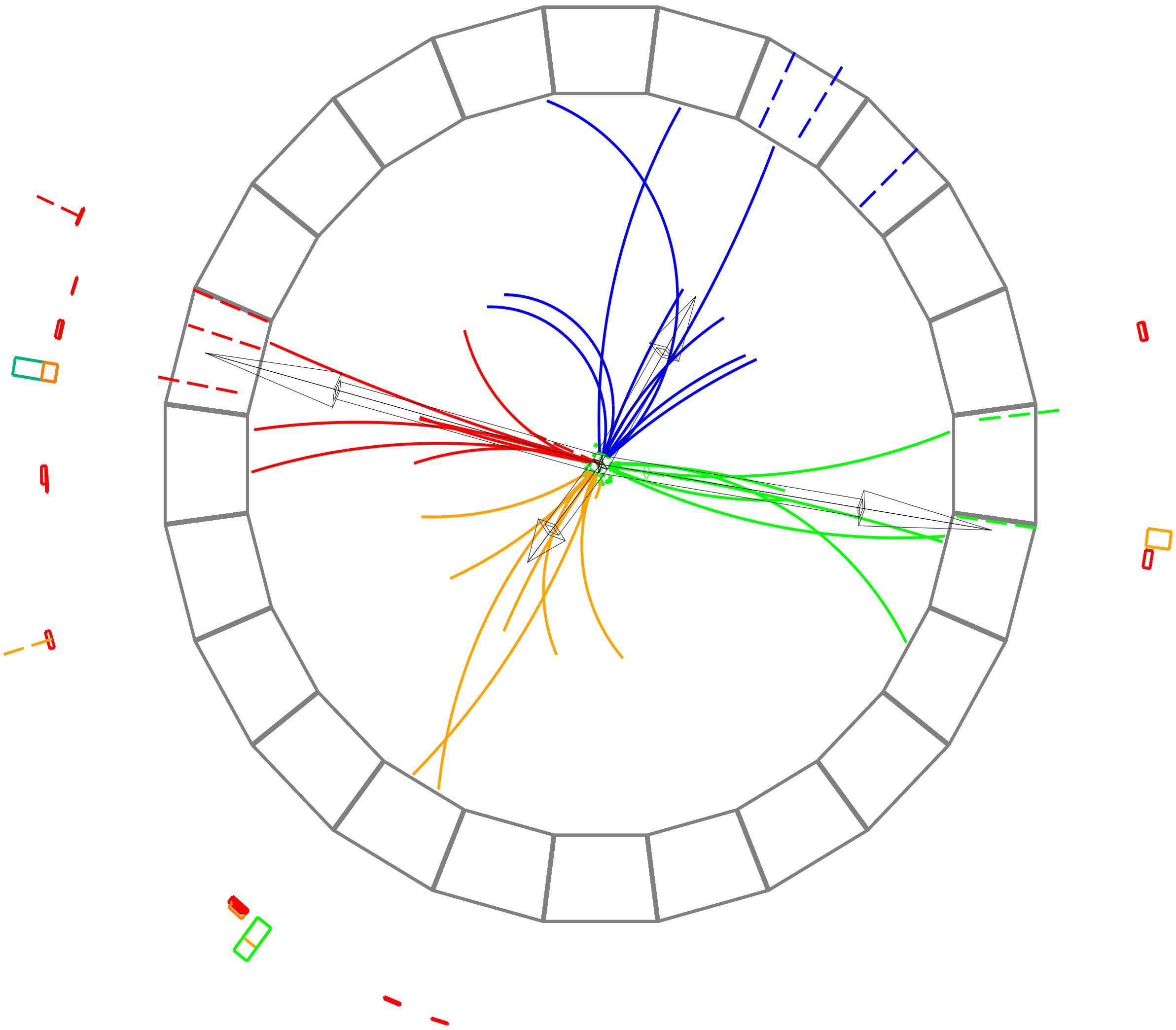

Figure 5.24: Typical Higgs boson (here: h^0, m_{h^0} = 40 GeV/c^2) simulated event of the $b\bar{b}b\bar{b}$ final state, seen in DELPHI detector. The event satisfies all selection criteria described in the text. Four jets in the event were reconstructed: they are displayed with different colors. Arrows represent jet momenta. Jet b-tagging values were found to be x_{b1} = 2.22 for the green jet, x_{b2} = 1.36 for the orange jet, x_{b3} = 1.17 for the red jet and x_{b4} = 0.45 for the blue jet. Dashed lines represent neutral particles. Barrel electromagnetic calorimeter is displayed in grey, in order to show the orientation of the display – see the detector schematic view and description in Chapter 3. Color cuboids represent energy deposits in the hadron calorimeter (not displayed here for legibility)

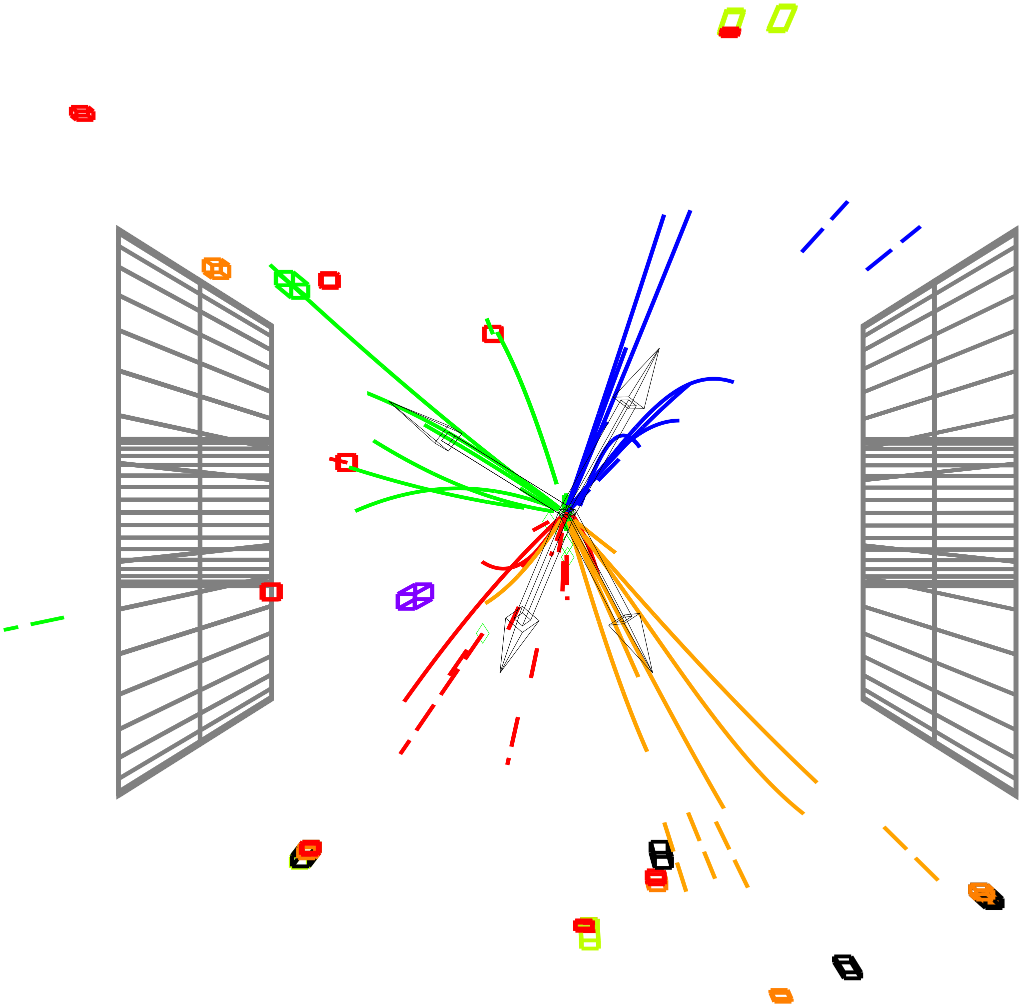

Figure 5.25: Real data event of the $b\bar{b}b\bar{b}$ final state, seen in DELPHI detector. The event satisfies all selection criteria described in the text. Four jets in the event were reconstructed: they are displayed with different colors. Arrows represent jet momenta. Jet b-tagging values were found to be $x_{b1} = 1.84$ for the red jet, $x_{b2} = 1.72$ for the orange jet, $x_{b3} = 0.73$ for the blue jet and $x_{b4} = 0.48$ for the green jet. Dashed lines represent neutral particles. Forward RICH detector is displayed in grey, in order to show the orientation of the display – see the detector schematic view and description in Chapter 3. Color cuboids represent energy deposits in the hadron calorimeter (not displayed here for legibility).

Chapter 6

Results

In this chapter results in the form of mass-dependent upper bounds on coupling factors as functions of the involved Higgs boson masses are presented. Non observation of the excess in data in considered channels allows to evaluate upper bounds on parameter values of the model.

As it was said in Section 4.3 the Yukawa process is available either in 1HDM and 2HDM. In both models the cross-section for the Yukawa process is suppressed by a factor $(m_f/m_W)^2$ in comparison to the Bjorken process, but in case of 2HDM model it can be enhanced by $\tan^2\beta$ factor. Thus, in the 1HDM model, the cross section is too small and the Yukawa process can not be observed at LEP energies. The final state cross section for the Yukawa process in the 2HDM(II) can be expressed in terms of the Standard Model Yukawa cross section and enhancement factor arising from mixing of the Higgs doublets and branching fractions. For h^0 production:

$$\begin{aligned}
\sigma_{\tau^+\tau^- h\to 4\tau} &= \sigma^{SM}_{\tau^+\tau^- H} \times R^2_{\tau^+\tau^- h} \times BR(h\to\tau^+\tau^-) \\
\sigma_{b\bar{b}h\to 2b2\tau} &= \sigma^{SM}_{b\bar{b}H} \times R^2_{b\bar{b}h} \times BR(h\to\tau^+\tau^-) \\
\sigma_{b\bar{b}h\to 4b} &= \sigma^{SM}_{b\bar{b}H} \times R^2_{b\bar{b}h} \times BR(h\to b\bar{b})
\end{aligned}$$

and for A^0:

$$\begin{aligned}
\sigma_{\tau^+\tau^- A\to 4\tau} &= \sigma^{SM}_{\tau^+\tau^- H} \times R^2_{\tau^+\tau^- A} \times BR(A\to\tau^+\tau^-) \\
\sigma_{b\bar{b}A\to 2b2\tau} &= \sigma^{SM}_{b\bar{b}H} \times R^2_{b\bar{b}A} \times BR(A\to\tau^+\tau^-) \\
\sigma_{b\bar{b}A\to 4b} &= \sigma^{SM}_{b\bar{b}H} \times R^2_{b\bar{b}A} \times BR(A\to b\bar{b})
\end{aligned}$$

The vertex enhancement factors $R^2_{f\bar{f}h}$ and $R^2_{f\bar{f}A}$ (where f is b or τ) are $|\sin\alpha/\cos\beta|^2$ and $\tan^2\beta$, respectively.

The analysis has been done for $\tan\beta = 30$. The maximal number of signal events that corresponds to 95% CL (see Appendix C) – μ_{max} was counted for each mass point in the analysis and each final state. This allows to extract excluded enhancement factor as:

$$\sigma = \sigma^{SM} \times R^2 \times BR$$

for every process. The excluded enhancement factor R can be found from:

The enhancement factor R and the number of events can be connected as follows:

$$\sigma \cdot BR \cdot R^2_{excl} = \frac{\mu_{max}}{\epsilon \cdot \mathcal{L}} \qquad \text{and} \qquad \sigma \cdot BR \cdot R^2 = \frac{N_{exp}}{\epsilon \cdot \mathcal{L}} \tag{6.1}$$

where ϵ is analysis final efficiency and $\mathcal{L}$ is luminosity. N_{exp} is expected number of signal events from MC simulations. Reference cross-sections for Yukawa production of A^0 and h^0 were obtained using program formulae described in publication by M. Krawczyk and J. Kalinowski [43]. Using expressions 6.1, one can write:

$$\mu_{max}/R^2_{excl} = N_{exp}/R^2 \tag{6.2}$$

The analysis has been done for tan$\beta = 30$. The excluded enhancement factor can be expressed as:

$$R_{excl} = 30 \times \sqrt{\frac{\mu_{max}}{N_{exp}}} \tag{6.3}$$

In all analysed final states (4τ, $2b2\tau$, $4b$), a certain number n of data events was found and compared to the expected background value b. For these values corresponding maximal signal number of events at 95% confidence level was computed. Then, using 6.3, maximal R factor was achieved. The procedure was applied to all masses, considered in the analyses. Factors R_{excl} achieved for every Higgs boson mass, are presented on the ($m_{A/h}$, R) plane in Figures 6.1, 6.2 and 6.3 separately for legibility, and superimposed in Figure 6.4 for comparison.

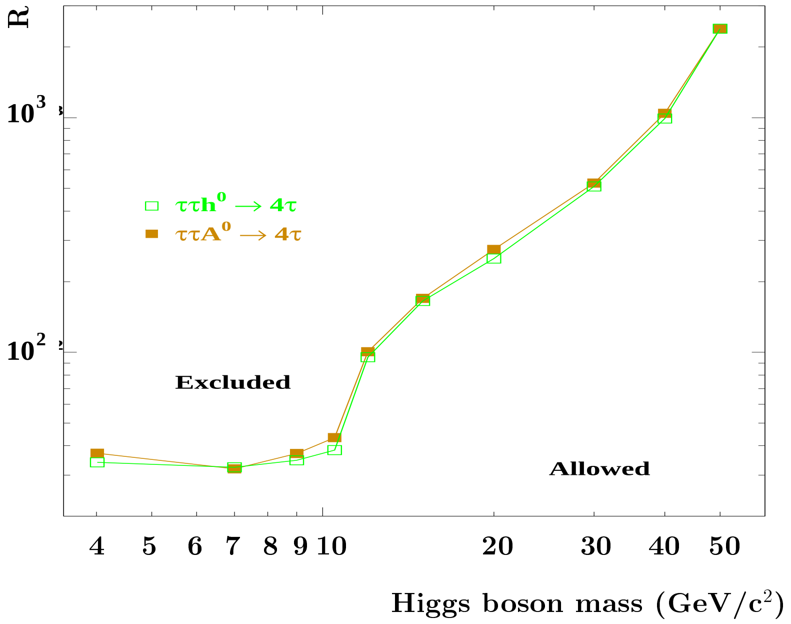

Figure 6.1: The exclusion within 2HDM type II on the ($m_{A/h}$, R) plane for 4τ final state in the Yukawa process. R stands for tanβ and sinβ/cosα for A^0 and h^0 Higgs bosons respectively. The exclusions are given at 95% confidence level. The excluded region is above plotted curves.

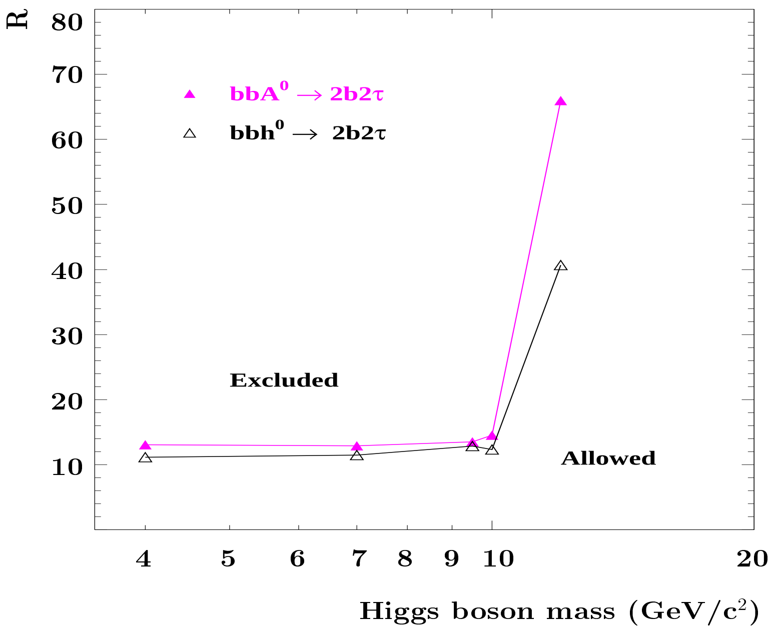

Figure 6.2: The exclusion within 2HDM type II on the ($m_{A/h}$, R) plane for $2b2\tau$ final state in the Yukawa process. R stands for tanβ and sinβ/cosα for A^0 and h^0 Higgs bosons respectively. The exclusions are given at 95% confidence level. The excluded region is above plotted curves.

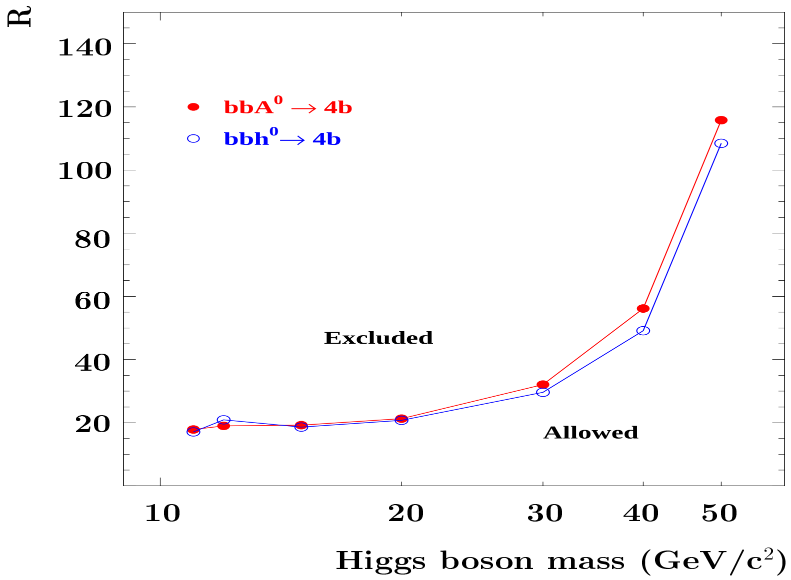

Figure 6.3: The exclusion within 2HDM type II on the ($m_{A/h}$, R) plane for $4b$ final state in the Yukawa process. R stands for tanβ and sinβ/cosα for A^0 and h^0 Higgs bosons respectively. The exclusions are given at 95% confidence level. The excluded region is above plotted curves.

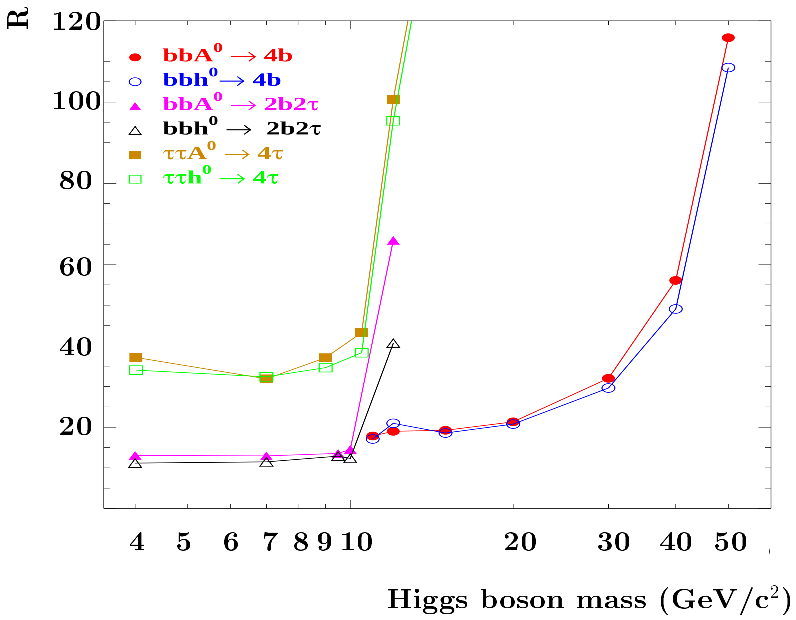

Figure 6.4: The exclusion within 2HDM type II on the ($m_{A/h}$, R) plane for 4τ, $2b2\tau$ and $4b$ final states in the Yukawa process. R stands for tanβ and sinβ/cosα for A^0 and h^0 Higgs bosons respectively. The exclusions for all analyses are superimposed for comparison. The exclusions are given at 95% confidence level. The excluded region is above plotted curves.

Chapter 7

Summary

In this thesis an analysis of the e^+e^- collisions, produced by the Large Electron Positron collider at CERN with center-of-mass energies at Z^0 peak and around is presented. The data was recorded by DELPHI detector and corresponds to the total integrated luminosity of $\sim$80 pb^{-1}.

The main goal of this thesis is to search for the possible presence of interactions (events) that can be attributed to Higgs boson (or bosons) production in the minimal extension of the Standard Model, the so called Two Higgs Doublet Model (2HDM). This particle is a crucial ingredient of the model that describes the world of elementary particles. It not only explains how particles acquire mass, but in addition ensures precise predictions for their interactions. Although the mass of the Higgs boson is not predicted, its properties are. Within the 2HDM, for a sufficiently small $\sin^2(\beta-\alpha)$, the h^0 boson produced through the Higgsstrahlung process cannot be seen in the data collected at LEP due to the cross-section suppression factor. Associated production, if kinematically allowed, would be dominant process for Higgs boson production. On the other hand a light Higgs boson which is produced only in the Yukawa process (for a light A^0 or light h^0) could have escaped discovery. Under the assumption that the Higgsstrahlung process is suppressed and the pair production is kinematically forbidden, $m_{A^0} + m_{h^0} > \sqrt{s}$, the Yukawa process becomes the dominant process for Higgs production at LEP.

In the thesis a search for light Higgs bosons in the Yukawa process is presented. Three different final states were considered for Higgs boson masses varying from 4 to 70 GeV/c^2: $4b$, $2b2\tau$ and 4τ.

For each of the final states a sequential series of cuts have been applied in order to reduce background. The final efficiencies for the signal samples varied for different final states and were 3.02% to 6.52% in the four-prong and 2.93% to 5.64% in the six-prong $\tau^+\tau^-\tau^+\tau^-$ final state, 0.8% to 1.78% in the $b\bar{b}\tau^+\tau^-$ final state and 0.1% to 2.4% for the $b\bar{b}b\bar{b}$ final state, depending on the mass of the Higgs boson.

The search for the light neutral Higgs bosons is summarized in presented exclusions of the enhancement parameter $\tan\beta$ for A^0 and $\sin\alpha/\cos\beta$ for h^0 Higgs boson as a function of the mass of the particles. The exclusions are given at 95% confidence level.

For the 4τ final state the exclusion of the enhancement factor R is$\simeq$31, if the mass of the

Higgs boson is 4 GeV/c^2, for the $2b2\tau$ R$\simeq$10 for the mass of 4 GeV/c^2 and in the $4b$ final state R$\simeq$17 for the mass of 12 GeV/c^2.

As the LEP experiments can not claim to have observed the Higgs boson, the search for this elusive particle continues. With the new proton–(anti-)proton colliders at Fermilab and CERN it is very likely that, if the Higgs boson (bosons) exists, it will be discovered in the coming years.

It is also possible that there will be no Higgs–like particle at all. This would destroy the theory of giving mass to the vector bosons but would not be in contradiction to experimental results. Different models without any Higgs boson would reveal an excess in the WW scattering that would imply the existence of alternative to the Higgs sector source of symmetry breaking [52, 53].

Appendix A

Jet clustering procedure

Primary quarks and gluons that are produced in the interaction are identified as groups of particles in the detector. To obtain the best estimate of the energy and momentum of each parton the goal is to cluster all particles originating from the same parton fragmentation. At the end of clustering the remaining groups of particles are called jets and their 4-momentum (the sum of the momenta of all particles assigned to the jet) is used as an estimate of the parameters of the primary parton. In this section a general introduction on clustering algorithms is given followed by a short discussion on the DURHAM algorithm, which is the algorithm used throughout the thesis. A detailed discussion on the subject is given in [39].

Most clustering procedures can be characterized by three definitions:

- **A distance (y_{ij}):** a measure that defines, how far in space two particles i and j are apart. The measure is used to decide, which two particles should be considered to be combined first.

- **A maximum distance (y_{cut}):** a resolution parameter defining the maximum distance for which two particles can be combined. The clustering procedure is ended, when $y_{ij} > y_{cut}$ or required number of clusters is reached.

- **A recombination scheme:** a prescription of how to construct the 4-momentum of the object that is formed after two particles combination.

In order to cluster particles into jets most algorithms follow a similar procedure: iterative procedures starting for each event with all (n) measured energy flow objects (particles). In this case every final-state particle is initially considered as a cluster. For each pair of these final-state particles ($i,\ j$) their separation is calculated using the algorithm specific distance definition. In the next step of the procedure the two particles ($i,\ j$) with the smallest value of y_{ij} are combined and replaced by a 'pseudo-particle' with 4-momentum p^{μ}_{ij} using a recombination scheme. This clustering is performed only if y_{ij} is smaller than the maximum distance parameter y_{cut}. After clustering particles i and j the event now consists of $n-1$ clusters and again all distances between particles are calculated. The procedure is repeated until all pairs of particles satisfy the condition $y_{ij} > y_{cut}$, or until a demanded number of clusters is reached. Cluster of particles that remain at this stage are called jets. For a given value of y_{cut} the event is characterized by the number of reconstructed jets.

The simplest choice for a distance measure for two clusters i and j is to use squared invariant mass[1]:

$$m_{ij}^2 = (E_i + E_j)^2 - (\mathbf{p}_i + \mathbf{p}_j)^2 \tag{A.1}$$

This measure has, in fact, some instability problems. With it, particles tend to cluster first in the region of small momenta particles. The clustering starts therefore in the centre of the event, and subsequantly spread outwards to enclose eventually the fast particles. The invariant mass measure will then tend to cluster fast particles around the slow ones, while the former should better represent the jet direction and slow particles should be clustered around fast ones.

In order to achieve jets around high momenta particles one uses other distance measures. In the LUCLUS [39] algorithm a jet is defined as a collection of particles that have a limited transverse momentum with respect to a common jet axis, and hence with respest to each other. A distance measure d_{ij} between two particles, or clusters depends only on the relative transverse momentum:

$$d_{ij}^2 = 4\frac{|\mathbf{p}_i|^2|\mathbf{p}_j|^2\sin^2(\theta_{ij}/2)}{(|\mathbf{p}_i| + |\mathbf{p}_j|)^2} \tag{A.2}$$

where $\mathbf{p}_i$ and $\mathbf{p}_j$ are i and j particles (clusters) momenta. If the relative angle, θ_{ij} is small, this measure reduces to

$$d_{ij}^2 \approx \frac{|\mathbf{p}_i \times \mathbf{p}_j|}{|\mathbf{p}_i + \mathbf{p}_j|} \tag{A.3}$$

In this limit the measure d_{ij}^2 is treated as the transverse momentum of particles with respect to the direction given by the sum of the two particle momenta.

Another alternative is to replace the distance measure described above with one used in the JADE [39] algorithm. The distance measure y_{ij} is defined by

$$y_{ij} = \frac{2E_iE_j(1 - \cos\theta_{ij})}{E_{vis}^2} \tag{A.4}$$

where θ_{ij} is the relative angle between i and j objects, and E_{vis} is the total visible energy of the event. The usage of E_{vis}^2 in the denominator makes the measure less sensitive to detector acceptance corrections and allows compare results at different center-of-mass energies.

[1]Equivalently, one could have used the invariant mass as measure.

If $m_i = m_j = 0$ the y_{ij} measure is just normalised squared mass. The JADE clustering algorithm has some characteristics that cause problems in certain classes of events, since two low-energetic clusters will be combined, even when they have a large opening angle. In events containing many of low-energetic clusters these can form a 'phantom' jet leading to an unnatural assignment of particles to jets. To overcome these problems, other algorithms were developed that were less sensitive to soft gluon emission, like the DURHAM algorithm.

The DURHAM algorithm [48] is the most widely used algorithm in multi-jet final states at LEP. It is closely related to the JADE algorithm, but does not suffer from the problems mentioned above by adopting a slightly different distance definition:

$$\tilde{y}_{ij} = \frac{2\min(E_i, E_j)(1 - \cos\theta_{ij})}{E_{cms}^2} \tag{A.5}$$

The measure has the geometrical interpretation as the transverse momentum of the softer patricle with respect to the direction of the harder one. The distance is again normalised to the total visible energy in the event and has the advantage compared to the original JADE distance that is assigns low-energy particles to their closest high-energy jet first and it's therefore better behaved.

Another advantage of this clustering algorithm is the fact that the hadronisation of the parton final states can be shown to have, on average, little influence on the jet-rates. This can be evaluated on generator level by studying the differences between parton and hadron level. Although there is no "best" clustering algorithm, because every one has specific qualities and problems, in multi-jet events at LEP the DURHAM clustering algorithm is generally accepted as one of the best in reconstructing the energy flow of the original partons and is therefore used in this thesis.

Appendix B

B-tagging in DELPHI

B-hadrons are formed in the hadronization of the b-quarks and have distinct properties allowing jets of particles to be identified (tagged) as coming from the fragmentation of a b-quark.

For high purity and efficiency b-quark events selection a special method had been developed. Variable x_b describes, to some extent, probability that a jet or an event contains b-quark(s). It is a combination of various variables, characteristic of B mesons (mass, lifetime, secondary vertices, impact parameters, etc.). A detailed description of the b-tagging combined variable construction and use can be found in the devoted publication [49].

B.1 Method of combined variables

For a combined tagging variable y, the likelihood ratio method is defined as:

$$y = \frac{f^{bkg}(x_1 \ ,..., \ x_n)}{f^{sig}(x_1 \ ,..., \ x_n)} \tag{B.1}$$

where $f^{bkg}(x_1 \ ,..., \ x_n)$ and $f^{sig}(x_1 \ ,..., \ x_n)$ are probability density functions of the variables $x_1 \ ,..., \ x_n$ for the background and signal respectively. The selection of all events of $y_0 > y$ gives the optimal tagging of the signal.

For $n > 2$ independent variables[1] expression B.1 becomes

$$y = \prod_{i=1}^{n} \frac{f_i^{bkg}(x_i)}{f_i^{sig}(x_i)} = \prod_{i=1}^{n} y_i \tag{B.2}$$

$$y_i = \frac{f_i^{bkg}(x_i)}{f_i^{sig}(x_i)} \tag{B.3}$$

where $f_i^{bkg}(x_i)$ and $f_i^{sig}(x_i)$ are probability density functions of each individual variable x_i for the background and signal respectively, and are determined from simulation.

[1] Variables are independent if, for the signal and for each separately treated background component, the distribution of one variable is independent of any selection on the others.

Such a method is used in DELPHI for combined b-tagging construction. The discriminating variables are not independent, but are chosen such that the correlations between them are small enough to ensure the resulting tagging is very close to optimal.

B.1.1 Jet b-tagging

In DELPHI all discriminating variables and the b-tagging can be computed independently for each jet in an event. All tracks are assumed to originate from fragmentation of the b-quark or from the decay of the B-hadron. There are two background types for the b-quark selection – jets generated by c-quarks and by light ($q = u,\ s,\ d$) quarks. These two components have different distributions of discriminating variables and are independent.

The tagging variable y for a jet is defined as:

$$\begin{aligned} y &= n^c/n^b \prod y_i^c + n^q/n^b \prod y_i^q \\ y_i^{(c,q)} &= f_i^{(c,q)}(x_i)/f_i^b(x_i) \end{aligned} \tag{B.4}$$

where $f_i^q(x_i)$, $f_i^c(x_i)$ and $f_i^b(x_i)$ are probability density functions of x_i generated by uds, c and b quarks respectively, and n^q, n^c and n^b are their normalised rates, such that $\sum n^q = R_q$, $\sum n^c = R_c$, $\sum n^b = R_b$. R_q, R_c and R_b are normalised production rates of different flavours.

The b-tagging variable, x_b is often defined as

$$x_b = -log_{10}y$$

B.1.2 Event b-tagging

B hadrons are almost always produced in pairs and the presence of the second B-hadron significantly improves the b-tagging as a whole. The likelihood ratio method allows combining the information from the two b-hadrons. Knowing that different flavours are produced independently, the equation for the event tagging variable can be written as:

$$y_{12}^{ev} = \frac{R_b}{R_c}\frac{n_1^c n_2^c}{n_1^b n_2^b}\prod y_{i,1}^c y_{i,2}^c + \frac{R_b}{R_q}\frac{n_1^q n_2^q}{n_1^b n_2^b}\prod y_{i,1}^q y_{i,2}^q \tag{B.5}$$

where y_1 and y_2 are two best tagged jets tagging variables, given by B.5. The information from two jest can be combined into a single tagging variable in the following, simpler way:

$$y_{12}^{ev} = y_1 \cdot y_2 \tag{B.6}$$

The b-tagging variable computed from B.6 was used in the DELPHI Higgs search.

B.2 Discriminating variables

Discriminating variables used in combined b-tagging are given here for jets with reconstructed secondary vertices. Other jet categories are described in [49].

- **The jet lifetime probability, P_j^+.**

  The variable defines probability that tracks being analyzed, are coming from the primary vertex. For b-quark jets as well as b-events the variable value is small. To compute this variable an analysis of tracks impact parameter is made. The impact parameter in the plane perpendicular to the beam axis is defined as the distance of the closest approach (ca) to the beam spot (primary vertex – pv). The sign of the impact parameter of the track is positive, if pv-ca vector component in the direction of its jet is positive. Tracks of b-quark origin are expected to have positive impact parameters. Due to the non-zero lifetime of D-mesons it can also be large for c-jets limiting the performance of the life-time tag.

- **The mass of particles combined at the secondary vertex, M_s.**

  This variable is sensitive to the quark flavour. The invariant mass of the particles from the secondary vertex for c-jets is limited by the mass of D-mesons (about 1.8 GeV/c^2), while a b-jet mass can go up to 5 GeV/c^2.

- **The fraction of the charged jet energy included in the secondary vertex, X_s^{ch}.**

  It reflects differences in the fragmentation properties of different flavours. The total energy of charged particles from the secondary vertex in light quark jets is much smaller than in b-quark jets. In case of b-jets the distribution of X_s^{ch} is determined by the fragmentation function $f(b \to B)$ whereas for a c-quark the distribution is determined by $f(c \to D)$, which is softer.

- **The transverse momentum at the secondary vertex, P_s^t.**

  The variable takes into account missing particles not included in the secondary vertex definition. P_s^t is defined as resultant transverse momentum, with respect to the B-hadron's estimated flight direction, of all charged particles attached to the secondary vertex. Due to the high mass of the B-hadron, the value of $P_s^t$for b-quark is higher than for c-quarks.

- **The rapidity of each track included in the secondary vertex , R_s^{tr}.**

  Although a B-hadron in a b-jet has on average a higher energy than a D-meson from a c-jet, the rapidities (defined as $1/2 \ln[(E + p_z)/(E - p_z)]$) of particles from B-decay are on average less than those from D-decay. This can be explained by the larger mass of the B-hadron and the larger multiplicity of its decay [54]. The 'fake' secondary vertices in light quark jets are due to wrongly measured tracks caused by multiple scattering in the detector and interactions with detector material causing the tracks to be shifted to even smaller values. This variable significantly improves the b-quark selection. Although a B-hadron on average is produced with higher energy, rapidities of particles from B-decays are less than those from D-meson decay. This is mainly explained by the higher B-meson mass. The variable R_s^{tr} is defined for each track in the secondary vertex. For rapidity computation charged particles are given the pion mass, whereas neutrals (except for K^0 and Λ) are assumed to be massless.

- **The transverse momentum of an identified energetic lepton, P_l^t.**

  In case the B decays semi-leptonically ($\mathrm{BR}_{B\to X\ell^-\bar{\nu_\ell}} \sim 11\%$) the transverse momentum of the lepton with respect to the B hadron direction [55] can be exploited. Due to the large mass of the b-quark this transverse momentum is expected to be larger for B-hadrons than for hadrons containing only light quarks. In absence of life-time information this is an excellent separating variable.

Appendix C

Extraction of limits

The goal of a search is to establish as strongly as possible either the existence of a signal or its absence. It should be expressed in terms of the test of the appropriate hypotheses. One should remember, however, that from the statistical point of view one only could or could not reject assumed hypothesis at given confidence level.

If there is a clue in the data that the sought signal is present, one should test the hypothesis that the signal is absent. The higher level of rejection of such hypothesis, the more probable is presence of the signal in the data. In the opposite case (no clue for the signal in the data) one should test the hypothesis that the signal is present.

One should then quantify the degree to which one of the hypotheses is favored or excluded by the experimental observations. The process can be described in three steps [56]

1. Identification of the variables in the experiment that comprise the search result. The simplest observable is the number of candidates left after a certain set of criteria was applied.

2. Definition of *test-statistics* as a function of these observables and of certain model parameters (for example particle mass or production rates), which allows to rank experiments from the most background-like to the most signal-like.

3. Choice of the confidence level, at which the hypothesis will be tried to be rejected.

Let us consider the simplest case - the observable which is the number of candidates found, with no background expected. Assuming that the observed number of events has a Poisson probability distribution, the confidence level to which a signal distribution with a given mean value μ is excluded for N_{obs} observed events, is given by the probability that the number of events is less than or equal to N_{obs} [57]:

$$CL_s = P_s(N \leq N_{obs})$$

where

$$P_s(N \leq N_{obs}) = \sum_{k=0}^{N_{obs}} \frac{\mu^k e^{-\mu}}{k!}$$

This situation can become more complicated in three different ways [58]:

1. there might be background expected from standard processes; a way of correction for known backgrounds is then needed,

2. several channels, often having very different efficiencies and/or branching ratios and/or collected luminosities, may contribute to a certain search,

3. the search result may not be simply a number of candidates, and additional information can be present. In particular, there can be information on the mass range of each candidate.

All these points are relevant for the Higgs analyses.

A standard technique [56, 57] to deal with the first problem is to normalise the confidence level for the signal + background hypothesis, CL_{s+b}, to the confidence level for the background-only hypothesis CL_b. This also makes it possible to obtain sensible exclusion limits on the signal even when the observed rate is so low that the background hypothesis is called into question.

The test statistics is constructed to increase monotonically for increasing signal-like (decreasing background-like) experiments so that the confidence in the signal + background hypothesis is given by the probability that the test-statistic is less or equal to the value observed in the experiment, X_{obs}:

$$CL_{s+b} = P_{s+b}(X < X_{obs}) \tag{C.1}$$

where

$$P_{s+b}(X < X_{obs}) = \int_0^{X_{obs}} \frac{dP_{s+b}}{dX} dX \tag{C.2}$$

and $\frac{dP_{s+b}}{dX}$ is the probability density function of the test-statistic for signal + background experiments. Similarly, the confidence in the background hypothesis is given by the probability that the test-statistic is less than or equal to value observed in the experiment X_{obs}:

$$CL_b = P_b(X < X_{obs}) \tag{C.3}$$

and

$$P_b(X < X_{obs}) = \int_0^{X_{obs}} \frac{dP_b}{dX} dX \tag{C.4}$$

where $\frac{dP_b}{dX}$ is the probability density function of the test-statistic for background only experiments.

The normalization described above is:

$$CL_s \equiv CL_{s+b}/CL_b \tag{C.5}$$

The signal hypothesis will be excluded at the confidence level CL when

$$1 - CL_s \leq CL \tag{C.6}$$

Let us consider the search result, given by a number of events with a Poisson distribution. Then the CL_s is given by:

$$CL_s = \frac{e^{-s} \sum_{k=0}^{N_{obs}} (s+b)^k/k!}{\sum_{k=0}^{N_{obs}} b^k/k!} \tag{C.7}$$

where N_{obs} is the number of events observed, b is the average background value (known) and s is the desired upper limit for the signal. This expression is commonly used to obtain conservative limits on the signal hypothesis [57].

In the case that several channels are present, the *naïve* approach within this method is to add the backgrounds, the expected signal rates and the observed number of events for all the channels, taking into account the efficiencies (ϵ_i), cross sections (σ_i) and luminosities ($\mathcal{L}_i$):

$$b = \sum b_i \qquad s = \sum s_i = \sum \epsilon_i \sigma_i \mathcal{L}_i \qquad N_{obs} = \sum N_{obs_i} \tag{C.8}$$

where index i runs over all channels. The drawback of this procedure shows up when channels with very different characteristics are combined. The presence of candidates in a channel with a very low value of s_i (i.e. very low efficiency, cross section or luminosity), and hence with a small contribution to the total number of expected signal events, can deteriorate considerably the obtained limit. This is true even if there is expected background, given the characteristics of the Poisson distribution.

Another disadvantage of this procedure is that it does not take into account the mass information of the candidates. Clearly, an events of reconstructed mass m_i such that $|m_0 - m_i| \gg \sigma_m$, where σ_m is the mass resolution, should not be considered as a candidate for the mass m_0. In practice, an arbitrary and common convention is to take the events as candidates for the mass region defined by $m_i \pm 2\sigma_m$.

In fact there is no real consensus about how to compute limits and how to overcome the above problems. Different methods giving at least partial solutions are available, but none of them is accepted. In particular, the problem of the combination of different channels became a crucial point at the moment of combining the search results of the different LEP experiments. Methods used by different experiments can be found in reference [56]. Only one of methods used and developed within the DELPHI experiment will be briefly described. The other method description can be found in a DELPHI paper by A. Read [56].

C.0.1 Bayesian approach for processes with subchannels

A way of making better use of the information about the different search channels [59] is to give to each channel a weight, defined as $w_i = s_i/s_{tot}$ (the branching ratio of the signal in channel i and to combine all the channels by assuming a probability function that is simply the product of the independent distributions for each channel. This is done in the framework of the Bayesian approach.

In the Bayesian approach the upper limit s on the parameter σ for the process with a probability function $W(n,\ \sigma)$ is given by:

$$1 - CL = \frac{\int_s^\infty W(n,\ \sigma) d\sigma}{\int_0^\infty W(n,\ \sigma) d\sigma} \tag{C.9}$$

If we assume:

- Poisson distribution in the total number of signal events;
- k channels;
- an average background b_i and a branching ratio w_i in each subchannel;
- the joint probability function for the total number of events $n_i = n_i^s + n_i^b$ in each subchannel is the product of independent Poisson distributions:

  $W(n_1,\ ...,\ n_k;\ s;\ w_1,\ b_1,\ ...,\ w_k,\ b_k) = P(n_1;\ sw_1 + b_1) \times ... \times P(n_k;\ sw_k + b_k)$

  where $P(n;\ s) = e^{-(s+b)}(s+b)^n/n!$ is the Poisson distribution.

Using C.9 one obtains:

$$1 - CL = \frac{e^{-s_{tot}} \prod_{i=1}^{k} \sum_{j=0}^{n_i} (s_{tot} + b_i/w_i)^j/j!}{\prod_{i=1}^{k} \sum_{j=0}^{n_i} (b_i/w_i)^j/j!} \tag{C.10}$$

This method accounts for the combination of different channels but not for the problem if including the mass information. More generally, the problem of search results given by continuous variables is not treated in a natural way by this method. A way of introducing the mass information is described in [59].

Acknowledgements

I am very grateful to many people who have helped me during completion of this thesis. I am greatly indebted to Piotr Zalewski for his constant consultation and support during my work on this thesis. I would like to express my gratitude to my supervisor, professor Ryszard Sosnowski for his support and help in solving many big and small problems. My special thanks go to Ryszard Gokieli, for our discussions, and for his great help, priceless advises and interest. I would also like to thank Maarten Boonekamp, for fruitful discussions, for his interest and help with some problems. I would like to thank all the members of the DELPHI Warsaw group for friendly atmosphere. I am indebted to all those people not mentioned here by name, who encouraged me during my work on the thesis, who showed their interest and sympathy and who believed in me.

Bibliography

[1] D. Groom *et al.* *Review of particle physics.* Eur. Phys. J. **C15** (2000) 1.

[2] F. Mandl and G. Shaw. *Quantum field theory.* John Wiley & Sons, 1984.

[3] I. C. Taylor. *Gauge Theories of Weak Interactions.* Cambridge University Press, 1976.

[4] J. Iliopoulos. *An Introduction to Gauge Theories.* Proceedings of the 1997 CERN-JINR School of Physics (1977) 36.

[5] J. Goldstone. *Field Theories with 'Superconductor' Solutions.* Nuovo Cimento **19** (1961) 154.

[6] S. Weinberg, J. Goldstone, A. Salam. *Broken Symmetries.* Phys. Rev. **127** (1962) 965.

[7] Ta-Pei Cheng and Ling-Fong Li. *Gauge theory of elementary particle physics.* Clarendon Press, Oxford, 1984.

[8] J. F. Gunion. *The Higgs Hunters Guide.* Addison-Wesley Publishing Company, 1990.

[9] A. G. Cohen, D. B. Kaplan, A. E. Nelsen. *Spontaneous Baryogenesis at the Weak Phase Transition.* Phys. Rev. **B263** (1991) 86.

[10] U. Amaldi, A. Bohm, G. L. Durkin, P. Langacker, A. K. Mann, W. J. Marciano. *A Comprehensive Analysis of Data Pertaining to the Weak Neutral Current and the Intermediate Vector Boson Masses.* Phys. Rev **D36** (1987) 1385.

[11] G. Costa, J. Ellis, G. L. Fogli, D. V. Nanopoulos and F. Zwirner. *Neutral currents within and beyond the standard model.* Nucl Phys **B297** (1988) 244.

[12] D. A. Rossa and M. Veltman. *Neutral Currents in Neutrino Experiments.* Nucl. Phys **B95** (1975) 135.

[13] S. Glashow and S. Weinberg. *Natural Conservation Laws For Neutral Currents.* Phys. Rev. **D15** (1977) 1958.

[14] P. Abreu *et al.* (DELPHI Collaboration). *DELPHI Detector at LEP.* Nucl. Instr. and Meth. **A303** (1991) 233.

[15] P. Abreu *et al.* (DELPHI Collaboration). *Performance of the DELPHI Detector.* Nucl. Instr. and Meth. **A378** (1996) 57.

[16] The LEP Collaborations, the LEP Electroweak Working Group, the SLD Heavy Flavour Group. *A Combination of Preliminary Electroweak Measurements and Constraints on the Standard Model.* CERN-PPE/97-154, 1997.

[17] DELPHI Collaboration. *DELANA User's Guide.* DELPHI 89-44 PROG 137, Geneva, 1989.

[18] D. Bertrand, L. Pape (DELPHI Collaboration). *TANAGRA, Track Analysis and Graphics Package.* DELPHI 87-95 PROG 98, Geneva, 1987.

[19] DELPHI Collaboration. *DELSIM, DELPHI event generation and detector simulation - Reference Manual* . DELPHI 89-68 PROG 143, Geneva, 1989.

[20] ALEPH Collaboration, R. Barate, *et al., Mass limit for the Standard Model Higgs boson with the full LEP-1 ALEPH data sample.,* Phys. Lett. **B384** (1996) 427
DELPHI Collaboration, P. Abreu, *et al., Search for the Standard Model Higgs boson in Z^0 decays.,* Nucl. Phys. **B421** (1994) 3
L3 Collaboration, M. Acciari, *et al., Search for neutral Higgs boson production through the process $e^+e^- \to Z^\star H^0$.,* Phys. Lett. **B385** (1996) 454
OPAL Collaboration, G. Alexander, *et al., Search for neutral Higgs bosons in Z^0 decays using the OPAL detector at LEP.,* Z. Phys. **C73** (1997) 189 .

[21] Report of the LEP working group. *Lower bound for the SM Higgs boson mass: combined results from the four LEP experiments* . CERN/LEPC 97-11, Geneva, 1997.

[22] OPAL Collaboration, G. Abbiendi, *et al.* . *Search for Higgs Bosons in e^+e^- Collisions at 183 GeV.* Eur. Phys. J **C7** (1999) 407.

[23] L3 Collaboration, M. Acciari, *et al.* . *Search for Neutral Higgs boson production through the process $e^+e^- \to Z^*H^0$* . Phys. Lett. **B385** (1996) 454.

[24] P. Chankowski, M. Krawczyk, J. Zochowski, Report of the LEP working group. *Implications of the precision data for very light Higgs boson scenario in 2HDM,2* . Eur. Phys. J. **C11** vol.4 (1996) 661.

[25] M. Krawczyk, J. Zochowski, P. Mättig. *Process Z to h(A)+ gamma in the 2HDM and the experimental constraints from LEP* . Eur. Phys. J. **C8** vol.3 (1999) 495.

[26] The ALEPH Collaboration. *Search for a Light Higgs Boson in the Yukawa Process.* PA13-026, Contribution to the International Conference on High Energy Physics, Warsaw, Poland, 1996.

[27] A. Pich, J. Prades and P. Yepes. *Bounds on a light scalar in two-Higgs-doublet models.* Nucl. Phys. **B388** (1992) 31.

[28] F. Larios, G. Tavares-Velasco, C. P. Yuan . *A very light CP-odd scalar in the Two-Higgs-Doublet Model* . Phys. Rev. **D64** vol. 5, (2001) 055004.

[29] F. Larios, G. Tavares-Velasco, C. P. Yuan . *Update on very light CP-odd scalar in the Two-Higgs-Doublet Model.* Phys. Rev. **D66** (2002) 075006.

[30] D. Chang, W. F. Chang, C. H. Chou, W. Y. Keung . *Large Two-Loop Contributions to g-2 from a Generic Pseudoscalar Boson.* Phys. Rev. **D63** vol.9 (2001) 91301.

[31] K. Adel, F. J. Yndurain . *Improved Evaluation of the Hadronic Vacuum Polarisation Contributions to Muon g-2 and $\alpha_{QED}(M_Z)$ Using High Order QCD Calculations.* Rev. Acad. Ciencias (Esp.) **92** (1998), hep-ph/9509378.

[32] A. Czarnecki, W. J. Marciano . *The Muon Anomalous Magnetic Moment : A Harbinger For "New Physics"* . Phys. Rev. **D64** (2001) 013014.

[33] M. Davier, A. Höcker . *New Results on the Hadronic Contributions to $\alpha(M_Z^2)$ and to (g-2)$_\mu$* . Phys. Lett. **B435** (1998) 427.

[34] L3 Collaboration. *Search for pair production of neutral Higgs bosons in two-doublet models.* paper EPS098 submitted to the Brussels EPS Conference, 1995.

[35] J. Kurowska, O. Grajek, P. Zalewski, DELPHI Collaboration. *Search for Yukawa production af a light neutral Higgs at LEP1.* DELPHI 99-76 CONF 263, paper submitted to the HEP'99 Conference, Tampere, Finland, July 1999.

[36] M. Bluj, M. Boonekamp, J. Hoffman, P.Zalewski, DELPHI Collaboration. *Search for Higgs Bosons in a general Two Higgs Doublet Model.* DELPHI 2001-068 CONF 495, contributed paper for EPS HEP 2001 (Budapest) and LP01 (Rome), 2001.

[37] G. Abbiendi *et al.* (OPAL Collaboration). *Search for Yukawa Production of a light neutral Higgs Boson at LEP.* Eur. Phys.J **C23** (2002) 397.

[38] P. Abreu *et al.* (DELPHI Collaboration). *Search for Neutral Higgs Bosons in Extended Models.* CERN-EP/2002-316.

[39] T. Sjöstrand. *The LUND Monte Carlo For Jet Fragmentation and e^+e^- Physics: JETSET Version6.3 and Update.* Comp. Phys. Comm. **39** (1986) 347.

[40] B.F.L. Ward S. Jadach and Z. Was. *The precision Monte Carlo event generator KK for two-fermion final states in e^+e^- collisions.* Comp. Phys. Comm. **130** (2000) 260.

[41] F.A. Berends, R. Pittau, R. Kleiss. *Excalibur : a Monte Carlo program to evaluate all four fermion processes at LEP 200 and beyond.* Comp. Phys. Comm. **85** (1995) 437.

[42] SE. Accomando, A. Ballestrero. *WPHACT 1.0 – A program for WW, Higgs and 4 fermion physics at e^+e^- colliders.* Comp. Phys. Comm. **99** (1997) 270.

[43] M. Krawczyk J. Kalinowski. *Fermion mass effects on* $\Gamma(Z\to b\bar{b}$ *+ a light Higgs) in a Two Higgs Doublet Model.* Phys. Lett. **B361** (1995) 66.

[44] F. Cossutti, M. Elsing, M. Espirito-Santo, C. Parkes, T. Spassoff, A. Tonazzo, C. Weiser, K. Beloous, V. Hedberg, F. Mazzucato. *Improvements to SKELANA for Version 2.0.* DELPHI 99-175 PROG 239, 1999.

[45] *DELGRA, DELPHI Graphics for Interactive Event Viewing, User manual,* http://delphiwww.cern.ch/~delgra/delgra/delgra.html.

[46] Maarten Boonekamp, DELPHI, private communication.

[47] Piotr Zalewski, DELPHI, private communication.

[48] S. Catani, Y. L. Dokshitzer, M. Olson, G. Turnock and B. R. Webber. *New clustering algorithm for multi-jet cross-sections in* e^+e^- *anihilation.* Phys. Lett. **B269** (1991) 432.

[49] P. Abreu *et al.* (DELPHI Collaboration). *b-tagging in DELPHI at LEP.* DELPHI 2002-031 CONF 565, contributed paper for ICHEP2002 (Amsterdam).

[50] P. Abreu *et al.* (DELPHI Collaboration). *Measurement of the rate of* $b\bar{b}b\bar{b}$ *events in hadronic Z decays and the extraction of the gluon splitting into* $b\bar{b}$. Phys. Lett. **B462** (1999) 425.

[51] M. H. Seymour. *Heavy quark pair multiplicity ine* e^+e^- *events.* Nucl. Phys. **B436** (1995) 163.

[52] J. Bagger, V. Barger, K. Cheung, J. Gunion, T. Han, G. A. Ladinsky, R. Rosenfeld, and C.-P. Yuan. *CERN LHC analysis of the strongly interacting WW system: Gold plated modes.* Phys. Rev. **D52** (1995) 3878.

[53] J. R. Pelez. *Strong WW scattering and resonances at LHC.* hep-ph/9705301, Contribution to the XXXIInd Rencontres de Moriond: *"Electroweak Interactions and Unified Theories* (May, 1997).

[54] DELPHI Collaboration, P. Abreu *et al* . *Hadronization properties of b quarks compared to light quarks in* $e^+e^- \to q\bar{q}$ *from 183 GeV to 200 GeV.* Phys. Lett. **B479** (2000) 118.

[55] M. Boonekamp. *b-tagging with high-pt leptons.* DELPHI-98-54, internal DELPHI-note, 1998.

[56] A. Read, DELPHI Collaboration . *Optimal statistical analysis of search results based on the likelihood ratio and its application to search for the MSM Higgs boson at* $\sqrt{s} = 161$ *and* $\sqrt{s} = 172$ *GeV.* DELPHI 97-158 PHYS 737.

[57] Review of particle physics. The Eur. Phys. J. **C3** (1998).

[58] M. Espirito Santo. *Search for composite and exotic leptons with the DELPHI detector at LEP2.* PhD thesis.

[59] V. Obraztsov. *Confidence limits for processes with small statistics in several subchannels and with measurement errors.* Nucl. Instr. Methods. **A316** (1992) 388.